Wavelet Weighted Distortion Measures for Retinal Images

A THESIS

submitted for the award of the degree of

DOCTOR OF PHILOSOPHY

By

S. R. Nirmala

DEPARTMENT OF ELECTRONICS AND ELECTRICAL ENGINEERING

INDIAN INSTITUTE OF TECHNOLOGY GUWAHATI

GUWAHATI - 781 039, INDIA

July 2012

This thesis is dedicated to

My Parents

and

Son **Supreeth** and Husband **Prasanna**

for their love, support and encouragement

Certificate

This is to certify that the thesis entitled "**Wavelet Weighted Distortion Measures for Retinal Images**", submitted by **S. R. Nirmala**, a research scholar in the *Department of Electronics and Electrical Engineering, Indian Institute of Technology Guwahati*, for the award of the degree of **Doctor of Philosophy**, is a record of an original research work carried out by her under our supervision and guidance. The thesis has fulfilled all requirements as per the regulations of the institute and in our opinion has reached the standard needed for submission. The results embodied in this thesis have not been submitted to any other University or Institute for the award of any degree or diploma.

Dated:

Guwahati.

Prof. S. Dandapat

Prof. P. K. Bora

Dept. of Electronics and Electrical Engineering

Indian Institute of Technology Guwahati

Guwahati - 781 039, India.

Acknowledgements

I would like to express my whole hearted and deep sense of gratitude to my guides Prof. S. Dandapat and Prof. P. K. Bora for their guidance, help and encouragement throughout my research work. I am greatly inspired by their attitude towards research, creative thinking, hard work and dedication in work. I am highly grateful to them for patiently checking all my manuscripts and thesis. This thesis would not have been possible without their bounteous effort. I owe my profound gratitude to Prof. S. Dandapat and Prof. P. K. Bora for their support in all respects.

I am very thankful to Prof. C. Mahanta, chairman of my doctoral committee, for her moral support, encouragement and suggestions rendered during the evaluation of my research work.

I am also thankful to my former doctoral committee member Dr. J. S. Sahambi.

My sincere thanks are due to my doctoral committee members Dr. S. R. Ahamed and Dr. M. K. Bhuyan for their useful advice and for sparing their valuable time to evaluate the progress of my work.

I specially thank Prof. Anil Mahanta for his advice and suggestions.

I would like to thank the faculty members of the department.

I would like to acknowledge all the help rendered by Manikandan and Krishnamoorthy during the initial stages of my research work. The discussions and valuable suggestions helped me in improving the research and programming skill.

My hearty thanks goes to Pati sir, Jayanna sir, Pradhanji, Sumitra, Govind, Abhinav, Deepak, Shweta and Malaya Nath.

I also thank Mr. Sanjib Das for his timely help.

I specially wish to express my thanks to Amrita Ganguly, Priya, Sharma sir and Josephine for sharing and caring during the ups and downs of my research life.

My sincere thanks go to Prof. Shankara Jois and Mrs. Ambuja Jois for their parental treatment, moral support and care to my family.

I would like to thank my well wishers Ranga Kumari, Dr. K. S. Rao and Remya Iyer.

I would like to thank all my friends and labmates for their wishes and help directly and indirectly during my research work.

I would like to thank my colleagues of Gauhati university, specially K. K. Sarma sir, for their help and support during the period of my thesis preparation.

Also, special thanks goes to the retinal experts from Shri Sankaradeva Netralaya - Guwahati and my labmates who participated in the subjective evaluations.

My greatest debt of gratitude is owed to my parents, whose hard work and sacrifices made me what I am today.

I would like to express my sincere gratitude to my in-laws for their support and blessings.

My loving thanks to my son Supreeth for being a good boy and always cheering me with his sweet smile and kiss.

Last, but not the least, I wish to convey my insurmountable gratitude to my husband, for his love, patience and encouragement during my doctoral studies.

S. R. Nirmala

Abstract

This thesis work is an investigation of new distortion measures in the wavelet domain. These measures are expected to quantify the clinical information loss in the processed retinal images. There are three major contributions. First, different subbands are investigated for the presence of retinal image information. Secondly, wavelet weighted distortion measures are defined for each of the retinal features. Third, performance of the new distortion measures is evaluated and compared with that of various state of the art image quality measures.

For medical images, the quality measure is expected to emphasize any distortion in the clinically important regions. The traditional squared error measures give equal importance to all parts of the image. To incorporate the importance of distortion in clinically significant regions into the measure, it is required to localize the retinal features such as the blood vessel, optic disc and macula. The spatial frequency localization and multiresolution properties of the discrete wavelet transform (DWT) can make it an efficient way of image representation. The DWT is used to decompose the image into different subbands. The contribution of each subband towards the image information is different. In the present work, two methods are proposed to examine the significance of a subband from the point of view of retinal features. In the first method, different subbands are investigated for the presence of information about the retinal image features. In the second method, the information about blood vessels in different subbands is exploited to propose a new method for the segmentation of blood vessels. After identifying the subbands which contain significant information about retinal features, a wavelet weighted distortion measure is defined. Different weights are assigned to different subband error measures.

The loss of clinical information is quantified as a weighted sum of the root of the normalized mean square errors of the coefficients in all the subbands. The distortion measure is computed for each of the features. A global wavelet weighted distortion measure (WWDM) for assessing the clinical quality is then defined by combining the individual distortion measures.

The proposed distortion measure WWDM is evaluated quantitatively and qualitatively in predicting the clinical quality of the distorted retinal images. The performance of the WWDM is compared with other image quality measures by applying them on retinal images degraded by different types of artifacts such as JPEG and wavelet compression, blur and noise. The statistical measures used for evaluation are, the *Pearson linear correlation coefficient* (PLCC), *Spearman rank order correlation coefficient* (SROCC), the *outlier ratio* (OR) and *root mean square error* (RMSE) between the actual mean opinion score (MOS) and the predicted MOS values. The statistical behavior is also evaluated in terms of how the measure is discriminating the artifacts when tested on a variety of images using the analysis of variance (ANOVA) method. The WWDM performs better among all the other state of the art image quality measures tested in this work.

Synopsis

Introduction

Retinal images have the potential to facilitate the early detection of retinal pathologies. The clinically important features of a retinal image are the *optic disc* (OD), the *macula* and the *blood vessels*. The ophthalmologists examine these features for signs of various eye related diseases. The retinal image should be of sufficient quality for reliable diagnosis. In some applications like telemedicine, these images need to be processed for efficient storage and transmission. Any such processing causes distortion and degrades the clinical quality of the image. It is expected that distortion occurs to the clinical information in the processed images. There is a need for quantification of the distortion in clinical information during such processing. This thesis documents the investigations on quantifying the loss of clinical information in processed retinal images using wavelets.

The processed image quality is generally evaluated subjectively and assessed quantitatively using the traditional measures, the *mean square error* (MSE) and the *peak signal to noise ratio* (PSNR). These measures quantify the error globally and fail to characterize the error in local clinical features. There is a limited research work in the direction of the quality evaluation of processed retinal images. They focus on how the distortion due to processing affects the detection and diagnosis of diseases. But the issue of quantifying the clinical distortion in retinal images has not been addressed.

There are three major contributions in this work. In the first, the effect of distortions of the clinical features in different wavelet subbands is studied. This study identifies the subbands that carry significant information about a retinal feature. Secondly, after identifying the clinically significant subbands, different weights are assigned to different subbands. The clinical information loss is quantified as a weighted sum of the root of normalized mean square errors of the coefficients in all the subbands. The clinical distortion measure is computed for each retinal feature. A global clinical distortion measure is defined by combining the distortion measures for individual features. As a third problem, the performance of the distortion mea-

sure is investigated in predicting the quality of the retinal images with different artifacts. The statistical measures used for evaluation are, the *Pearson linear correlation coefficient* (PLCC), the *Spearman rank order correlation coefficient* (SROCC), the *outlier ratio* (OR) and the *root of the mean squared error* (RMSE) between the subjective scores and the predicted subjective scores after nonlinear regression. The statistical behavior is also evaluated in terms of how the measure discriminates the artifacts when tested on a variety of images using the *analysis of variance* (ANOVA) method. It is shown that the wavelet weighted distortion measure can effectively quantify the distortion in clinical features of processed retinal images.

Motivation

For medical images, a distortion measure has to be defined from the diagnostic perspective. Such a measure should take proper account of the clinical nature of the images. Certain regions of a medical image are rich in clinical information and some regions are clinically non-significant. The distortion occurring in these clinically informative regions is more important than that in the background regions. The image quality measure is expected to emphasize any distortion in clinically important regions and deemphasize the effects in nondiagnostic regions. The traditional measures, MSE and PSNR are simple and estimate the distortion on a pixel by pixel basis. The drawback of the squared error measures is that they give equal importance to all parts of the image. It is because of such shortcomings some alternate measures need to be searched for medical images.

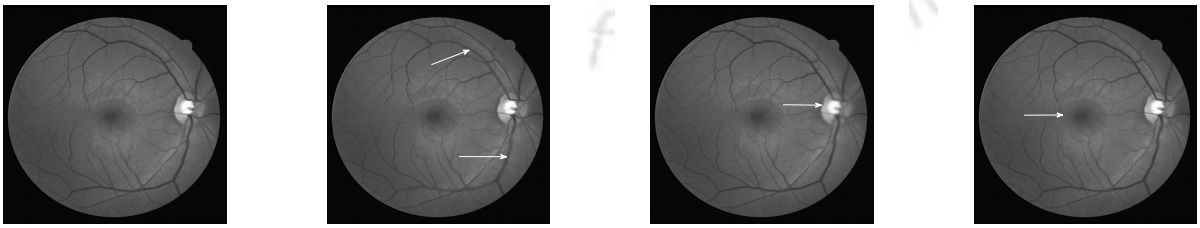

(a) (b) (c) (d)

Figure 1: Retinal images with same MSE but having distortion in the (a) dark background region (b) thick blood vessels (c) optic disc region and (d) macula region (shown with white arrows).

The limitations of conventional objective measures are illustrated using Figure 1. The figure shows four retinal images having the same value of MSE($\simeq 12\%$). But the error in each image is due to distortions in different spatial locations including the diagnostic features and nonsignificant regions. The distortion in different diagnostic features may indicate different pathological conditions. The distortion in the dark background region is diagnostically insignificant. The high values of error measures due to distortion in the dark background regions may mislead the evaluation of the retinal image. Measuring the distortion in diagnostic features is more meaningful than quantifying the error globally using the entire image.

To incorporate the importance of distortion in clinically significant regions into the measure, it is required to segment the image into clinically important regions and the background. The accurate segmentation of clinical features in retinal image is relatively a difficult task. In this direction, alternate methods can be investigated to localize the retinal features. The *spatial frequency localization* and *multiresolution analysis* (MRA) properties of the discrete wavelet transform (DWT) present an efficient way of image representation. The multiresolution decomposition of a retinal image separates the clinically important features into different frequency subbands. The multiscale property of the wavelet shows that the features which are difficult to detect at one scale may be easily detected at another scale. Hence the DWT can be explored for localizing the retinal image components. The recent compression techniques for medical images such as JPEG2000 and DICOM use the DWT. Wavelet based thresholding is effective for image denoising. These attractive features of wavelet analysis motivated us to develop a wavelet based distortion measure to quantify the loss of clinical information in retinal images.

Analysis of retinal features in wavelet subbands

The importance of wavelet subbands in representing the retinal features is investigated. The DWT separates and retains the image features in one or a few of the subbands. The retinal image is decomposed to 5 levels using bior6.8 wavelet. This generates one low frequency approximation subband and fifteen high frequency detail subbands. Different subbands refer to different frequency bands of an image. They have different contributions to the image quality.

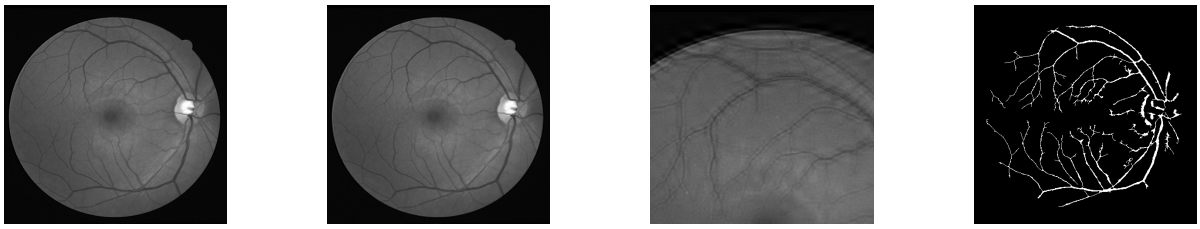

(a) (b) (c) (d)

Figure 2: (a) Original image and reconstructed images when subband coefficients of (b) L1, (c) L3 are made zero (a small section of the image is shown for better visualization) and (d) segmented image showing the vessels

Distortion at different frequencies will have different impact on the image content. Hence we have introduced distortion in different subbands and its effect on the quality of the retinal image features is observed. The diagnostic importance of subbands in a level is examined by zeroing the coefficients of the subbands at that level and keeping all other subbands undisturbed. The diagnostic quality of the retinal image is observed by reconstructing the image using the altered subbands.

(a) Wavelet subbands and blood vessel information:

The blood vessels represent abrupt changes in intensity and characterized by high frequency subbands (high spatial frequency components). The image in Figure 2(b) is obtained after zeroing the coefficients of decomposition level-1 (L1) subbands H(1), V(1) and D(1). It is observed that the vessel structure is well reconstructed as compared with the original image shown in Figure 2(a). This shows that these (highest frequency) subbands do not have significant blood vessel information. The image in Figure 2(c) is produced after zeroing the coefficients of level-3 (L3) subbands. It is observed that altering these coefficients has relatively greater influence on the thick vessels than that on the thin vessels. Similar experiments show that the thin vessels are sensitive to the second level (L2) subband coefficients. Modifying the level-4 (L4) has little influence on thick blood vessels. The level-5 (L5) subband coefficients represent the slowly varying retinal background and have minimum effect on the blood vessels. The thin vessels are composed of higher frequency components as compared to the thick vessels. The distortions

in them are perceived even at low compression. Hence the L2 subbands are expected to have higher clinical importance compared to the other subbands. With all these observations, different subbands can be arranged in the descending order of their vessel information content, as $L2, L3, L4, L5$ and $L1$.

The above observations are exploited to develop a novel method for the segmentation of blood vessels. The vessel image is obtained by subtracting the background from the original image. The background image contains all the information except blood vessels. This can be estimated by making the subband coefficients of L2, L3, and L4 zero. The coefficients of high frequency subbands of L1 and low frequency approximation and high frequency L5 subbands are kept intact. This suppresses the blood vessel components in the retinal image leaving only the approximated background. After thresholding and postprocessing the vessel image, the segmented vessels are shown in Figure 2(d). The segmented vessel structure indicates that, out of many subbands only a few are significant for the blood vessels.

(b)Wavelet subbands and optic disc information:

The OD and macula regions are small compared to the entire retinal image space. Their characteristics are effectively studied by considering small blocks containing those regions. The experiments show that the optic disc structure is well preserved when the subbands of L1 and L5 are zeroed. This indicates that they are clinically less important. The distortion in the OD when subbands of L3 are zeroed is relatively more when compared to the case of zeroing the subbands of L2 and L4. The different subbands are expected to be in the order of importance as $L3, L2, L4, L5$ and $L1$.

(c)Wavelet subbands and macula information

The macula appears as a dark region near the center of the retinal image. The center of the macula is called fovea. The intensity variation between the macula region and the surrounding retinal region is very sharp compared to the intensity transition from the fovea to the macular region. Similar experiments show that the relative importance of the subbands in representing the macular information may be $L2, L1, L3, L4$ and $L5$.

Wavelet subband weighted distortion measure

The results of the investigation about clinically significant information in subbands of different decomposition level are used to design a variable weighting scheme for the error measures. This helps in defining a more meaningful distortion measure in the wavelet domain. An individual measure is defined to quantify the distortion in each feature. These measures are combined to define a global distortion measure for assessment of the clinical quality of the image. The wavelet based distortion measure WWDM is proposed as

$$\text{WWDM} = \sum_{f \in \{v,d,m\}} \text{WWDM}_f \tag{1}$$

where $WWDM_f$ is the distortion measure for the retinal feature 'f'. The feature 'f' can be blood vessels (v), the OD (d) or the macula (m). The $WWDM_f$ is defined as

$$\text{WWDM}_f = \Delta_{\mathbf{e}}^T \cdot \frac{\Gamma_f}{\text{tr}[\,\Gamma_f\,]} \cdot \Delta_{\mathbf{e}} \tag{2}$$

where $\Delta_{\mathbf{e}}$ is a vector representing the error in wavelet subbands and Γ_f is the diagonal matrix of subband weights $w_{(b,n)}$ for each of the diagnostic features. The weight values are calculated using the subband coefficients of the original image. The weight factor for a detail subband b at the decomposition level n with K number of coefficients can be estimated as the sum of the absolute values of wavelet coefficients $d_{(b,n)}$ within the subband. It is defined as,

$$w_{(b,n)} = \sum_{k=1}^{K} |d_{(b,n)}(k)| \tag{3}$$

Experiments are performed to examine the ability of the proposed WWDM in capturing the clinical distortion. The results show that, the WWDM indicate high values when there is distortion in any of the diagnostic features like the blood vessels, the optic disc and the macula. On the other hand, the distortion measure shows small values and gives less importance to the distortion in a clinically nonsignificant region such as the nonvessel smooth retinal background.

The proposed WWDM estimates the distortion in local diagnostic features and hence performs better in reflecting the diagnostic information loss in retinal images.

Performance evaluation of the proposed WWDM

To evaluate the performance of the proposed WWDM, different retinal images are considered from test and training set images of the DRIVE database. The gray retinal images are obtained from the green channels of the original color images. They are resized to (512×512) and decomposed to five levels using the *biorthogonal* wavelet filters. The performance of WWDM is compared with other image quality measures by applying them on retinal images degraded by different types of artifacts such as compression (JPEG, SPIHT), blur and noise. The measures are then investigated in terms of their correlation with subjective evaluation scores using the PLCC, SROCC, OR and RMSE. Their statistical behavior is also evaluated in terms of how they discriminates different distortion artifacts when tested on a variety of images using the ANOVA method. The experimental results indicate that the proposed method provides better prediction accuracy (higher PLCC), better prediction monotonicity (higher SROCC), better prediction consistency (lower OR) and better performance (lower RMSE) compared to other most widely used image quality measures in the image processing literature. The WWDM is simple to compute and more sensitive to clinically significant distortions in retinal images.

Organization of the Thesis

The contents of the thesis are organized as follows: Chapter 1 presents an introduction and overview of the retinal image analysis. Chapter 2 presents the literature review on quality assessment of retinal images for different applications. Two methods for the analysis of retinal image information in different wavelet subbands are discussed in Chapter 3. In Chapter 4, the new wavelet weighted distortion measure (WWDM) is presented. The performance evaluation of the proposed distortion measure using various statistical parameters and the comparison with other image quality measures are presented in Chapter 5. Chapter 6 concludes the thesis by summarizing the contributions and identifying the future extensions.

Contents

List of Figures **xxiii**

List of Tables **xxvii**

List of Acronyms **xxix**

List of Symbols **xxxiii**

1 Introduction **1**

1.1 Retinal image and its clinical features 4

1.1.1 Clinical importance of retinal images 4

1.2 Retinal image processing 6

1.2.1 Segmentation of anatomical structures in retinal images 7

1.2.1.1 Segmentation of retinal blood vessels 7

1.2.1.2 Segmentation of the optic disc and fovea 9

1.2.2 Detection of abnormalities 11

1.3 Image quality measures 13

1.3.1 Wavelet based medical image analysis 14

1.4 Quality analysis of retinal images 15

1.5 Scope for the present work 17

1.6 Organization of the thesis 18

2 Review of image quality measures **19**

2.1 Image quality measures 20

2.1.1 Subjective measures 20

2.1.2 Objective Quality measures 21

2.2 Wavelet based image quality measures . . . 25
2.3 Quality measures for retinal image . . . 31
2.4 Motivation for the present work . . . 42

3 Analysis of retinal image information in wavelet subbands 47

3.1 Wavelet filter for retinal image analysis . . . 49
3.1.1 Method . . . 51
3.1.2 Selection of optimum decomposition level . . . 52
3.1.3 Selection of appropriate wavelet filter . . . 53
3.2 Wavelet analysis of retinal features . . . 56
3.3 Blood vessel information in wavelet subbands . . . 59
3.3.1 Analysis of vessel information through segmentation . . . 63
3.4 Optic disc information in different wavelet subbands . . . 79
3.5 Macula information in different wavelet subbands . . . 80
3.6 Summary . . . 83

4 Distortion measures in the wavelet domain 89

4.1 Proposed distortion measure . . . 90
4.1.1 DWT based image quality measures . . . 91
4.1.2 Computation of weights . . . 92
4.1.2.1 Proposed weight based on the sum of absolute values of wavelet coefficients . . . 92
4.1.2.2 Weight based on the relative subband mean energy (RSME) . . . 93
4.1.3 Wavelet weighted blood vessel distortion measure ($WWDM_v$) . . . 95
4.1.4 Wavelet weighted distortion measure for the optic disc ($WWDM_d$) . . . 99
4.1.5 Wavelet weighted distortion measure for the macula ($WWDM_m$) . . . 101
4.2 Results and discussion . . . 103
4.2.1 Evaluation of the DWT based distortion measures . . . 104
4.2.1.1 Distortion in blood vessels . . . 104
4.2.1.2 Distortion in the optic disc . . . 107

4.2.1.3 Distortion in the macular region . . . 109
4.2.2 Performance of the individual distortion measures . . . 111
4.2.2.1 Evaluation of the blood vessel distortion measure ($WWDM_v$) . 111
4.2.2.2 Evaluation of the distortion measure for the optic disc ($WWDM_d$) 120
4.2.2.3 Evaluation of the distortion measure for the macula ($WWDM_m$) 123
4.2.3 Evaluation of the proposed WWDM . . . 124
4.3 Summary . . . 125
5 Performance evaluation of distortion measures 127
5.1 Evaluation of image quality measures . . . 128
5.1.1 Experimental details . . . 129
5.1.1.1 Types of image distortion . . . 129
5.1.2 Subjective image quality evaluation . . . 131
5.1.2.1 Processing of the subjective scores . . . 133
5.1.3 Objective image quality measures . . . 133
5.1.4 Evaluation metrics . . . 135
5.1.5 Analysis of variance and F-ratio . . . 138
5.2 Evaluation Results . . . 140
5.2.1 Performance evaluation using the metrics . . . 140
5.2.2 Performance evaluation using the ANOVA . . . 145
5.3 Summary . . . 147
6 Conclusions 149
6.1 Scope for the Future Work . . . 153
A Retinal images under pathological conditions 155
A.1 Pathological retinal images . . . 156
B Training and instructions to the subjects 159
B.1 Training instructions . . . 161

Bibliography **163**

List of Publications **173**

List of Figures

1 Retinal images with same MSE but having distortion in the (a) dark background region (b) thick blood vessels (c) optic disc region and (d) macula region (shown with white arrows). xii

2 (a) Original image and reconstructed images when subband coefficients of (b) L1, (c) L3 are made zero (a small section of the image is shown for better visualization) and (d) segmented image showing the vessels xiv

1.1 A cross sectional view of the eye. (http://www.healthtree.com/articles/anatomy/eye/) 3

1.2 Fluorescein Angiogram (http://www.revophth.com). 3

1.3 Digital retinal photograph from DRIVE database. 5

2.1 Single-level 2-D subband decomposition of the image 26

2.2 Mutual information between the reference image C and the images E and F, where these images denote visual signal at the output of the HVS model from the reference and the distorted images. 29

2.3 Retinal images with same MSE but having distortion in the: (a) dark background region (b) thick blood vessels (c) optic disc region and (d) macula region (shown with white arrows). 43

3.1 Examples of parent-child relationships in the wavelet tree. 51

3.2 Block diagram of the SPIHT algorithm. 52

3.3 Average values of (a) PSNR, (b) LMSE and (c) SSIM at different decomposition levels for CR = 2, 4, 6, 8, 10. The Wavelet filter used is db5. 53

3.4 (a) Original image and reconstructed images when subband coefficients of (b) L1, (c) L2, (d) L3, (e) L4 and (f) L5 are made zero. 58

3.5 (a) Original image and reconstructed images when coefficients of subband (b) H2, (c) V2 and (d) D2 are made zero. Only small section of the image is shown for better visualization. 61

3.6 (a) Original image and reconstructed images when subband coefficients of (b) L1, (c) L2, (d) L3, (e) L4 and (f) L5 are made zero. 64

3.7 (a) Original image and reconstructed images when subband coefficients of (b) L1, (c) L2, (d) L3, (e) L4 and (f) L5 are made zero. 65

3.8 (a) Original image and reconstructed images when subband coefficients of (b) L1, (c) L2, (d) L3, (e) L4 and (f) L5 are made zero. 66

3.9 (a) Original image (b) Background retinal image (c) Initial vessel image (after background subtraction and normalization). 68

3.10 (a) Initial vessel image (b) Histogram and threshold selection and (c) Thresholded vessel image. 70

3.11 (a) Image showing initial vessel map (b) Thresholded vessel image (c) Mask image (d) Mask multiplied vessel image (e) Vessel map after length filtering and (f) Segmented vessel map after morphological processing. 71

3.12 (a) Original image (b) Background image (c) Difference image and (d) segmented image showing the thick vessels. 74

3.13 (a) Original image (b) Background image (c) Difference image and (d) segmented image showing the thin vessels. 75

3.14 (a) Original image (b) ground truth (GT) image. 76

3.15 (a) Original and reconstructed OD images when subband coefficients of level (b) L1, (c) L2, (d) L3, (e) L4 and (f) L5 are made zero. 78

3.16 (a) Original and reconstructed OD images when subband coefficients of level (b) L1, (c) L2, (d) L3, (e) L4 and (f) L5 are made zero. 81

3.17 Macula images (a) Original and when subband coefficients of level (b) L1, (c) L2, (d) L3, (e) L4 and (f) L5 are made zero (images are contrast enhanced for better visualization). 87

3.18 (a) Original and reconstructed macula images when subband coefficients of level (b) L1, (c) L2, (d) L3, (e) L4 and (f) L5 are made zero. 88

4.1 Characteristics of weight factor given by Equation (4.6). 93

4.2 Characteristics of RSME weight factor. 94

4.3 Characteristics of weight factor for blood vessels. 96

4.4 (a) Image of subband V2 (b) mask image. 97

4.5 Average modified weight factor. 98

4.6 Characteristics of RSME weight factor. 98

4.7 The OD regions (black square) in (a) original image (b) subband V1 (b) subband V2. 99

4.8 Characteristics of the actual and modified weight factors for the optic disc . . . 99

4.9 Average modified weight factor. 101

4.10 Average modified weight factor. 103

4.11 (a) Original image showing the two thick vessels (b), (c) and (d) processed images showing increased distortion in the thick vessels. 105

4.12 Behavior of (a) WMSE, (b) Rel WMSE and (c) RNWMSE at different decomposition level, when the distortion is progressively increased in the thick vessel. x-axis indicates increase in the smoothness (σ) 106

4.13 (a) Original image showing the OD (b), (c) and (d) processed images showing increased distortion in the OD. 108

4.14 Behavior of WMSE, Rel WMSE and RNWMSE at different decomposition levels: x-axis indicates the increase of smoothness (σ). 109

4.15 Weighted distortion measures under subbands zero condition (a) weighted with actual weight values and (b) weighted with modified weight values. 112

4.16 Retinal image showing different regions. 112
4.17 (a) A section of thick vessel (original) (b) Thick vessel after smoothing (reconstructed). 115
4.18 The gray level profile(vessel 1) of original vessel. The intensity profile flattens (vessel 2 to vessel 5) for increasing smoothness. 116
4.19 (a) Original image (b) image showing distortion in thin vessels. 116
4.20 (a) Original image, (b) image with distortion in clinically nonsignificant region, (c) clinically nonsignificant region and (d) distortion in clinically nonsignificant region. 117

5.1 Dependance of image quality on distortion parameter σ for Gaussian blur distortion. 131
5.2 A general logistic curve. 136
5.3 Scatter plots showing the nonlinear fit using the logistic function for the a) MSE (b) PSNR (c) SSIM (d) MS-SSIM (e) IFC (f) VIF (g) VSNR and (h) WWDM versus DMOS. Each data point represents one distorted image. 143
5.4 Prediction performance of the objective quality measures. 146

A.1 Retinal image (DRIVE database) with microaneurysms and hemorrhages. 157
A.2 Retinal image showing drusen. (The image is obtained from a local eye hospital, Sankaradeva Netralaya) 157
A.3 (a) Normal OD (b) OD showing increased size of the cup in case of glaucoma (http://optic-disc.org). 158

List of Tables

2.1 Mean Opinion Score (MOS) and its description 21

2.2 Image Quality Measures 23

3.1 Average Values of PSNR, LMSE and SSIM index at optimum decomposition level. 55

3.2 SSIM index values for blood vessels in different directions 62

3.3 Vessel classification table 73

3.4 Performance results on test images of DRIVE database 77

3.5 Average SSIM values for the optic disc region 80

3.6 Average SSIM values for the macula region 82

4.1 Performance of the wavelet based distortion measures when macula of the retinal image is distorted 109

4.2 Performance of the proposed measure when a particular decomposition level (L) subbands are zeroed 113

4.3 Performance of the proposed measure when only thin vessels are distorted 117

4.4 Distortion in clinically nonsignificant regions 118

4.5 Performance of the proposed $WWDM_v$ when other features of retinal image are distorted 119

4.6 Performance of the distortion measure $WWDM_d$ when only OD is distorted . . . 120

4.7 Performance of the proposed $WWDM_d$ for different cases 122

4.8 Performance of the distortion measure $WWDM_m$ when only macula is distorted 123

4.9 Performance of the proposed $WWDM_m$ for different cases 123

4.10 Performance of the proposed WWDM 125

5.1 Image quality assessment (IQA) algorithms under test 134

5.2 Pearson linear correlation coefficient(PLCC) after nonlinear regression 145

5.3 Spearman rank order correlation coefficient(SROCC) after nonlinear regression . 145

5.4 Root mean squared error (RMSE) after nonlinear regression 146

5.5 Outlier ratio (OR) after nonlinear regression 146

5.6 ANOVA results (F-scores) for all the measures and for different distortions . . . 147

B.1 Format for giving the MOS 161

List of Abbreviations

A	Approximation subband
ARMD	Age Related Macular Degeneration
Acc	Accuracy
ANOVA	Analysis of Variance
BMP	Bit Map image file
CR	Compression Ratio
CFOV	Circular Field of View
CDR	cup-to-disc ratio
DR	Diabetic Retinopathy
DCT	Discrete Cosine Transform
DFT	Discrete Fourier Transform
DWT	Discrete Wavelet Transform
DICOM	Digital Imaging and Communication in Medicine
DRIVE	Digital Retinal Images for Vessel Extraction
D	Wavelet subband in the Diagonal direction
DD	Disc Diameter
DSCQS	Double Stimulus Continuous Quality Scale
DMOS	Difference Mean Opinion Score
$DMOS_p$	Predicted Difference Mean Opinion Score
DF	Degrees of Freedom
FDOG	First Order Derivative of the Gaussian
FOV	Field Of View

FPR	False Positive Rate
FP	False Positive
FN	False Negative
GT	Ground Truth
Gblur	Gaussian blur
HVS	Human Visual System
H	Wavelet subband in the Horizontal direction
ISC	Image Structure Clustering
IDWT	Inverse Discrete Wavelet Transform
IFC	Information Fidelity Criterion
ISI	Image Structure Invariants
IQA	Image quality assessment
JPEG	Joint Photographic Experts Group
JPEG 2000	Joint Photographic Experts Group 2000
kNN	k- Nearest Neighbor
LMSE	Laplacian Mean Square Error
LZW	Lempel-Ziv-Welch algorithm
LSC	List of Significant Coefficients
LIC	List of Insignificant Coefficients
LIS	List of Insignificant Sets
LUT	Look Up Table
L1	Wavelet decomposition Level-1
L2	Wavelet decomposition Level-2
L3	Wavelet decomposition Level-3
L4	Wavelet decomposition Level-4
L5	Wavelet decomposition Level-5
MF	Matched Filter
MAs	Microaneurysms

MSE	Mean Square Error
MOS	Mean Opinion Score
MRA	Multi Resolution Analysis
MSA	Multi Scale Analysis
MS-SSIM	Multi Scale - Structural Similarity Index
NMSE	Normalized Mean Square Error
MS	Sum of Squares of the Means
OD	Optic Disc
OR	Outlier Ratio
PCA	Principal Component Analysis
PDM	Point Distribution Model
PSNR	Peak signal to Noise Rtaio
PACS	Picture Archiving in Communication Systems
PLCC	Pearson Linear Correlation Coefficient
Q_G	Total number of Quality Groups
RMSE	Root Mean Square Error
Rel WMSE	Relative Wavelet subband Mean Square Error
RNWMSE	Root of the Normalized Wavelet subband Mean Square Error
RSME	Relative Subband Mean Energy
SSIM index	Structural Similarity Index
SPIHT	Set Partitioning in Hierarchical Trees
Se	Sensitivity
Sp	Specificity
SROCC	Spearman Rank Order Correlation Coefficient
SS	Sum of Squares
TIFF	Tagged Image File Format
TPR	True Positive Rate
TP	True Positive

TN	True Negative
V	Wavelet subband in the Vertical direction
VQEG	Video Quality Experts Group
VSNR	Visual Signal to Noise Ratio
VIF	Visual Information Fidelity measure
WIQM	Wavelet based Image Quality Measure
WNMSE	Wavelet based Normalized Mean Square Error
wRel WMSE	Weighted Relative Wavelet subband Mean Square Error
$WWDM_f$	Wavelet Weighted Distortion Measure for a retinal Feature
$WWDM_v$	Wavelet Weighted Distortion Measure for the blood Vessels
$WWDM_d$	Wavelet Weighted Distortion Measure for the optic Disc
$WWDM_m$	Wavelet Weighted Distortion Measure for the Macula
WWDM	Wavelet Weighted Distortion Measure
WMSE	Wavelet subband Mean Square Error
wWMSE	Weighted Wavelet subband Mean Square Error
WGN	White Gaussian Noise

List of Symbols

A	ANOVA data matrix
b	Wavelet subband
β_1, β_2,β_3	Regression model parameters
c	Contrast component
$C(X)$	RMS contrast of the image X
$C(e)$	RMS contrast of the error (distortion) e
$d_{b,n}$	Wavelet (detail) coefficient of the original image
$\tilde{d}_{b,n}$	Wavelet (detail) coefficient of the processed image
Δ	Laplacian operator
DF	Degrees of freedom
$\Delta_{\mathbf{e}}$	Error vector
e	Error between the subbands
E	Energy of a subband
$\bar{E}$	Mean energy of a subband
$\bar{E}_{tot}$	Total subband mean energy
g, h	Quality groups
Γ_f	Diagonal weight matrix
h	Quality group
i	i^{th} sample
I	Mutual information
j	Any given scale
J	Highest scale

k	Coefficient of a subband
K	Total number of coefficients in a subband
l	Luminance component
μ	Mean
M	Objective measure
n	Any given decomposition level
N	Final decomposition level
NL	Number of lowpass filters
NH	Number of highpass filters
N_o	Order of a wavelet filter
N_{or}	Order of the reconstruction filter
N_{od}	Order of the decomposition filter
$\phi(x)$	Scaling fucntion
$\psi(x)$	Wavelet fucntion
Q	Quality level of JPEG compression
q	Quality score
Q_G	Total number of quality groups
r	Rank difference
ρ	Relative subband mean energy
s	Structural component
σ^2	Variance
σ	Standard deviation
S	Total number of test (distorted) images
S_G	Total number of sample points in a group
θ	Orientation of a subband
T_H	Threshold
t	Session
T	Total number of sessions

v	Viewer (observer)
V	Total number of viewers
ω	Weight facor for a subband
X	Original image
Y	Reconstructed (distorted) image

1

Introduction

Contents

1.1 Retinal image and its clinical features 4
1.2 Retinal image processing 6
1.3 Image quality measures 13
1.4 Quality analysis of retinal images 15
1.5 Scope for the present work 17
1.6 Organization of the thesis 18

Medical imaging is a modern health care procedure. It has become important not just because of the visual documentation but for its ability to extract information about many diseases. The exploration of visual information can lead to evidences for the diagnosis of a disease. Recent advances in medical imaging technology have made it possible to obtain high resolution images of body structures. These accomplishments have allowed clinicians to make accurate and efficient diagnoses in a noninvasive fashion. Medical imaging can also be used for the study of normal anatomy and physiology. The progress in the computing power and communication technology have resulted in digital displays of data making the *picture archiving and communication system* (PACS) and *teleradiology* possible. With medical imaging playing an increasingly prominent role in the diagnosis and treatment of diseases, the challenging problem of extracting clinically useful information about anatomical structures has become important [1].

The human eye is like a camera. In Figure 1.1, a cross section of the human eye is shown with important anatomical components. Each part plays a vital role in providing clear vision. Light comes in through the iris and is focused onto the retina through a lens. The retina is a membrane containing photoreceptor nerve cells that lie in the inside back wall (the fundus) of the eye. The photoreceptor nerve cells of the retina change the light rays into electrical impulses and send them through the optic nerves to the brain where an image is perceived. Ophthalmic photography is a specialized form of retinal imaging dedicated to the study and treatment of eye related diseases. There are two common procedures to perform such photography: (a) *angiography* and (b) *fundus photography*.

The ophthalmic photography may be performed after the injection of a fluorescent dye into the bloodstream via a vein in the patient's arm. Such a procedure is called Fluorescein Angiography. With special colored filters, only the dye is photographed as it travels through the vessels in the retina. This image is generally known as fluorescein image or fluorescein angiogram. Figure 1.2 shows an example of a fluorescein angiogram. This may detect and quantify changes in blood vessels more accurately than direct ophthalmoscopy due to the better contrast between the blood vessels and background retina layer. But it is not a very commonly used technique in clinical practice because it is invasive in nature.

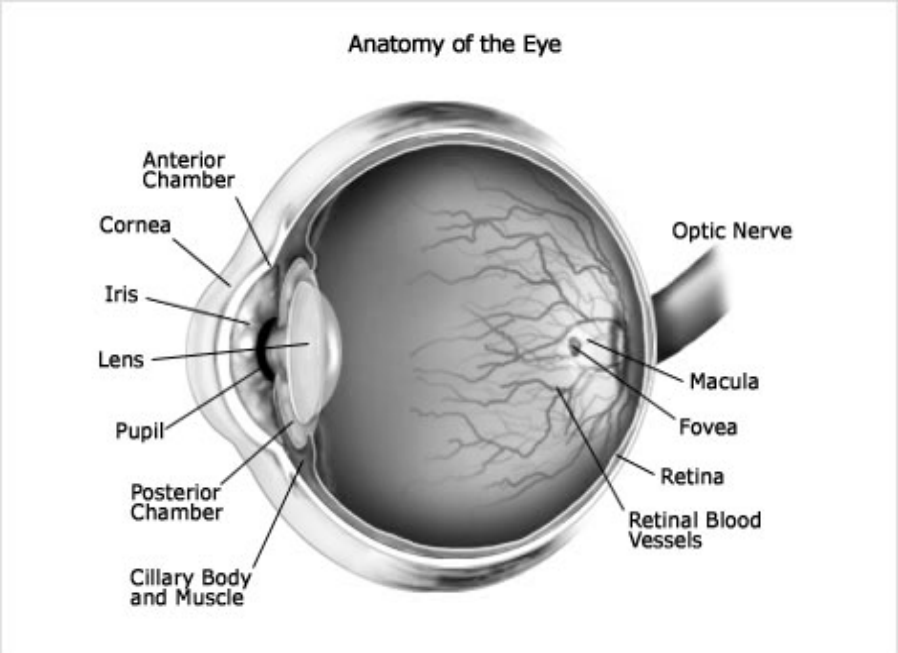

Figure 1.1: A cross sectional view of the eye. (http://www.healthtree.com/articles/anatomy/eye/)

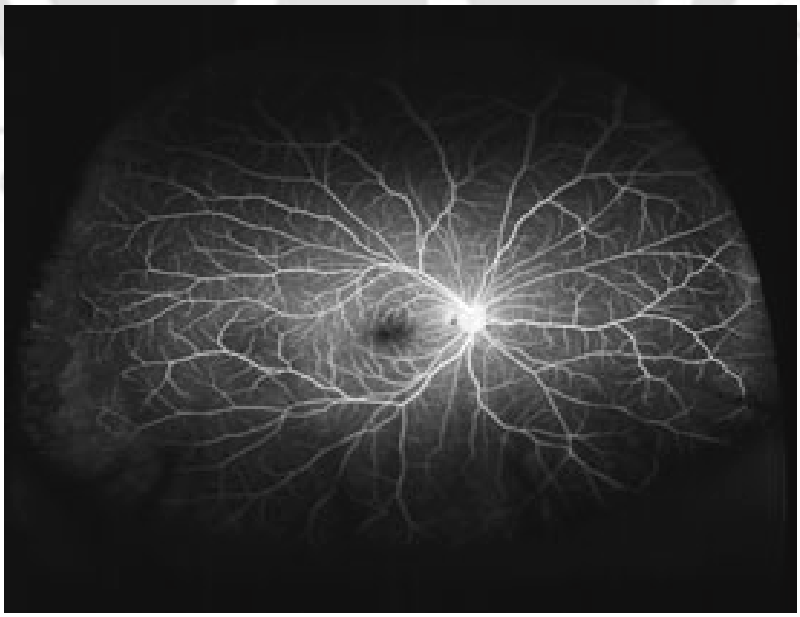

Figure 1.2: Fluorescein Angiogram (http://www.revophth.com).

In fundus photography, a digital fundus camera is used to capture color retinal images. A fundus camera is a special type of low power microscope with an attached camera designed to photograph the interior surface of the eye, including the retina, the optic disc and the macula. There are two common types of fundus microscopes - *mydriatic* and *non-mydriatic* [2]. Mydriatic instruments are designed assuming that the eyes have been dilated. The non-mydriatic instruments do not require dilation. The mydriatic instruments produce higher quality images due to the wider field of view enabled by dilation. Fundus cameras are used by optometrists, ophthalmologists, and trained medical professionals for monitoring progression of a disease, diagnosis of a disease or in screening programs, where the photos (images) can be analyzed later.

1.1 Retinal image and its clinical features

A digital retinal image is shown in Figure 1.3. The area of the retina shown in this image is only a small part of the complete retina which is much larger. The dark, central retinal area is called the *macula*. The center of the macula is the *fovea*, a small dip which contains the highest concentration of photosensitive cells. This is responsible for sharp central vision and reading vision. The peripheral retina is responsible for the peripheral vision. Other important structures of the retina are the *optic disc* (OD) and the *blood vessels*. The optic disc is a region in the back of the eye where the optic nerve enters the eye. This also corresponds to the blind spot since there are no photosensitive cells in this location. The optic nerve is the structure which takes the information from the retina as electrical signals and delivers it to the brain where this information is interpreted as a visual image. The blood vessels radiating out from optic disc and spreading in the whole retina supply blood to nourish the inner retinal layers. Retinal arteries and veins are visible as dark linear branched structures.

1.1.1 Clinical importance of retinal images

Retinal diseases affect millions of people all over the world. Early detection of retinal problems is critical for successful treatment. Screening is the simple procedure to detect retinal disorders.

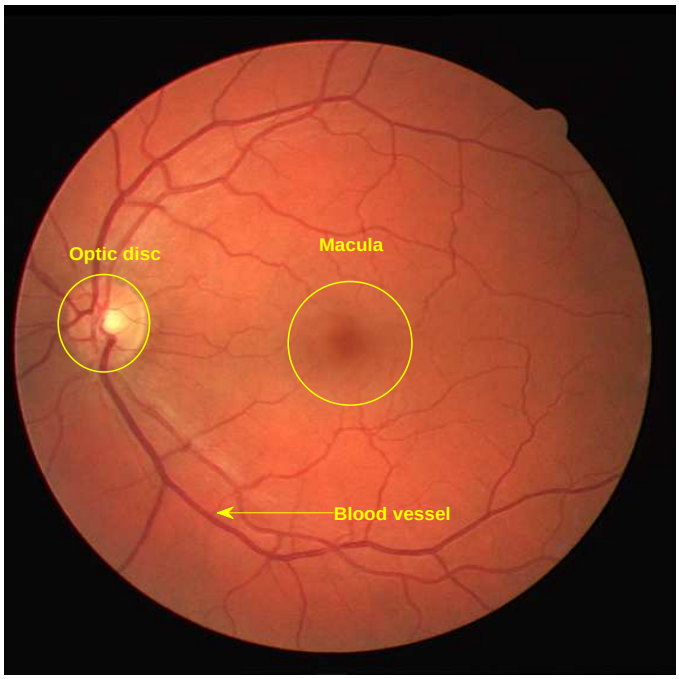

Figure 1.3: Digital retinal photograph from DRIVE database.

Retinal images have the potential to facilitate early detection of retinal pathologies. The retinal images provide critical diagnostic information in common disorders, such as diabetes, glaucoma and macular degeneration.

An ophthalmologist examines the retinal image features - the blood vessels, the optic disc and the macula for any possible indication of pathological conditions. Diabetes is a major medical and social problem affecting more and more people every year. A common complication of diabetes affecting the blood vessels in the retina is the *diabetic retinopathy* (DR) [3]. There are multiple eye diseases that affect the vasculature in the eye, particularly the blood vessels of the retina. These diseases can cause physical changes in the width, color and path of the vessels [4–6]. The early stages of DR are marked by retinal vascular changes like, growth of new vessels, increased vessel tortuosity, venous beading and microaneurysms [7, 8]. There are also systemic diseases that affect the blood vessels in the entire body. The eye is the only place for a physician to directly observe blood vessels in vivo. The retinal vasculature offers a

unique opportunity for a physician to gain valuable clues for detecting and diagnosing systemic diseases. It has been found that the increased artery dilation due to hypertension is more in the eye compared to that in the other parts of the body [9]. Blood vessels are also used as landmarks for the registration of retinal images of the same patient collected at different visits [10].

The OD appears as a bright yellowish or white region in color retinal images. Its shape is more or less circular, interrupted by the outgoing vessels. The morphological changes at the optic nerve head or OD and the loss of optic nerve function in the form of visual field defects mark a pathological condition called glaucoma. Hence, it is important to identify and quantify the structural changes that occur early in the disease [11]. The OD also acts as a landmark to detect other features like the blood vessels and the macula [12].

The study of the macular region may provide a means to detect and diagnose macular abnormalities. Many conditions leading to blindness are associated with pathologies of the macular region. These include age-related macular degeneration (ARMD), diabetic macular edema, macular hole, etc [13, 14]. Patients suffering from macular diseases may experience the blurring of central vision.

Hence, the development of computer technologies for studying these structures may help in early diagnosis of various retinal diseases. The modern research has been focussed on ways to enhance informativeness and develop objective methods of early diagnostics.

1.2 Retinal image processing

Retinal imaging and image processing play a crucial role in the care of patients with retinal diseases. The development of new imaging technologies offers very high resolution digital images that are needed for clinical applications. The digital retinal images can be subjected to image analysis for quantitative measurements of the retinal features. This quantitative analysis can be used as a research tool to better understand the relationship between the retinal components and the eye related diseases.

The retinal image analysis includes:

- segmentation of anatomical structures - blood vessels, optic disc and macula;
- detection of abnormalities - microaneurysms, hemorrhages and neovascularizations.

1.2.1 Segmentation of anatomical structures in retinal images

An efficient segmentation of anatomical structures in retinal images is an important step in retinal image analysis [15]. This section presents various algorithms proposed for the segmentation of blood vessels, the optic disc and the macula.

1.2.1.1 Segmentation of retinal blood vessels

Automatic detection of blood vessels is a challenging problem because of the low contrast between the vessels and the background. The presence of pathological features may cause further difficulty in detecting the blood vessels. A number of approaches have been reported in the literature to solve this problem. They can be classified into *unsupervised* and *supervised* methods. In an unsupervised method, several predefined criteria are considered to classify a pixel as a candidate blood vessel pixel. The unsupervised methods include the popular matched filtering [16–18], mathematical morphology [19, 20], vessel profile tracking [21] and multiscale [22, 23] based approaches for vessel segmentation and analysis of retinal images.

The *matched filter* (MF) method [16] is a simple and effective method to detect and segment retinal vessels. Considering the piecewise linear approximation of blood vessels and Gaussian intensity cross section profile, a series of filters with different orientations are used to match the vessels. The blood vessels are detected by thresholding the MF response image. However, the MF will have strong responses to not only vessels but also nonvessel edges and hence many false detections may result. A threshold probing technique was proposed to improve the accuracy of MF method by analyzing the region-based attributes of the vessel network structure. This method showed improved performance in recognizing small vessels and the results of this work are used as benchmark for performance evaluation [17]. But this method requires the MF response image as the input. An extension and generalization of MF was considered in [18] for the detection of blood vessels. The authors used a pair of filters, the zero-

mean Gaussian filter and the first order derivative of the Gaussian (FDOG). The detection of blood vessels in a noisy environment using mathematical morphology was investigated in [20]. The vessels are assumed to be a set of piecewise linear and locally connected elements. A cross-curvature evaluation is performed to further distinguish vessels from similar background patterns. The method of blood vessel tracking in [21] is applied to find an average diameter of the blood vessel over a length. Two Gaussian functions are used to model the vessel profile. Following the direction of vessel axis, the variation of of vessel diameter has been described based on the parameters of modeled intensity distribution at every cross sectional point. The quantification of varying vessel diameters may be useful for the study and diagnosis of vascular diseases. The technique implemented in [23] examines multiscale derivatives of the intensity profile for retinal vessel segmentation. In this implementation, vessels are segmented pixel by pixel using a nondirectional region growing algorithm based on edge and ridge strength. This approach avoids many of the problems that exists in image filtering and profile tracking. Better segmentation results were obtained but the method took longer time to process each image.

The supervised methods exploit some prior information to decide if the pixel belongs to a vessel or not [24–27]. In this approach, each image pixel is represented by a *feature vector*. Then a classifier is trained with these feature vectors. A supervised method proposed in [24] for blood vessel segmentation is based on pixel classification. The feature vector is formed using the various filter outputs. The features consist of the output of the Gaussian filter and its derivatives up to order 2 and at five different scales augmented with the original green channel image intensity values. The k-nearest neighbor (kNN) classifier results in a pixel probability map. A binary segmentation of the vasculature was obtained after thresholding the probability map.

A ridge based algorithm is used to detect vessels in a retinal image [25]. Ridges are the points that have an extremum in the direction of the largest surface curvature. After the ridges are computed, points belonging to the same ridges are grouped together. Grouping is done by applying a simple region growing algorithm. A set of features including width of the vessel, intensity and edge strength are extracted for all grouped ridge pixels. Then a feature selection

scheme is used to select those which provide the best class separability. A kNN classifier is used on this set of features to classify the ridges into two classes- the vessels and the background.

The Gabor wavelet transform is used in [26] for blood vessel segmentation. The Gabor wavelet can be fine tuned to specific frequencies and is more sensitive in detecting the directional features. The maximum modulus of the wavelet transform over all angles for multiple scales are taken as pixel features. Normalized feature vectors are given as input to the Bayesian classifier to obtain the vessel segmentation. As supervised methods are designed based on preclassified data, generally their performance is better than that of unsupervised ones. They can produce good segmentation results but at the cost of computational complexity.

The analysis of blood vessel structure also helps in separating the arteries and veins [28]. The study of relative diameters of arteries and veins shows the risk of systemic diseases such as stroke, hypertension or myocardial infarction.

1.2.1.2 Segmentation of the optic disc and fovea

The optic disc (OD) is considered as one of the main features of a retinal fundus image. The OD often serves as a landmark for other fundus features. The change in the shape, color or depth of the OD is an indicator of various ophthalmic pathologies especially for *glaucoma*. Localizing the OD automatically and efficiently is not an easy process, since the appearance of the OD may vary significantly due to retinal pathologies.

The OD is detected by identifying the area with the highest average variation among adjacent pixels using a window size equal to that of the OD [29]. The images were preprocessed using an adaptive local contrast enhancement method which was applied to the intensity component. But the concept of average intensity variation may not be satisfied when bright abnormalities are present. Hence in [30], the OD center is approximated as the center of the largest of the brightest connected object in a retinal image. Then a binary image including all the bright regions is obtained by simply thresholding the intensity image.

The concept of average brightness is used in [31] to find the OD candidate regions for their model-based approach. Pixels with the highest 1% intensity levels were selected. The selected

pixels were then clustered. Only large clusters were retained and small clusters were discarded. A model for OD was created by applying the principal component analysis (PCA) to a training set of 10 intensity normalized square subimages manually cropped around the OD. Then for each pixel in the candidate regions, the PCA transform was applied through a window with different scales. The OD was detected as the region with the smallest Euclidean distance to its projection onto the OD model.

A recent technique that reduces the dimensionality of the search space is proposed in [32]. It uses the projection of the 2-D image feature space onto two orthogonal axes. This gives two 1-D signals that can be used to determine the two coordinates of the OD. The retinal vessels' orientation, the OD brightness and shape are used as the image features that help differentiate the OD from the background.

The fovea is a darker area located in the center of retina. It is responsible for sharp central vision. Localizing the macula, especially the location of the fovea may potentially be useful in improving the detection of subtle cases of DR and ARMD. Detection of the fovea has received less attention, likely due to the fact the fovea is harder to detect and does not feature any high contrast structures.

The increased pigmentation around the fovea is used to detect its location using a template matching technique in [29]. The region of interest was searched for the darkest area in the neighborhood of the optic disc. The detection performance of 80.4% on 100 images was reported. Following the similar method to find the fovea, the authors of [31] have used the additional information of the locations of vascular arch. This helps reduce the search area. A detection performance of 100% for the fovea is reported on 89 images.

An automated method to detect the location of the optic disc and fovea is presented in [33]. The method uses an optimization technique to fit a point distribution model (PDM) to the fundus image. After fitting, the points of the model indicated the location of the normal anatomy. The method requires the vascular arch to be at least partially visible but works on images centered on the fovea as well as centered on the optic disc. This method was able to find the fovea location in 94.4 % and the optic disc in 98.4% on 500 images.

A similar method for the fovea centered images was presented by [34]. After detecting the vascular arch, the optic disc is found using a Hough transform and the fovea is detected by template matching where the template was derived from a set of training images.

A fully automated, fast method to detect the fovea and the optic disc in digital color photographs of the retina is presented in [35]. The method makes few assumptions about the location of both structures in the image. The problem of localizing structures in a retinal image is considered as a regression problem. A kNN regressor is utilized to predict the distance in pixels in the image to the object of interest at any given location in the image based on a set of features measured at that location. The method combines cues measured directly in the image with cues derived from a segmentation of the retinal vasculature. A distance prediction is made for a limited number of image locations and the point with the lowest predicted distance to the optic disc is selected as the optic disc center. Based on this location the search area for the fovea is defined. The location with the lowest predicted distance to the fovea within the foveal search area is selected as the fovea location.

1.2.2 Detection of abnormalities

The retinal image analysis offers the advantage to perform automated screening for conditions of diabetic retinopathy (DR). This helps to reduce the workload required from manual trained graders. The detection of DR concentrates largely on the automated detection of *microaneurysms* (MAs), *haemorrhages* and *exudates*. The MAs detection program applied on angiogram images was first described in [36]. The retinal images were processed by improved techniques for shade correction and used the top-hat transformation to remove the blood vessels and other distracters. The Gaussian filters were used to retain candidate MAs for subsequent classification.

To detect the abnormalities in case of early DR, various processing methods including image enhancement, noise removal and image normalization in combination with pattern recognition were employed in [37]. The number of detected microaneurysms/haemorrhages from 428 retinal images were compared with the results of two expert human graders.

An iterative region growing technique with adaptive intensity thresholding was performed in [38] to effectively detect MAs and haemorrhages. The pixels within a certain boundary and having similar intensity values are grouped as a region. The major structures of the retinal image (optic disc, blood vessels and fovea) were also segmented to improve the detection of abnormality features. A new technique called a 'Moat operator' which creates a trough around lesions was used to automatically detect the features of DR. The algorithm was applied on a set of 30 retinal images of which nine were normal and other images had pathological features.

A hybrid scheme that used both the top-hat based method as well as a supervised pixel classification based method is presented in [39]. This scheme is proposed to detect the MAs in color fundus photographs. This method was also used for the detection of hemorrhages in addition to the MAs. More number of features, including the color information were added to the candidate extraction process compared to those of the previous works. With this large set of features, a supervised classifier is used to distinguish the real and spurious candidate lesions. A set of 100 images taken from a screening program were used to test the proposed method.

A study was made in [40] to assess whether automated identification of DR based on the presence of MAs is an effective tool in clinical practice. Five optometrists were employed to assess the DR in the 758 retinal images of 385 patients obtained in a clinic. Then the performance of the automatic DR detector was compared with the experts' assessment.

The approach of [41] finds the MAs directly using template matching in wavelet subbands. In this approach, the optimal adapted wavelet transform is found using a lifting scheme framework. By applying a threshold on the matching result of the wavelet template, the MAs are labeled. Results were evaluated on 120 retinal images and compared to the analysis made by experts.

An automated system to detect DR by segmenting the possible MAs, haemorrhages and exudates in color retinal images was described in [3]. The system performs preprocessing, identification of normal structures, identification and extraction of candidate DR features. The classification of candidate features as true features or noise was done using artificial neural networks. To use this system as a tool for DR screening, the images are classified as normal or abnormal according to the presence or absence of MAs. The system was evaluated by comparing

its performance with a human grader on a set of 773 retinal images.

A new approach for automatic detection of MAs from color retinal images was proposed in [42]. The detection of MAs is considered as a problem of target detection from clutter where the probability of occurrence of target is considerably low compared to the clutter. The number of clutter responses were gradually reduced by rejecting the clutter successively. The processing stage passes majority of the MAs while rejecting the clutter. The technique uses a specific set of features to accept the true MAs. A final score is assigned to the retained MAs based on the similarity to a true MAs. The results are evaluated using two publicly available datasets and the the dataset built by the authors.

1.3 Image quality measures

Image quality measures are used to evaluate the performance of image processing techniques. Image quality evaluation can be done either subjectively or objectively. *Subjective image quality* evaluation is the most accurate and reliable way of assessing the quality of an image. However, this method is slow, inconvenient and expensive for practical usage. Thus, *objective image quality* metrics that can automatically predict the perceived image quality are preferred [43]. The objective quality measures are simple to compute and useful in many ways. The commonly used mean square error (MSE), root mean squared error (RMSE), normalized mean squared error (NMSE) and the peak signal-to-noise ratio (PSNR) are computed by averaging the squared intensity differences of reference and distorted image pixels. But the drawback of the squared error measures is that, a slight spatial shift of an image may cause a high numerical distortion but no perceptible distortion. Conversely, a small average distortion may result in a severe visual artifacts if all the error is concentrated in a small important region. Therefore, their predictions of the image quality often do not agree well with the perceived quality by humans [44]. They characterize the distortions globally and thus fail to reflect spatial variations in image quality. These difficulties have motivated the researchers to develop the human visual system (HVS) based quality measures.

The HVS-model based approaches show significant improvement in their performance. But

they are more complex to implement. The structural similarity (SSIM) index [45] is proposed based on the assumption that the HVS is highly adapted to extract structural information from the viewing field. The SSIM index is computed locally and then averaged to obtain a single mean SSIM index value. The information theoretic approaches [46, 47] attempt to quantify the information loss by measuring the mutual information between the distorted and the reference images. In this method, the distorted and reference images are considered to be two random samples. Then, the mutual information is computed as the distance between the distributions of the images.

1.3.1 Wavelet based medical image analysis

In many image processing applications, mathematical transformations are applied to an image in order to extract information which may not be readily available from the original image. The discrete wavelet transform (DWT) offers an efficient representation of the signal, finely tuned to its intrinsic properties. One of the most important features of wavelet transforms is their *multiresolution* representation [48]. The wavelets are able to handle spikes and discontinuities better than the conventional Fourier analysis [49]. This makes them a perfect tool for traditional image processing applications.

The important aspect of medical images is that the information of interest is often a set of features that are spatially localized. The wavelet transform is an effective method to highlight these space localized features. The research article [50] describes the application of wavelet transforms for noise reduction in magnetic resonance imaging (MRI) images. Since then, wavelet transforms have been successfully used in many applications including image analysis, image compression, image enhancement, image segmentation and multiscale image registration [51–53]. The summary and overview of research works related to wavelets in medical image processing from the past few years is given in [54–56].

1.4 Quality analysis of retinal images

In medical image computing, the evaluation of image quality is a major concern [1]. The initial approaches for retinal image quality have focused either on the global intensity histogram [57] or on the local intensity histogram in combination with global edge histogram [58]. In the former method, a template intensity histogram is generated using twenty excellent quality retinal images. The target image quality is evaluated by correlating its histogram with the template histogram. A quality index Q is used to define the quality of the given image. To make the quality assessment a little more strong compared to [57] , the global edge histogram is combined with the local intensity histogram [58]. Using these two features, the images were classified into good, fair and bad quality images. But these methods rely on one mean histogram and do not consider the natural variations in different quality images.

The quality assessment method in [59] considers the relationship between image blurring and visibility of blood vessel features. The image quality is assessed by estimating the total vessel area. If the image is out of focus or blurred, the smaller vessels are not visible. The images are classified into good and poor quality images by applying a threshold. But this method fails if the main thick vessels carry significant area and satisfy the threshold.

The image quality in retinal images is defined using the concept of image clarity and field definition [60]. The visibility of macular vessels was considered as an indication of image clarity. The image that shows the full 45° field of view (FOV), optic disc and macula was defined as an image with adequate field. The overall image quality is evaluated by combining these two features. This method requires the segmentation of retinal components and hence computationally expensive.

The performance of the image quality assessment method can be improved by training the system to learn important structures in the retinal image [61–63]. A supervised method is proposed in [61] to classify the low quality images. This method employs the Red Green Blue (RGB) color information and second order image structures. These image structures are obtained by employing a set of filters. The image structures are grouped using a clustering al-

gorithm. This procedure is called *image structure clustering* (ISC). The filter output computed for each pixel is considered as a feature vector. Then the raw color information is combined with this feature vector and a classifier is trained with this combined feature vector. The classifier output distinguishes the normal images from low quality images.

The retinal image quality assessment defined in [62] was based on the strength of the blood vessel segmentation algorithm. To make the algorithm fast and robust, local vessel densities are extracted using local polar windows. This local information is combined with the original RGB color information to form a feature vector. The classifier takes the feature vector as input and categorizes the images into good, fair and bad quality images.

The recent method of retinal image quality assessment [63] is inspired by the diagnosis procedures based on the opinion of a retinal specialist. The retinal image quality is evaluated considering the optic disc and blood vessel structures as well as general characteristics of texture, homogeneity and contrast. The structures are grouped as in ISC [61]. The image quality assessment is performed by combining this global clustering with local general features.

Retinal images are processed for efficient storage and transmission in some applications such as PACS or telemedicine. This causes the distortion and degrades the quality of the retinal images. The primary consideration here is, the retinal experts must be able to make diagnosis from an image that has been processed. Various methods discussed above have investigated the quality of individual retinal images (fundus photograph). But there is a limited research effort in the direction of evaluation of processed (compressed) retinal images [64–69].

Different studies have been made to investigate the effect of compression on retinal image quality and automatic analysis of retinal images. The digital retinal image is compressed using the Joint Photographic Experts Group (JPEG) and DWT based methods. Automatic counting of MAs was considered before and after compression [64]. It was observed that the image quality degrades with the increase in the compression ratio and affects the number of MAs detected. The influence of compression on retinal image was examined for various applications like, the diagnosis of glaucoma [66] and diabetic retinopathy [65, 67–69].

1.5 Scope for the present work

Analysis of retinal image features is important for detecting eye related diseases. The retinal image should be of sufficient quality to ensure reliable diagnosis. Various approaches have been proposed to study the clinical usefulness of the retinal image for different applications [60–63]. But these methods evaluate the quality of a single retinal image. In some cases retinal images need to be processed for efficient storage and transmission. Any such processing may cause differences in the quality of the image features. The literature related to retinal image processing focus on how the distortion affects the retinal images for clinical applications [64, 66]. But the issue of quantifying the image distortion has not been addressed.

There are several traditional objective distortion measures that are widely used [43]. They are simple and easy to compute. These measures estimate the distortion on a pixel-by-pixel basis. They do not consider the influence of artifacts on some important image content like the clinical features. Such measures treat the distortions in the clinically important regions and nonsignificant regions the same way. This limitation indicates the need for diagnostically meaningful distortion measures. In a retinal image, the features like blood vessels, optic disc and macula constitute the diagnostically important components. The distortion measure for retinal images is expected to emphasize any distortion in these diagnostic features.

The *multiresolution analysis* (MRA) technique helps produce localized image features with good *space-frequency resolution* [48, 70]. This can be explored for localizing the retinal image components. The MRA property of the DWT allows improvement in the detection of features at specific resolution. The recent compression techniques for medical images such as *JPEG2000* and *DICOM* (Digital Imaging and Communication in Medicine) [71,72] use the DWT. A wavelet based quality measure may be useful for defining the image quality. The available literature on the distortion measures in the transform domain are defined for multimedia images.

The retinal image is decomposed into several subbands using a two dimensional DWT (2D DWT). The image information is spread across different subbands. Out of many subbands, a few subbands may have significant information about the retinal features. A detailed study in

this directions is not available in the literature. Hence a systematic study can be carried out to investigate clinically significant information in different subbands. The results of the investigation about the significant information in different subbands may help to design a variable weighting scheme. This gives scope for defining a diagnostically meaningful distortion measure in the wavelet domain. The individual measures can be defined to quantify the distortion in each of the retinal features. These measures may help to evolve a global distortion measure for the assessment of the clinical quality of the image.

1.6 Organization of the thesis

The organization of the rest of the thesis is as follows: In this chapter, the retinal images are introduced and its clinical importance is discussed. The literature survey of retinal image analysis methods is also presented.

In **Chapter 2**, the literature review on quality assessment of retinal images for different applications is presented. In **Chapter 3**, a brief review of wavelets and wavelet based analysis of retinal image is discussed. This chapter discusses the effect in different subbands due to distortion in clinical features. In **Chapter 4**, wavelet weighted distortion measures are proposed for each of the three retinal features. A global wavelet weighted distortion measure (WWDM) is defined by combining the individual measures to effectively quantify the diagnostic information loss. **Chapter 5** presents a statistical evaluation of a number of image quality measures used to quantify the distortion in retinal images. They are evaluated using different metrics to assess their correlation with human evaluation scores. In **Chapter 6**, conclusions are drawn by summarizing the contributions of the work and mentioning some directions for future work.

2

Review of image quality measures

Contents

2.1	**Image quality measures**	**20**
2.2	**Wavelet based image quality measures**	**25**
2.3	**Quality measures for retinal image**	**31**
2.4	**Motivation for the present work**	**42**

The advanced digital imaging and computing technology has the full potential in modern ophthalmology as it is dependent on digital retinal images [73]. As mentioned earlier, the digital fundus photography is a common procedure in ophthalmology to capture retinal images. The retinal images thus obtained are used by medical experts to diagnose and document diseases like diabetic retinopathy (DR) or glaucoma. Sometimes, the images are further evaluated by automatic analysis tools to support the diagnosis. Good image quality is essential to ensure a reliable diagnosis. There are only a few studies that have been published on the quality assessment of retinal images.

This chapter presents a review on the quality assessment approaches reported in the literature for retinal image. Section 2.1 presents the various conventional measures used for image quality assessment. A brief introduction to the DWT and discussion of DWT-based quality measures is presented in Section 2.2. Section 2.3 gives a description of the methods and different features such as the edge histogram of the blood vessels, area of the main blood vessels, visibility of fine vessels near the macula that are considered in defining the quality of retinal image.

2.1 Image quality measures

Digital images are subjected to a variety of distortions during processing such as compression, transmission and filtering. There is a need to study the effect of these distortions on the image quality. Various quality measures are used for evaluation of distortions in images. They can be broadly classified into *subjective* and *objective* image quality measures.

2.1.1 Subjective measures

Since the human observer is the ultimate receiver to judge the image quality, the most reliable means of assessing image quality is the subjective evaluation. The most frequently used subjective measure is the *Mean Opinion Score* (MOS), obtained from a large population of human subjects [74]. The subjective test is conducted by displaying a pair of images on the screen. The first image is always the original (reference) image without any artifacts and considered

to be of excellent quality. The second image is the reconstructed version of the original which possess some difference with respect to original. The assessor is asked to give the score for the second image taking the first image as reference. The standard 5 level scoring shown in Table 2.1 is used in the subjective evaluation. The image with significant distortion is given a score of 1 and an image with well preserved features is rated high as 5. The effectiveness of an image quality measure is assessed by estimating the correlation with subjective quality scores of the processed images.

The advantage of this method is the true reflection of image quality. But this method is inconvenient, time consuming and expensive. These problems have resulted in an extensive research to develop objective measures for image quality assessment.

Table 2.1: Mean Opinion Score (MOS) and its description

Rating	Image quality	Level of distortion	Effect on clinical features
5	Very Good	Imperceptible	Clinical features are well preserved
4	Good	Perceptible but not annoying	Most of the clinical features are preserved
3	Fair	Slightly annoying	Clinical features are slightly distorted
2	Poor	Annoying	Most of the clinical features are distorted
1	Bad	Very annoying	All clinical features are distorted

2.1.2 Objective Quality measures

A number of mathematically defined measures have been used in the literature for image quality assessment. These include the mean squared error (MSE), the peak signal to noise ratio (PSNR), the root mean squared error (RMSE), normalized absolute error (NAE), laplacian mean squared error (LSME), normalized cross correlation (NCC) and structural content (SC) [43]. Suppose X is the original image and Y is the processed image each of size M×N.

Then the MSE is computed as

$$\text{MSE} = \frac{1}{\text{MN}} \sum_{m=1}^{\text{M}} \sum_{n=1}^{\text{N}} [\text{X}(m,n) \; - \; \text{Y}(m,n)]^2 \tag{2.1}$$

and the PSNR is given by,

$$\text{PSNR} = 10 \log_{10} \frac{(2^b - 1)^2}{\text{MSE}} \quad \text{dB} \tag{2.2}$$

where b is the number of bits used to represent an image pixel. For gray images, b is 8.

Other objective measures used in the image quality assessment are listed in Table 2.2 with their algebraic expressions.

The traditional simple error measures such as the MSE or the PSNR operate on a pixel-by-pixel basis and neglect the important influence of image content and viewing conditions on the actual visibility of artifacts. Hence these measures are inadequate in evaluating the artifacts and their predictions often do not agree well with the perceived quality. Distortions are relatively more disturbing in smooth areas of an image than in texture regions. The pixel-based metrics give equal importance to all the regions. Therefore, the perceived quality of images with the same PSNR can actually be very different [75]. It is observed that a higher PSNR or equivalently, a lower MSE may not necessarily imply a higher subjective image quality. They quantify the distortions globally and thus cannot reflect spatial variations in the image quality. These problems have motivated the research group for the study of vision models. This resulted in the human visual system (HVS) based quality measures.

Image quality assessment can be improved by incorporating some models of HVS into the evaluation process [76]. In recent years, approaches based on HVS-models are slowly replacing the classical numerical quality measures. The quality improvement that can be achieved using an HVS-based approach is significant and applies to a large variety of image processing applications. However, the HVS is complex and many of its properties are not well understood to model it reliably.

The image quality measures developed in [45, 77] do not directly employ the HVS model, but are inspired by the functioning of HVS. The Structural SIMilarity (SSIM) index [45] is a change in the fundamental assumption from the intensity error based image quality measures.

Table 2.2: Image Quality Measures

normalized mean square error, $\text{NMSE} = \frac{\sum_{m=1}^{\text{M}} \sum_{n=1}^{\text{N}} [X(m,n) - Y(m,n)]^2}{\sum_{m=1}^{\text{M}} \sum_{n=1}^{\text{N}} [X(m,n)]^2}$
root mean square error, $\text{RMSE} = \sqrt{\frac{1}{\text{MN}} \sum_{m=1}^{\text{M}} \sum_{n=1}^{\text{N}} (\text{X}(m,n) - \text{Y}(m,n))^2}$
normalized absolute error, $\text{NAE} = \frac{\sum_{m=1}^{\text{M}} \sum_{n=1}^{\text{N}} (\lvert\text{X}(m,n) - \text{Y}(m,n)\rvert)}{\sum_{m=1}^{\text{M}} \sum_{n=1}^{\text{N}} \lvert\text{X}(m,n)\rvert}$
laplacian mean square error, $\text{LMSE} = \frac{\sum_{m=1}^{\text{M}} \sum_{n=1}^{\text{N}} [\Delta(X(m,n)) - \Delta(Y(m,n))]^2}{\sum_{m=1}^{\text{M}} \sum_{n=1}^{\text{N}} [\Delta(X(m,n))]^2}$
normalized cross correlation, $\text{NCC} = \frac{\sum_{m=1}^{\text{M}} \sum_{n=1}^{\text{N}} \text{X}(m,n)\text{Y}(m,n)}{\sum_{m=1}^{\text{M}} \sum_{n=1}^{\text{N}} \text{X}(m,n)^2}$
structural content, $\text{SC} = \frac{\sum_{m=1}^{\text{M}} \sum_{n=1}^{\text{N}} \text{X}(m,n)^2}{\sum_{m=1}^{\text{N}} \sum_{n=1}^{\text{N}} \text{Y}(m,n)^2}$
where Δ is the Laplacian operator and $\Delta((\text{X}(m,n)) = \text{X}(m+1,n) + \text{X}(m-1,n) + \text{X}(m,n+1) + \text{X}(m,n-1) - 4\text{X}(m,n)$

This is considered to be the best state of the art image quality measure. Previous approaches measure the perceptual image quality assuming that image intensity is the key component of the visual quality. This method often measures intensity error and then penalizes these errors according to their visibility. The main idea here is that human visual perception is built to understand a scene based on its structure suggesting that this structural information is the key component of visual quality.

The SSIM index is computed locally by comparing local patterns of pixel intensities that have been normalized for luminance and contrast. It is estimated as the combination of *luminance*, *contrast* and *structural content* within a local window which moves across the entire image. Suppose x and y are the local regions of the reference (X) and degraded (Y) images, then μ_x (μ_y) and σ_x^2 (σ_y^2)) are the mean and variance of the original (distorted) image. The luminance comparison is a function of mean intensity values and is defined as

$$l(x,y) = \frac{2\mu_x\mu_y + C_1}{\mu_x^2 + \mu_y^2 + C_1} \tag{2.3}$$

The contrast comparison is a function of standard deviations as given by

$$c(x,y) = \frac{2\sigma_x\sigma_y + C_2}{\sigma_x^2 + \sigma_y^2 + C_2} \tag{2.4}$$

where C_1 and C_2 are small constants which are added to avoid the instability when the denominators are very close to zero. These two values are further determined by two user defined values K_1, K_2, and the dynamic range L of the pixel values. They are computed as $C_1 = (K_1L)^2$ and $C_2 = (K_2L)^2$ where K_1 and K_2 are $\ll 1$.

The structural comparison is a function of correlation between the images and computed as

$$s(x,y) = \frac{\sigma_{xy} + C_3}{\sigma_x\sigma_y + C_3} \tag{2.5}$$

where C_3=$C_2/2$. The three comparisons of (2.3), (2.4) and (2.5) are combined to form the similarity measure as

$$\text{SSIM}(x,y) = [l(x,y)]^\alpha \cdot [c(x,y)]^\beta \cdot [s(x,y)]^\gamma \tag{2.6}$$

where $\alpha > 0$, $\beta > 0$ and $\gamma > 0$ are the parameters used to adjust the relative importance of the components. By substituting the three components and setting α=β=γ=1, the simplified expression for the local SSIM index can be estimated as,

$$\text{SSIM}(x,y) = \frac{(2\mu_x\mu_y + C_1)(2\sigma_{xy} + C_2)}{(\mu_x^2 + \mu_y^2 + C_1)(\sigma_x^2 + \sigma_y^2 + C_2)} \tag{2.7}$$

The local SSIM index values give a SSIM map showing the local error variation. These values

are then averaged to obtain a single mean SSIM index value. It has been shown that the SSIM index can better quantify the perceived image distortion than the traditional MSE or PSNR [45].

The subjective scores and various objective measures discussed, are originally developed for assessing the quality of TV and multimedia images. These conventional image quality measures are also used for quality evaluation of different medical images [44,78] and retinal images [65,79]. But they are not addressed with respect to the clinical quality of the reconstructed images.

2.2 Wavelet based image quality measures

The wavelets used in the image analysis are functions that possess certain mathematical properties. They decompose the data into different scales or resolutions. Such MRA or *multiscale approximation* (MSA) gives the possibility of investigating a particular problem at various space-frequency scales. The multiscale concept is motivated by the HVS that recognizes the images and simultaneously processes them at multiple scales [76]. The MRA technique can provide a coarse to fine and scale invariant decomposition for interpreting the image information. At different scales, the details of an image characterize the different sizes of the scene : the lower resolution provides a global view of an image, while the higher resolutions provide details of the image. The detailed study of wavelets and wavelet transforms can be found in many books and literature [48, 70, 80, 81].

The design method of the most of the DWTs is through the use of MRA. In MRA, a scaling function $\phi(x)$ is used to create a series of approximations $\phi_{j,k}(x)$ of a function by dilation and translation. Similarly, a wavelet family $\psi_{j,k}(x)$ is the set of functions generated by dilation and translation of an elementary mother wavelet $\psi(x)$. These basic scaling and wavelet functions can also be extended to two dimensions. In 2-D DWT, an image is decomposed into one low frequency approximation (A) subband and three high frequency detail subbands at each resolution as shown in Figure 2.1. The high frequency band which contains detail information in the horizontal direction is denoted as H band, the vertical detail band as V and the diagonal

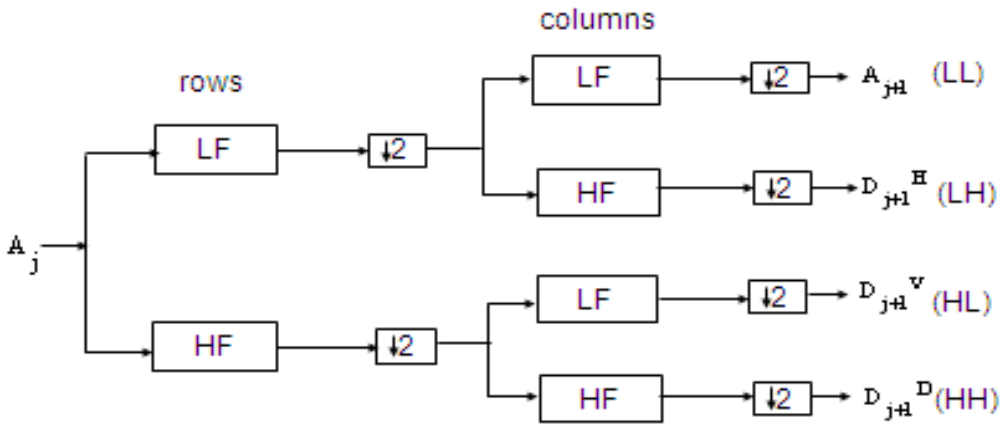

Figure 2.1: Single-level 2-D subband decomposition of the image

detail band as D. Now the basic scaling and wavelet functions are given by

$$\phi_{j,m,n}(x,y) = 2^{j/2}\ \phi(2^j x - m, 2^j y - n) \tag{2.8}$$

and

$$\psi^b_{j,m,n}(x,y) = 2^{j/2}\ \psi^b(2^j x - m, 2^j y - n) \tag{2.9}$$

at a resolution level j, $b = \{H, V, D\}$ and for all m, $n \in \mathbf{Z}$. Here (m,n) determines the position of translated scaling or wavelet function [82, 83]. The DWT of an image $f(x,y)$ of size $(R \times C)$ is then

$$W_\phi(j_0,m,n) = \frac{1}{\sqrt{RC}} \sum_{x=0}^{R-1} \sum_{y=0}^{C-1} f(x,y)\phi_{j_0,m,n}(x,y) \tag{2.10}$$

$$W^b_\psi(j,m,n) = \frac{1}{\sqrt{RC}} \sum_{x=0}^{R-1} \sum_{y=0}^{C-1} f(x,y)\psi^b_{j,m,n}(x,y) \tag{2.11}$$

where j_0 is an arbitrary starting level. The $W_\phi(j_0,m,n)$ coefficients define an approximation of $f(x,y)$ at scale j_0 and $W^b_\psi(j,m,n)$ coefficients represent the H, V and D for scales $j \geq j_0$. Given the W_ϕ and W^b_ψ, $f(x,y)$ can be obtained by the inverse DWT (IDWT) as

$$\begin{aligned} f(x,y) = \tfrac{1}{\sqrt{RC}} \textstyle\sum_m \sum_n W_\phi(j_0,m,n)\phi_{j_0,m,n}(x,y) \\ + \tfrac{1}{\sqrt{RC}} \textstyle\sum_{b=H,V,D} \sum_{j \geq j_0} \sum_m \sum_n W^b_\psi(j,m,n)\psi^b_{j,m,n}(x,y) \end{aligned} \tag{2.12}$$

Using the space frequency model of the DWT, various image quality measures have been proposed in the literature [46, 47, 84–87].

- *The Multi-Scale Structural SIMilarity* (MS-SSIM) [84]

  This measure is an extension of the SSIM [45]. This offers more flexibility in incorporating the variations of viewing conditions. The algorithm calculates multiple SSIM values at multiple image scales (resolutions). A lowpass filter is applied iteratively on reference and distorted images. The filtered images are then downsampled by a factor of 2 at the end of each filtering. This results in a series of versions of reference and the distorted images at different scales. Considering the original scale as Scale 1, and the highest scale as Scale J, the luminance comparison is computed only at Scale J and is denoted as l_J(x, y). The MS-SSIM also depends on the contrast components c_j(x, y) and structure components s_j(x, y) at each resolution. The overall MS-SSIM is evaluated by combining the measurement at each scale using

$$\text{MS-SSIM}(x,y) = [l_J(x,y)]^{\alpha_J} \cdot \prod_{j=1}^{J} [c_j(x,y)]^{\beta_j} [s_j(x,y)]^{\gamma_j} \tag{2.13}$$

  where the exponents α_J, β_j and γ_j are are used to adjust the relative importance of different components.

- The *Visual Signal-to-Noise Ratio* (VSNR) [85]

  This is a wavelet domain image quality metric for quantifying the visual fidelity of distorted images based on near-threshold and suprathreshold distortions. The distortions e between original image X and its distorted version Y are given by e = Y-X. The VSNR metric tries to improve the HVS model by incorporating the low-level and mid-level properties of the HVS. The computation of VSNR involves two stages. In the first stage, a threshold for the distortion of the degraded images is set using the wavelet based visual masking models. The distorted image is assumed to be perfect (VSNR=∞) if distortions are below the threshold. In the second stage, where the distortions are above the threshold, the low level visual property of perceived contrast and the mid level visual

property of global precedence are used. These properties are used to determine Euclidean distances in distortion-contrast space of multiscale wavelet decomposition. The RMS contrast of distortions $C(e)$ is then calculated as a linear combination of these distances. Similarly, the RMS contrast of the original image X is represented by $C(\mathrm{X})$. Then the visual signal-to-noise ratio is given by the contrast signal-to-noise ratio of X to e as,

$$\mathrm{VSNR} = 20\log_{10}\left(\frac{C(\mathrm{X})}{C(\mathrm{e})}\right) \tag{2.14}$$

A higher VSNR indicates that the tested image is less degraded.

The information theoretic approaches [46, 47] try to find alternative methods to imitate the HVS. These approaches quantify the loss of image information due to the distortion process and explore the relationship between image information and visual quality. In these methods, the distorted and reference images are considered to be two random samples. Then, the mutual information is computed as the distance between the distributions of the images.

- The *Information Fidelity Criterion* (IFC) [47]

  This measure quantifies the statistical information that is shared between the original and the distorted images. The IFC considers the mutual information between the wavelet subband coefficients of the original image and wavelet subband coefficients of distorted image. Then visual quality is evaluated as

$$\mathrm{IFC} = \sum\nolimits_{b\in subbands} I(\overrightarrow{X}^{K_b,b}; \overrightarrow{Y}^{K_b,b} | s^{K_b,b}) \tag{2.15}$$

  where $\overrightarrow{X}^{K_b,b}$ ($\overrightarrow{Y}^{K_b,b}$) denotes K_b coefficients in the b^{th} subband of the reference image (distorted image) and $\boldsymbol{s}^{K_b,b}$ is the model parameters of the subband b for the associated source image. Theoretically the IFC value ranges from zero (no fidelity) to infinity (perfect fidelity).

- The *Visual Information Fidelity* (VIF) [46]

  The measure represents the information that could ideally be extracted by the brain

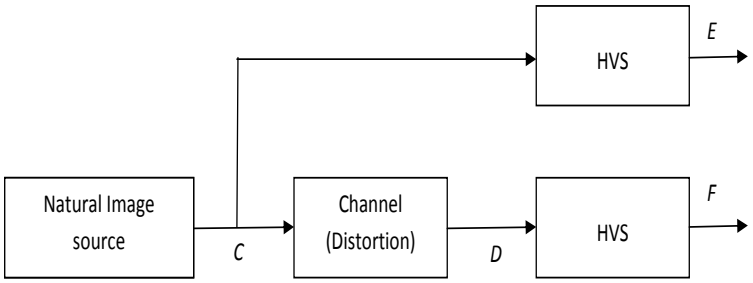

Figure 2.2: Mutual information between the reference image C and the images E and F, where these images denote visual signal at the output of the HVS model from the reference and the distorted images.

from a particular wavelet subband in the reference and the test (distorted) images. The reference image is modeled as the output of a stochastic natural source that passes through the HVS channel and is processed later by the brain. This is shown pictorially in Figure 2.2. It evaluates the quality as a ratio of mutual information between quantities in the wavelet domain. The VIF criterion uses two facts of image information to define the perceptual quality. The first is, the mutual information which quantifies how much of the reference information can be extracted from the distorted image F. The second fact is the mutual information between the HVS model of reference (original) image E and the original image itself. Combining these two quantities, a visual information fidelity measure is proposed for image quality assessment as

$$\text{VIF} = \frac{\sum_{j \in subbands} I(\overrightarrow{C}^{N,j}; \overrightarrow{F}^{N,j} | s^{N,j})}{\sum_{j \in subbands} I(\overrightarrow{C}^{N,j}; \overrightarrow{E}^{N,j} | s^{N,j})} \tag{2.16}$$

where $\overrightarrow{C}^{K,b}$ represents K coefficients from subband b of the reference image. The VIF values lie between 0 and 1. When the VIF takes a value zero, it indicates that all information about the reference image has been lost in the distortion channel. In case the image is not distorted at all and VIF is calculated between the reference image and its copy, VIF is exactly unity.

- *Wavelt based Image Quality Measure* (WIQM) [86]

The quality measure is defined using the Watson′s model of noise visibility in different wavelet subbands . The Watsons wavelet model is used to incorporate the HVS characteristics in the image quality measure. The original and the distorted images are decomposed to three levels (n=1 to N=3) using CDF9/7 filter. The orientation (θ) of the approximation band is taken as 1. For the detail bands it is 2, 3 and 4. The difference between the original and distorted images in different wavelet subbands is computed. Then each subband error value is weighted with experimentally determined weights. The WIQM is defined as the perceptually weighted difference between coefficients of original and degraded image. It is given by

$$\text{WIQM} = \sum_{n=1}^{N=3} \sum_{\theta=2}^{4} w_{n,\theta} E_{n,\theta} \tag{2.17}$$

where $w_{n,\theta}$ are the weighting factors in the related subbands and E is the error between coefficients of the original and the degraded images. The authors claim that best results are obtained by neglecting the highest frequency (level-1) subband errors and approximation subband error. The limitation of this measure is, for different image database the weights were calculated differently.

- The *Wavelet Based Normalized Mean Squared Error* (WNMSE) [87]

  It is a new image quality metric proposed in the wavelet domain. The wavelet decomposition of the original and the distorted images results in different wavelet (detail) subbands (H,V,D) and one approximation subband (A). Then the normalized mean square errors (NMSE) of the wavelet coefficients of original and distorted image is computed as,

$$\text{NMSE}_{(b,n)} = \frac{\sum_{k=1}^{K} (d_{(b,n)}(k) - \tilde{d}_{(b,n)}(k))^2}{\sum_{k=1}^{K} (d_{(b,n)}(k))^2}, \tag{2.18}$$

  where $\text{NMSE}_{(b,n)}$ is the NMSE of a wavelet subband b having K number of coefficients and at decomposition level n. The $d_{(b,n)}(k)$ is the wavelet coefficient of the original image and $\tilde{d}_{(b,n)}(k)$ is the wavelet coefficient of the processed image. Then the quality of an image is assessed as a weighted sum of normalized mean square errors (WNMSE) of the

wavelet coefficients in all the subbands.

$$\text{WNMSE} = w_{(A,N)} \times \text{NMSE}_{(A,N)} + \sum_{j\in(H,V,D)}\sum_{n=1}^{N} w_{(b,n)} \times \text{NMSE}_{(b,n)} \tag{2.19}$$

The weight w for a subband is computed using the frequency index of that subband. The frequency index $f_{(b,n)}$ of a subband b at decomposition level n is defined as

$$f_{(b,n)} = NL_{(b,n)} - NH_{(b,n)} \tag{2.20}$$

where $NL_{(b,n)}$ ($NH_{(b,n)}$) is the number of lowpass (highpass) filters that the subband passed through (Refer Figure 2.1).

The wavelet based image quality assessment schemes have been proposed based on the idea to exploit the characteristics of the HVS. But these works are aimed at evaluating the visual quality of a multimedia image.

2.3 Quality measures for retinal image

Image quality assessment plays a significant role in medical image processing applications. However, little attention has been paid towards the evaluation of the image quality from the point of view of distortion in clinically significant features [88, 89]. The ophthalmologists use the retinal images for disease detection and diagnosis. Hence, these images are required to meet the image quality criterion [73]. The quality assessment of retinal images has more constraints than the traditional image quality evaluation methods presented in the previous sections. The quality assessment has to be performed to simulate the opinion of medical experts. There are a limited number of works that have been published and devoted to address the issue of retinal image quality assessment [57–61, 90].

- *Image content based quality measures*

  The quality evaluation could be performed by an objective method based on the numerical analysis of the image content. The research on retinal image quality assessment started with histogram based methods [57, 58]. The approach in [57] is based on the idea

that *histogram similarity* is correlated with image quality. An ideal intensity histogram template is generated from 20 excellent quality retinal images. The template histogram is adjusted in order to approximate a Gaussian distribution. The width or spread of the histogram is interpreted as a measure of contrast in the image. The target image quality is assessed by computing the correlation of its histogram with the template histogram. A quality index Q, normalized between 0 and 1 is obtained and used to define the quality of the given image. A higher value of Q indicates an image of excellent quality and lower Q represents a poor quality image. Here the image quality is evaluated from the signal processing point of view considering the correlation between quality and noise. The computed Q was also used as a quality measure for image enhancement applications. It was shown that the suitability and effectiveness of image enhancement methods can be verified with the help of Q. The authors claim that this image quality measure can help retinal experts for making reliable and accurate diagnosis.

The subsequent literature [58] showed that the relation between intensity histogram similarity and image quality is not that strong. The analysis of about 40 retinal images of varying quality showed that some good quality images had histograms different from the template histogram whereas the histogram of some poor quality images matched the template histogram. Hence the authors tried to modify the quality assessment by using two different set of features: the distribution of the edge magnitudes in the image (global edge histogram) and the local distribution of the pixel intensity (local histogram), as compared to the global histogram of [57]. The authors had observed that in good quality retinal images, the shape of the edges magnitude histogram is similar to a Rayleigh distribution with a smooth fall as the intensity increases. For poor quality images, they found that edges distribution fall more rapidly than good quality images. The reference edge histogram was constructed with the edge maps of a set of good images taken from a dataset of 40 images. The edge intensity histograms were introduced to characterize the sharpness of the image. The difference between the edge magnitude histogram of a test image T and a reference edge magnitude histogram R is evaluated using a metric d_{edge}

similar to the χ^2 statistic:

$$d_{edge}(T,R) = \sum_i \frac{(R_i - T_i)^2}{R_i + T_i}, \qquad \forall i | R_i + T_i \neq 0 \tag{2.21}$$

But in their later research, the authors found that the distribution of gray scale values also plays an important role. They considered the intensity distribution of the image as another feature in the quality assessment. The mean intensity histogram is defined from a set of good quality images as in [57]. But instead of making a global similarity measure between the intensity distribution of the whole target image and an ideal distribution model, the authors used a region-based approach. The local similarity measure is computed as the difference between intensity histogram for each segmented region of the reference and the test image. Weighted sum of the local similarity measure gives the total similarity measure of the target image histogram with respect to the reference image histogram. Using these two features the authors classified the images into good, fair and bad. A shortcoming of these two methods is that they use only a limited type of analysis. Their comparison relies on one mean histogram that does not generalize well on the natural variability of fundus images.

- *Blood vessel visibility based quality measures*

  The quality assessment in [59] considers features unique to retinal images. The authors found a correlation between image blurring and visibility of the vessels. The blood vessel segmentation procedure is applied on the retinal image and the area of the detected vessels is computed. The image quality is estimated using the total vessel area. The authors were able to estimate if the image is good enough to be used for screening applications. The classification of images was possible because if the image is out of focus or blurred then the thin vessels are not visible any more. A threshold value is used to classify the images into good or poor quality images. The authors employed a dataset of 1746 images taken from a retinopathy screening program. They obtained a success rate of 84.3 % in correctly identifying good quality images and 95.0 % for poor quality images. But the limitation of the method is: even if some vessels are not detected and the main thick

vessels with significant area may mislead the retinal image quality assessment algorithm. The reason is that a considerable quantity of vessels area is taken by the two arcades which are likely to be detected even in a poor quality image. Hence a global measure of the vessel area is not enough to discriminate the good images from the bad quality images.

The authors of [60] tried to give solution to the problems with the quality assessment of [59]. They defined the image quality using two aspects: *image clarity* and *field definition*. The image clarity factor considers the visibility of the macular vessels as an indicator of image clarity. The vessels in the macular area are known to be narrow and become less visible with any image degradation. Depending on the visibility of the small vessels within one optic disc diameter (DD) around the macula, the images are graded as follows:

- *Excellent*: Small vessels are sharp and clearly visible
- *Good*: Small vessels are clearly visible but not sharp
- *Fair*: Small vessels are not clearly visible
- *Inadequate*: No vessels are clearly visible

An image with adequate field was defined as one that shows the full 45° field of view (FOV). This requires the complete optic disc, the macula and the upper and lower vessel arches. The field definition factor for defining image quality is as follows:

- *Excellent*: The entire macula and optic disc are visible. The macula is present at the center of the image and both the vessel arches are visible
- *Good*: The complete macula and optic disc are visible. The macula is not centered but both main vessel arcades are completely visible
- *Inadequate*: Either a small-pupil artifact is present, or at least one out of the macula, optic disc, upper vessel arch, or lower vessel arch is incomplete

In the above quality descriptions, the search for the macula region was restricted to a circular region at the center of the semiellipse fitted to the vessel arcades. The search

space for the optic disc was restricted to a region surrounding the rightmost or leftmost point of the macula centered images. The visibility of the macular vessels is considered as a good indicator of image clarity, because these have a width and color similar to those of microaneurysms (MAs). The final classification of the overall quality is obtained by combining the two measures of image clarity and field definition. The authors reported a success rate of 99.1 % in identifying the good quality images on a dataset of 1039 images. The authors have extended the concept to assess the clarity of retinal images obtained in mass medical screening. They have used the regionally based structural and statistical measures to define the clarity of the retinal images [90].

The methods [59,60] have been used to assess the quality of retinal images in diabetic retinopathy screening. They require a difficult step of segmenting the vessels and other major anatomical structures to find the region of interest around the fovea. The segmentation may not be accurate in case of low quality images. Another drawback is the computational cost because it requires two different transforms to find the area of interest.

- *Image structure based quality measures*

  The retinal image quality assessment system proposed by [61] is based on the assumption that an image of sufficient quality should contain particular image structures according to a certain pre-defined distribution. This is a supervised method that learns which image structures are present in normal quality images and their relative ratios. For training and testing the system, a large set of example images is used. The method does not require any specific analysis and could be applied to other types of medical images as well.

  The method employs two sets of features to represent image quality: color and second order *image structure invariants* (ISI). The color information is extracted from normalized histograms of the R, G and B color planes. The ISI features are used for *image structure clustering* (ISC). The ISC is used to represent most of the important structures found in a set of normal quality images. The authors applied filterbank to generate features invariant to rotation, position or scale. The invariance property is important because the

blood vessel structure, one of the important image structures in retinal images can have different orientations and can be found anywhere in the image. The Gaussian derivative filters up to second order are used to determine the image derivatives as L_x, L_y, L_{xx}, L_{xy} and L_{yy}. To cover the scale range of normal image structures found in retinal images, the filter outputs are found at five different scales, i.e σ= 1,2,4,8,16. For each pixel in the image, a feature vector or response vector of length $5 \times 5 = 25$ is computed. A subset of response vectors which best represent the structures in the retinal image is considered. All vectors were scaled to zero mean and unit variance and the k-means clustering was applied. The number of clusters c giving the best classification performance was found by experimentation on the training dataset of 1000 images obtained from a screening program. The features used in the final system consist of a histogram of the ISC clustered pixels as well as the raw R, G, and B histograms. A statistical classifier is trained using these two feature vectors to distinguish the normal images from low quality images. This quality assessment process is called image structure clustering (ISC). This technique does not require localizing major anatomical structures and proved to be a reliable quality estimator.

The new attempt for a fast and robust quality metric for retinal images is described in [62]. The approach is partially inspired by the work of [61]. It is assumed that the ability of a blood vessel segmentation algorithm directly depends on the overall quality of an image. But a considerable amount of vessels area is occupied by the two main thick vessels which can be detected even in a poor quality image. Hence a global measure of the vessel area (density) is not enough to discriminate the good one from bad quality images. To overcome these difficulties the authors measured the local vessel densities for different regions in the image. The RGB colour histogram with 5 bins per channel also used as a feature for image classification. The proposed quality metric algorithm operates in four stages: mask localization, vessel segmentation, feature extraction and classification. The green channel image is extracted from color fundus image and scaled down to 160x120 to reduce the computational load. The seed points are placed on the four

corners of the image. A region growing technique is initiated from these points. When the four regions are segmented, a mask is generated to show which pixels correspond to the retinal (foreground) area. The process is completed by scaling back the image to its original size. The retinal vasculature is detected using the mathematical morphology method presented in [20]. In the feature extraction process, the local vessel densities are extracted employing polar windows. The area of the vasculature under each local window is computed and this gives the local vessel density. Each local density feature is normalized to zero mean, unit variance and stored in the feature vector. A complete feature vector set is formed by adding color histogram features to the local vessel density features. These features are fed as input to the classifier. The output of the classifier shows whether the image belongs to the good, fair or the poor class of image quality or it is an outlier (not a retinal image). The authors employed a dataset of 84 macula centered retinal images with different resolutions and FOV.

- *Quality measure based on the image structures and characteristics*

  The recent method for retinal image quality assessment is published in [63]. The authors present a method that introduces a combination of global and local structural characteristics as a non-reference approach and does not involve segmentation. According to the authors, the methods discussed previously concentrate either on the histogram information, that misses the structural information of relevant image components or segmentation of structures which may be error-prone. The authors appreciate the idea of ISC method [61] but also mention the limitation as, it mainly uses the local gradient information. Compared to the state of the art, this new technique evaluates the image quality according to the four criteria. These quality criteria are inspired by diagnosis procedures based on the advice of an eye expert. Evaluating an image according to these criteria makes quality assessment a more objective task and enables the building of an objective gold standard.

  The four criteria considered above were composed of two structural and two generic criteria. The two structural criteria were based on the OD structure and the vessel structure.

It was investigated whether the OD and fine blood vessels can be recognized in the retinal images. The two generic criteria were based on homogeneous illumination and bright, high-contrast background. The retinal images were examined for uniform illumination in all parts of the image and for brightness and sufficient contrast in the background. The structural criteria are covered by an unsupervised clustering and a sharpness metric. Like in ISC, the clustering groups the anatomical structures into clusters. The clustering describes the recognizability, dissimilarity and contrast of relevant structures. In the generic criteria, which include texture, homogeneity and contrast are described by Haralick texture metrics. The authors used the combination of global clustering with local sharpness and texture features for classification. They claim that this form of quality assessment is not present in the state of the art quality assessment methods. The images considered for the quality evaluation are the optic disc centered fundus images. The images are of 1600×1212 in size with a 22.5° field of view. The method was evaluated on a test data set of 301 retinal fundus images. Three human observers preclassified the images. Then the method was evaluated based on this gold standard and compared with the ISC approach. The success rates in classification showed that this new method outperformed the state of the art ISC approach. But the anatomical components like the fovea are not considered in the process.

All the methods discussed above perform automated and objective measurement of the image quality of single retinal fundus photo.

Literature on retinal image compression

Retinal screening is an effective way to identify patients suffering from retinal diseases. Digital images of the retina are captured and then assessed by an ophthalmologist. The digital retinal images obtained during screening should possess sufficient quality for reliable diagnosis. In order to identify small features such as exudates and microaneurysms, retinal images are captured at high resolutions. This in turn means large file sizes. At least four images are taken for each patient. In this way a large number of retinal images are obtained, thus generate a huge amount

of clinical data. These images may have to be stored for future reference or to be transmitted for remote diagnosis.

The archival of thousands of images places a high demand on the storage space as well as the bandwidth when used in a Picture Archiving and Communications System (PACS) or telemedicine [89]. Therefore, image compression is a necessary step in such applications. The compression methods may be lossless or lossy. The reconstructed image after lossless compression may look like the original image when they are displayed. The lossy compression leads to loss of image information and the reconstructed image may have some changes as compared to the original image. Some studies [64, 65, 67, 68, 90] have shown that the compression up to about 20:1 does not significantly affect the diagnosis of retinal images (considering the original size of 1.3 MB). The clinical usefulness of a medical image is highly dependent on its quality. Hence evaluating the quality of processed retinal images is an important issue. The available literature on retinal image compression includes [64–69, 79, 91] for various clinical applications.

The study made in [91] found that the transmission of digital retinal images through telephone systems is difficult due to large size of the images. The authors applied image compression algorithm to color retinal photographs of 15 subjects, at five different compression rates. The compressed images were presented to an experienced observer to screen for various retinal disorders. The retinal images were compressed to about 3 % of their original size. At higher compression rates the observer could not identify the abnormal features in the retina. It is suggested that the reduced bit rate makes it practical to transmit a large number of images from remote communities. This reduced rate has implications for telemedicine. But the quality of the compressed retinal images are not quantified objectively.

The JPEG and wavelet compression methods were used to compress 30 colour retinal images in [79]. Each of the original retinal image occupied about 1.5 MB. The images were compressed to 5 different levels. To produce an image with poor quality the highest compression was selected empirically. The RMSE of each colour channel was calculated to determine objectively the quality of the images. The objective quality of the images was also measured by determining the degree to which blood vessel branching can be seen. Subjective quality of the images was

assessed by 5 ophthalmologists who recorded their observations of the original digitized image and compressed images.

The aim of the study conducted in [64] was to investigate the effect of compression on the automatic analysis of medical images. The task considered was the automatic counting of MAs. The digital retinal images taken from three patients were compressed using the JPEG and DWT. The ground-truth of MAs in fluorescein angiogram of the retina were obtained with the help of expert's opinion using uncompressed images. The effect of compression on image quality and the number of MAs correctly detected was examined. The reported results showed that the image quality degrades with the increase in the compression ratio and affects the diagnostic accuracy of detecting correct number of MAs.

The authors of [65] have carried out a study to investigate the compression of retinal images for the application in telemedicine. The JPEG and wavelet compression techniques were applied to 11 retinal images. The effect of five levels of compression on the quality of the image is discussed. They were able to compress a 1.5 MB retinal image to 29 KB using JPEG and 22 KB using a the DWT algorithm without loosing significant diagnostic information. The RMSE is used to quantify the distortion in the compressed image.

To test whether compression degrades the clinical quality of the images, the authors of [66] have studied the influence of JPEG compression on the diagnosis of glaucoma using images obtained from 155 patients. The original slides were digitized and saved both in non-compressed TIFF format and in the compressed JPEG format. A glaucoma specialist and an observer measured the optic nerve head cup to disc ratio for all three groups: the original slides, uncompressed TIFF and compressed JPEG images. They were able to compress up to a ratio of 40 : 1 without much influence on the clinical assessment.

The effect of JPEG and JPEG2000 compression algorithms on the detection of DR lesions were compared in [67]. Forty five colour fundus photographs were obtained with a digital nonmydriatic fundus camera and saved in uncompressed TIFF format (1.26 MB). They were compressed to 118, 58, 41, and 27 KB by both algorithms. Subjective image quality was graded by clinical experts. Various statistical parameters were calculated for all lesions at all

compression ratios. The result of the experiments showed that compression till 118 and 58 KB is clinically acceptable. Images with higher compression ratio were found to be insufficient for the screening purposes.

The authors of [68] undertook a study to compare digital retinal images compressed to different levels using the JPEG compression method. The original bit-mapped (BMP) images were compressed and investigated to determine whether there was any loss of clinical detail due to compression. In this study, 330 images were analyzed for the detection of DR lesions. Four different levels of compression were used and an objective analysis was undertaken using the lesion counts. The compressed images were assessed separately and blindly and the results were compared with their original BMP images. The findings of the study are, all the lower level compressed images of size 66-107 kb, appeared similar to the original BMP (1.3 Mb) images. The images with higher level compression resulted in images of size between 16 and 24 kb, were found unsuitable for diabetic retinopathy screening. The images with moderate compression had lower number of lesions compared to the original images.

In [69],the authors have analyzed the effects various levels of JPEG compression on the automatic and manual diagnosis of DR. Eighty retinal images were acquired at high quality and then compressed to various quality levels. An automated microaneurysm detector was run on these low quality retinal images. The presence of DR was decided based on the number of detected MAs. The presence of MAs was also evaluated and counted by human observers. They found that the blocking artifacts created by the JPEG format start to seriously affect the quality and hence diagnosis even at relatively low compression factors. The authors conclude that this may have important clinical implications for deciding on acceptable levels of compression for a fully automated eye-screening programme.

In the compression related literature, the problem of how the degradation of image quality with compression affects clinical usefulness has been discussed. But the problem of quantifying the degradation or changes between the original and the processed image using a distortion measure is not addressed.

2.4 Motivation for the present work

The medical images are subjected to different processing such as compression for efficient storage and transmission [92, 93]. The clinical utility depends on the quality of the processed images. The processing should ensure minimum loss of clinically useful information for the correct and efficient assessment of medical images [44, 78, 94–96]. The traditional objective measures such as the MSE and PSNR may be used to quantify the error in the processed medical images. The advantage of these measures is that it is easy to compute and use them. But the drawback of the squared error measures is that they give equal importance to all parts of the image. A slight spatial shift of an image may cause a high numerical distortion but no perceptible distortion. Conversely, a small average distortion may result in a severe visual artifacts if all the error is concentrated in a small important region. Therefore, their predictions of the image quality often do not agree well with the human visual perception [44]. It is because of such shortcomings, some alternate measures have been searched for medical images.

The limitations of conventional objective measures can be illustrated using Figure 2.3. The figure shows four retinal images having the same value of MSE ($\simeq$ 12%). But the errors are due to distortions in different spatial locations including the diagnostic features and the nonsignificant regions. The distortion in different diagnostic features may indicate different pathological (clinical) conditions. The distortion in the dark background region is diagnostically insignificant. The high error in the dark background regions may mislead the evaluation of the retinal image. On the other hand, a lower value of the MSE does not ensure the clinically acceptable quality. Hence it is required to devise an image quality measure that takes into account the loss of clinical information.

For medical images, a distortion measure has to be defined from the diagnostic perspective. Such a measure should take proper account of the medical nature of the images [78]. Certain regions of the medical image are of higher diagnostic importance and some regions are diagnostically unimportant [97]. The distortion occurring in these regions is more important than distortions in the nonsignificant (background) regions. The image quality measure is ex-

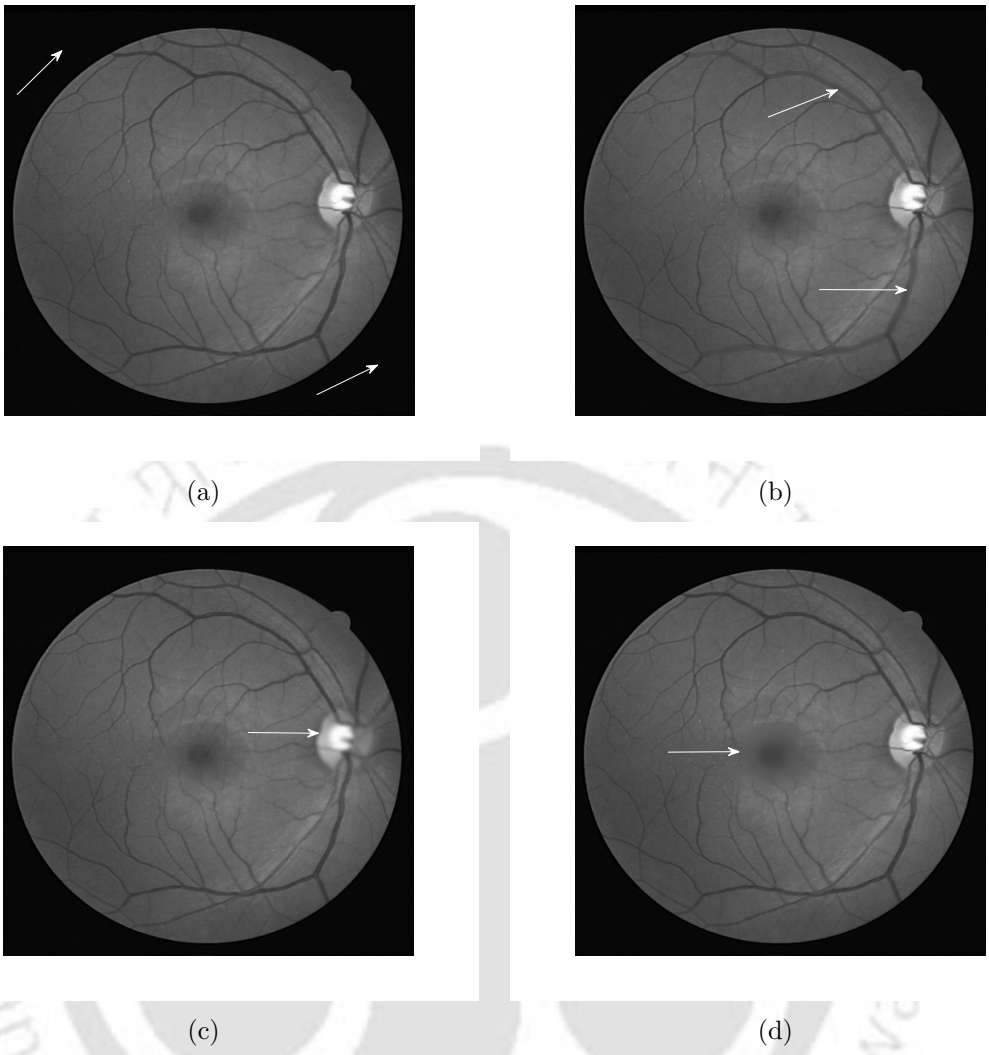

Figure 2.3: Retinal images with same MSE but having distortion in the: (a) dark background region (b) thick blood vessels (c) optic disc region and (d) macula region (shown with white arrows).

pected to emphasize the distortion in clinically important regions. Because of the differences in the characteristics of different medical images, traditional methods do not provide satisfactory results. The most common objective measure, the MSE and its related distortion measures perform the quality assessment uniformly over the whole image. These measures represent the global error characterization and they fail to capture the relevant diagnostic information loss.

To incorporate the importance of the clinically significant regions into the distortion measure, it is required to segment the image into those regions and the background. The segmentation of such regions in retinal image includes the extraction of the OD, the macula and the blood

vessels. The accurate segmentation of features in a retinal image is relatively a difficult task. In this direction, alternate methods can be investigated to localize the retinal features. The *spatial frequency localization* and *multiresolution analysis* (MRA) properties make the DWT an efficient way of image representation. The multiresolution decomposition of a retinal image separates the image features into different frequency subbands. The *multiscale* property of the wavelet shows that the features which are difficult to detect at one scale may be detected at another scale. Hence the DWT may be explored for localizing the retinal image components. The recent compression techniques for medical images such as JPEG2000 and DICOM use the DWT. The wavelet based thresholding is effective for image denoising. These attractive features of wavelet analysis has motivated us to develop a wavelet based distortion measure to quantify the loss of clinical information in retinal images.

In this thesis work, the following investigations are undertaken.

- **To study and analyze the retinal image information in wavelet subbands**

  The method uses the DWT to decompose the image into different subbands. The contribution of each subband towards the image information is different. In the present work, two methods are proposed to examine the significance of a subband from the point of view of retinal features.

  - In the first method, we introduce distortion in different subbands. The effect of distortions on the image quality is studied. This study identifies the subbands that carry significant information about a retinal feature.
  - In the second method, the information about blood vessels in different subbands is exploited to develop a novel method for segmenting the blood vessels.

- **To define a wavelet subband based distortion measure**

  The results of the investigation about clinically significant information in subbands of different decomposition levels are used

  - to propose a variable weighting scheme for the error metrics measuring the error between the original image and distorted retinal images.

The clinical information loss is quantified as a weighted sum of the errors of the coefficients in all the subbands.

  - The clinical distortion measure is computed for each of the three retinal features.
  - A global distortion measure for assessing the clinical quality of the image is defined by combining the individual distortion measures.

Any objective measure must ultimately be validated by comparing with the subjective assessments. A good objective measure should reflect the distortion in the image due to any processing like blurring, noise and compression. An objective measure is useful if it correlates well with the image quality as perceived by the viewers (human subjects). The ideal method of demonstrating this involves performing a subjective study by a number of viewers on the retinal images of different quality.

- **To evaluate the performance of the distortion measure**

  The performance of the proposed distortion measure in predicting the quality of the retinal images is evaluated. The statistical measures used for the evaluation are, the *Pearson linear correlation coefficient* (PLCC), the *Spearman rank order correlation coefficient* (SROCC), the *outlier ratio* (OR) and the *root mean squared error* (RMSE) between the subjective scores and the predicted subjective scores after nonlinear regression. The statistical behavior is also evaluated in terms of how the measure is discriminating the artifacts when tested on a variety of images using the *analysis of variance* (ANOVA) method.

Database

In the present work, retinal images are taken from test and training images of DRIVE (Digital Retinal Images for Vessel Extraction) database [98]. The DRIVE database comprises 40 eye-fundus color images. The seven of these images present pathological cases. The images are pictured with a Canon CR5 nonmydriatic 3CCD camera with a 45 field-of-view (FOV). Each image was captured at 768 $\times$ 584 pixels, 8 bits per color plane and, in spite of being offered

in LZW (Lempel-Ziv-Welch) compressed TIFF (Tagged Image File Format) format, they were originally saved in JPEG format. The database is divided into two sets: a test set and a training set, each of them containing 20 images. The test set provides the corresponding FOV masks for the images, which are circular (approximated diameter of 540 pixels). Two manual segmentations are generated by two different specialists for each image. The selection of the first specialist is accepted as the ground truth (GT) and used for algorithm performance evaluation in literature. The training set also includes the FOV masks for the images and a set of manual segmentations made by the first specialist.

The input images used in all the experiments and tests are monochrome and obtained by extracting the green channel from original RGB retinal images. The green channel provides the best vessel-background contrast of the RGB-representation. The red channel is the brightest color channel and has low contrast. The blue channel image has a poor dynamic range. Thus blood vessels in the retinal layer are best represented and reach higher contrast in the green channel [99].

3

Analysis of retinal image information in wavelet subbands

Contents

3.1 Wavelet filter for retinal image analysis 49
3.2 Wavelet analysis of retinal features 56
3.3 Blood vessel information in wavelet subbands 59
3.4 Optic disc information in different wavelet subbands 79
3.5 Macula information in different wavelet subbands 80
3.6 Summary 83

The analysis of clinical features is important for the clinical use of retinal images. In order to adequately represent these features, the proposed work utilizes the wavelet transform. The multiresolution analysis (MRA) of the wavelet helps in producing localized image features with good space frequency resolution [48, 54]. This spatial localization has proven to be useful in analyzing the local spectral properties of particular regions like the anatomical structures which are of interest in an image. The multiscale property of the wavelet shows that features which are difficult to detect at one scale may be detected at another scale. The wavelet decomposition uses a linear transformation to split an image into subbands or subimages containing different frequency information. It allows the processing of different frequency information separately. The multiresolution property of the wavelet transform has been successfully used in many applications such as image denoising, compression, data coding [51–53] and singularity detection [49]. A region based wavelet coding technique has been proposed in [100] for compression of medical images.

To emphasize the importance of this powerful tool in the analysis of retinal images, we start with wavelet decomposition of retinal image. The DWT consists of applying the low-pass and highpass filters to decompose the original image. The spectrum is divided into two equal parts resulting in the approximation band and detail band coefficients for each level of decomposition. A single level 2-D wavelet decomposition generates four subbands denoted by LL, LH, HL and HH where L represents lowpass filtering and H, highpass filtering. In the wavelet domain, the low-frequency subimage (LL) is the approximation of the original image and denoted by subband A (approximation band). The three high frequency subimages LH, HL and HH correspond to the detail information of the image such as edges and contours in different directions. These directional subbands are represented as horizontal H, vertical V and diagonal D subbands. The N-level DWT will yield 3N+1 subbands and each level contains a H band,V band and D band. The one approximation band of the final decomposition level and three detail bands of each level together form ($3N$+1) subbands as, A(N), H(N), V(N), D(N), H(N-1), V(N-1), D(N-1), ... , H(1), V(1) and D(1).

This chapter presents an investigation on retinal image information in different wavelet

subbands. Section 3.1 discusses the selection of the optimum decomposition level and the best suited wavelet filter for retinal image analysis. The information about retinal features contained in different wavelet subbands is described in Section 3.2. The distribution of blood vessel information in different subbands is described in Section 3.3. Section 3.4 investigates the important subbands that carry information of the optic disc. The clinically relevant subbands for the macula are examined in Section 3.5

3.1 Wavelet filter for retinal image analysis

Image compression is one of the most important applications of wavelets.There are two issues in using the wavelets for image processing applications. The first one is to choose the *optimum decomposition level* and the second is to select an *appropriate wavelet filter*. The next subsections deal about the experimental evaluation of the performance of various wavelet filters for retinal image compression and then to select an appropriate wavelet filter for retinal image analysis.

The choice of a suitable wavelet filter influences the image quality as well as the system design. Different mother wavelets are characterized by their regularity, which describes the smoothness of the wavelet. The performance of different wavelet filters is observed by decomposing the image into various levels using a type of wavelet filter and for a given compression ratio. The quality of the reconstructed image is evaluated at each decomposition level. Various quality measures are used to quantify the effect of wavelet filters [51, 101]. The subjective evaluation is also done by examining the visual quality of reconstructed image. The optimum decomposition level and a best suited wavelet filter for retinal image analysis can be then chosen from the experimental observations.

A few research works have been reported on wavelet based retinal image compression [64, 65, 67] using Antonini, Daubechies4 (db4) wavelet filters and JPEG 2000 compression method. However no systematic study has been done to evaluate the clinical performance of wavelet filters at various decomposition levels and at different compression rates. The intention here is to compare and contrast the behavior of a few general types of wavelet filters at various

image decomposition levels. In this study, the wavelet compression method, set partitioning in hierarchical trees (SPIHT) [102] is applied on digital retinal images. The investigation starts by selecting a wavelet filter for a given compression ratio (CR) and examining the performance at different levels of image decomposition. The decomposition procedure at a given level is illustrated in Figure 2.1 of the earlier chapter. The subband coefficients are then subjected to the SPIHT coding described below.

SPIHT algorithm

This algorithm was introduced by Said and Pearlman [102]. The SPIHT exploits the hierarchical structure of the wavelet transform by using a tree-based organization of the coefficients. It is considered as one of the advanced image coding methods. It has the advantages of high signal-to noise ratio, good quality of the decoded image, fast coding and decoding and a simple structure. The algorithm codes the most important coefficients first and then transmits the remaining coefficients so that a progressively refined copy of the original image can be obtained.

In this algorithm, the interband spatial dependencies are captured in the form of *parent-child relationship*s. Each parent node will have four children. Except the coarsest subband and the finest subbands, each wavelet coefficient (parent) at the n^{th} level of decomposition is spatially correlated to four child coefficients at the level n-1 in the form of a (2x2) block of adjacent pixels. These four child coefficients are at the same relative location in the subband decomposition structure as shown in the Figure 3.1. This relationship is utilized in the SPIHT coding. If a parent coefficient is significant (insignificant) with respect to a threshold, then all of its children would most likely be significant (insignificant). This results in coding only the parent's position information and children coordinates can be derived from the same. The SPIHT captures the significant information about coefficients and stores them in three ordered lists: *List of significant coefficients* (LSC), *List of insignificant coefficients* (LIC) and *List of insignificant sets* (LIS). These lists contain the coordinates of coefficient location. The LSC is initialized to be empty. The LIC is initialized with the coefficients of the lowest frequency approximation subband. The LIS is initialized with the detail coefficients of coarsest level.

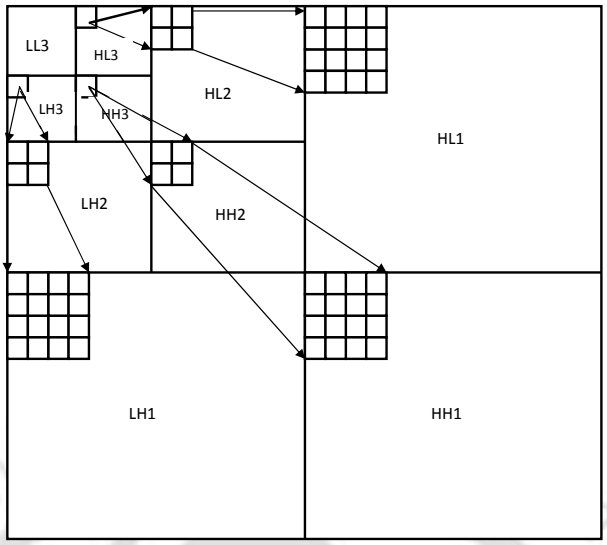

Figure 3.1: Examples of parent-child relationships in the wavelet tree.

After initialization, a threshold is chosen as $T_H(0) = 2^{n_o}$, where n_o is selected such that the largest pixel magnitude, say c satisfies $2^{n_o} \leq c < 2^{n_o+1}$.

At a given stage n, all pixels with magnitudes satisfying $T_H(n) \leq |x| < 2T_H(n)$ are identified as significant and their position and sign bit are encoded. This process is called a *sorting pass*. Then every pixel with magnitude greater than or equal to $2T_H(n)$ is refined by encoding the n^{th} most significant bit. This is called a *refinement pass*. The Figure 3.2 shows a simple block diagram of the SPIHT algorithm [103]. The encoding of significant pixel position and the scanning of pixels for refinement is efficiently accomplished using the LSC, LIC, and LIS. The encoding is progressive in pixel magnitude, using a sequence of thresholds $T_H(n) = 2^{n_o-n}$, for n= 0,1,2,....

3.1.1 Method

The various wavelet filters are applied on 20 retinal images (01_test to 10_test and 30_training to 40_training) randomly selected from test and training sets of the DRIVE database [98]. The green channel image is extracted from original color image and resized to 256 x 256. The CR

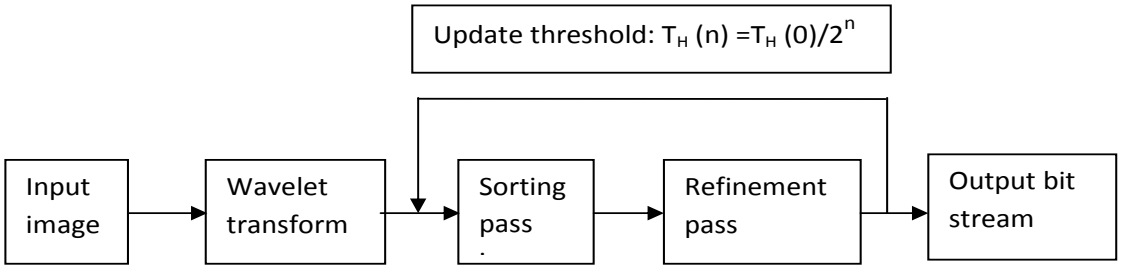

Figure 3.2: Block diagram of the SPIHT algorithm.

is varied from 2 to 10. The experimental results are obtained by decomposing an image to different levels (from 2 to 8) using a given wavelet filter for a particular CR. The experiment is repeated for different compression ratio. The quality of resulting image is investigated by numerically computed objective measures and by subjective visual image quality test. Similar observations are made for the whole set of filters. The objective measures- PSNR, LMSE and SSIM index are used to quantify the effect of wavelet compression. The subjective evaluation is quantified by the mean opinion score (MOS) [74]. The 5 level scoring with description is given in Table 2.1. The MOS values are obtained from two medical experts and six students working in different areas of signal processing. The performance evaluation is done across all images.

3.1.2 Selection of optimum decomposition level

Decomposing the image to fewer levels means better energy retention and better image quality. Decomposing to higher levels provides better compression but more energy loss and degraded image quality. The experiments in this work show that the best trade-off between energy loss, compression and image quality is provided by decomposing to a level of 5 or 6 for a 256x256 image. The results required for selecting the optimum decomposition level for a given wavelet filter for all 20 images across all compression ratios are shown in Figure 3.3. The optimum decomposition level can be determined by plotting the PSNR against decomposition levels at different compression rates as shown in Figure 3.3(a). After a particular decomposition level, the PSNR tends to saturate and that level is taken as the optimum decomposition level. Similarly Figure 3.3(b) shows the LMSE variation with decomposition levels. The LMSE decreases from

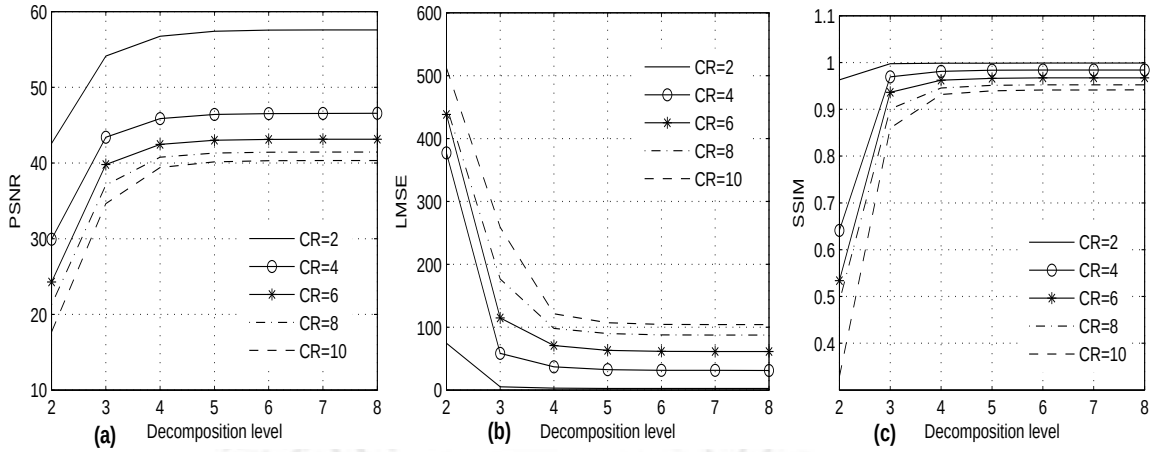

Figure 3.3: Average values of (a) PSNR, (b) LMSE and (c) SSIM at different decomposition levels for CR = 2, 4, 6, 8, 10. The Wavelet filter used is db5.

a higher value at initial decomposition levels to a much lower value at later levels up to an optimum decomposition level. Thereafter the variation in LMSE values is very little. Figure 3.3(c) gives the SSIM index values at different decomposition levels. The SSIM index value increases initially up to an optimum decomposition level and remains at the same value for further decomposition levels.

3.1.3 Selection of appropriate wavelet filter

Since large numbers of wavelet filters are available, researchers often have difficulty in selecting an optimal wavelet for a specific image processing application. The selection of the wavelet filter depends on important properties like compact support, symmetry, orthogonality, regularity and the degree of smoothness. How well a wavelet can pack the signal energy in as few coefficients as possible depends on the wavelet properties. But it is difficult for a wavelet filter to have all properties and it has to sacrifice some property to satisfy the remaining properties. This compromise makes the filters to belong to the wavelet family of orthogonal, biorthogonal or symmetric. In each family, wavelet filters of different order N_o can be chosen. Generally the decomposition filter order N_{od} and reconstruction filter order N_{or} will be of same. But biorthogonal wavelet can have similar or different filter orders for decomposition and reconstruction. The lower order filters with compact supports have good time localization and preserves high

frequency features like edges. The higher order filters lead to higher degree of smoothing because of their wider support.

In this work, five types of wavelet families such as Haar, Daubechies, Coiflet, Biorthogonal and Symmetric wavelets are considered. The following set of wavelet filters are examined : Haar wavelet, db-N_o with $N_o = 1$; Daubechies wavelet, db-N_o with $N_o = 2, 3, 5, 6, 7$; Coiflet wavelet, coif-N_o with $N_o = 1, 2, 3, 4, 5$ and Biorthogonal wavelet, bior-$N_{or}.N_{od}$ with $N_{or}, N_{od} = 2.2, 3.3, 4.4, 5.5, 6.8$ and Symmetric wavelets, sym-N_o with $N_o = 2, 4, 5, 6, 7$. An appropriate wavelet filter is chosen by considering the effect of all wavelet filters on the quality of a set of 20 images at the optimum decomposition level and at various compression ratios. The comparison results of objective quality measures- the PSNR, LMSE and SSIM indices averaged over 20 images for each wavelet filter are recorded in Table 3.1. It is noted that among all the wavelet filters considered, the wavelet filter bior6.8 performs better by having maximum PSNR, minimum LMSE and best SSIM index values at different CR as shown by the row with darker shade of gray. This shows that the objective quality of the processed image is better for the Biorthogonal wavelet family. The reason may be that, biorthogonal wavelets use linear phase filters with similar or dissimilar order for decomposition and reconstruction filters. They are more symmetrical, have a relatively short support and close to orthogonal wavelets. All these properties ensure less reconstruction error [104]. It is also possible to find the appropriate filter from a particular family of filters using the same criterion. The filter coif2 performs better among the Coiflet family of filters. Similarly, db3 and sym5 perform better compared to other filters of their respective family. These are shown by the rows of lighter gray shade.

The digital retinal images are processed using different types of wavelet filters. The perceptual effect of different wavelet filters, filter orders and decomposition levels on retinal images is examined. The comparison of the performance of the wavelet filters is done on the basis of objective quality parameters- the PSNR, the LMSE and the SSIM index . These measures help in selecting the optimum decomposition level as 5 and bior6.8 as the appropriate filter for retinal image analysis.

Table 3.1: Average Values of PSNR, LMSE and SSIM index at optimum decomposition level.

Wavelet	CR=2			CR=4			CR=6			CR=8			CR=10		
	PSNR	LMSE	SSIM	PSNR	LMSE	SSIM	PSNR	LMSE	SSIM	PSNR	LMSE	SSIM	PSNR	LMSE	SSIM
bior2.2	56.810	3.233	0.998	46.149	36.491	0.983	43.030	65.974	0.967	41.306	94.210	0.953	40.245	109.509	0.943
bior3.3	54.067	6.208	0.997	44.412	54.035	0.976	41.674	85.917	0.958	40.089	112.634	0.944	38.891	135.523	0.932
bior4.4	57.626	2.345	0.999	46.660	28.822	0.985	43.287	56.622	0.969	41.591	82.305	0.954	40.487	98.782	0.944
bior5.5	56.782	2.252	0.998	46.011	27.249	0.983	42.430	55.080	0.963	40.992	79.151	0.949	39.869	95.420	0.937
bior6.8	57.675	2.503	0.999	46.675	30.760	0.984	43.324	59.448	0.969	41.611	85.415	0.954	40.494	101.910	0.944
coif1	57.407	2.618	0.999	46.496	31.528	0.984	43.108	62.218	0.967	41.402	89.255	0.952	40.262	107.073	0.941
coif2	57.558	2.546	0.999	46.620	30.658	0.984	43.216	60.355	0.968	41.525	86.435	0.953	40.401	103.284	0.943
coif3	57.527	2.571	0.999	46.541	31.309	0.984	43.145	60.970	0.967	41.471	86.878	0.952	40.341	103.567	0.942
coif4	57.465	2.613	0.999	46.452	32.238	0.984	43.056	62.591	0.967	41.378	88.865	0.952	40.241	105.802	0.940
coif5	57.395	2.653	0.999	46.400	32.521	0.983	42.987	63.198	0.966	41.312	89.976	0.951	40.151	106.876	0.940
db1	56.067	3.569	0.998	46.199	33.543	0.982	42.738	67.729	0.964	41.015	96.059	0.947	39.723	119.450	0.935
db2	57.326	2.658	0.999	46.433	32.007	0.983	43.022	63.170	0.966	41.316	90.063	0.951	40.164	107.981	0.940
db3	57.446	2.608	0.999	46.520	31.541	0.984	43.113	61.610	0.967	41.425	88.149	0.952	40.287	105.493	0.941
db5	57.402	2.639	0.999	46.408	32.403	0.984	42.995	63.045	0.966	41.306	89.784	0.951	40.154	106.952	0.940
db6	57.355	2.680	0.999	46.315	32.953	0.983	42.903	64.145	0.966	41.223	91.636	0.950	40.059	109.074	0.938
db7	57.302	2.718	0.999	46.307	33.289	0.983	42.854	64.907	0.965	41.174	92.495	0.950	39.983	110.418	0.937
sym2	57.326	2.658	0.999	46.433	32.007	0.983	43.022	63.170	0.966	41.316	90.063	0.951	40.164	107.981	0.940
sym4	57.553	2.546	0.999	46.606	30.803	0.984	43.179	60.990	0.967	41.483	87.016	0.953	40.354	104.173	0.942
sym5	57.630	2.502	0.999	46.627	30.308	0.985	43.230	60.145	0.968	41.540	86.106	0.953	40.414	103.087	0.942
sym6	57.591	2.528	0.999	46.594	30.959	0.984	43.177	60.974	0.967	41.495	86.744	0.953	40.368	103.592	0.942
sym7	57.512	2.569	0.999	46.525	31.554	0.984	43.108	61.452	0.967	41.449	87.062	0.952	40.314	104.322	0.941

3.2 Wavelet analysis of retinal features

The wavelet decomposition of an image produces several subimages or subbands of coefficients. Each subband contains information in a specific direction and along a specific scale/frequency. The advantages of using the wavelet transform is that the signal features can be extracted in the wavelet domain [105,106]. The research works related to wavelet transform based retinal image analysis focussed on the use of processed retinal image for different applications [26,41,69,107]. But no systematic study has been made to evaluate the retinal features at various wavelet subbands.

In the present study, we propose two methods for the analysis of retinal features.

(1) In the first method, the importance of a subband in representing a retinal feature is investigated. Different subbands refer to different frequency components of an image. They have different contributions to the image quality. Distortions at different frequencies will have different impact on the image components. Hence we have introduced distortion in different subbands and its effect on the quality of the retinal image (features) is observed. These effects are quantified by computing the SSIM index. The SSIM index is used to estimate the similarity between the retinal features before and after the subband distortion.

(2) In the second method, the blood vessels information in different subbands is exploited to develop a novel method for segmenting the blood vessels. A vessel emphasized image is constructed using the relevant subbands for blood vessels. This image is subtracted from the background image. The difference image gives initial vessel image. Vessel segmentation is performed by thresholding and postprocessing the initial vessel image. The segmented vessel pattern shows that, out of many subbands only a few of the subbands have discriminating information about blood vessels.

The retinal image G can be partitioned into regions G_b and G_f such that $G{=}G_b \cup G_f$. G_b is the retinal background and G_f contains all the other anatomical features [108]. The image part G_f can be modeled as $G_f{=}G_v \cup G_d \cup G_m$ having three components: the blood vessels G_v, the optic disc G_d and the macula G_m . G_f is characterized by sharp boundaries and gray

level changes and thus contains a relatively large proportion of high frequency components. In contrast, G_b consists of slowly varying background and thus contains the low frequency components. In a retinal image, vessels have different widths or resolution. The main thick vessels branch into thin vessels and spread in all over the retina. Therefore multiresolution property of the wavelets can be used to analyze the vessel features. The directional property is another important characteristic of the vessel structure. Since the two dimensional DWT can decompose the image into different frequency bands in several directions, the vessel details in different orientations can be observed.

In this work, a five-level decomposition is performed on the retinal images of size 512×512 generating fifteen *detail subbands* and one *approximation band*. The fifteen detail subbands can be put into 5 groups according to the levels of transformation: level-1 (L1), level-2 (L2), level-3(L3), level-4 (L4) and level-5 (L5). Each of the subband contains information about the retinal image [87,109]. The detail coefficients may provide vital information about the localized features of the retinal image. The approximation coefficients represents the slowly varying low frequency background of the retinal image.

It is important to know the significance of each level subbands from the point of view of presence of diagnostic information in that subband. For a particular diagnostic feature, it is expected that certain subbands may contain information that is relatively more significant than the other subbands. The diagnostic importance of each level subbands is examined by zeroing the coefficients of the subbands and keeping all other subband coefficients unchanged. The effect is analyzed by reconstructing the image with the altered subbands. The original and the reconstructed images are visually examined to assess the image quality from the point of view of the blood vessels, the macula and the optic disc. These effects are also quantified by computing the SSIM index between the retinal features before and after the subband distortion. This shows that which of the subbands carry significant information of the features.

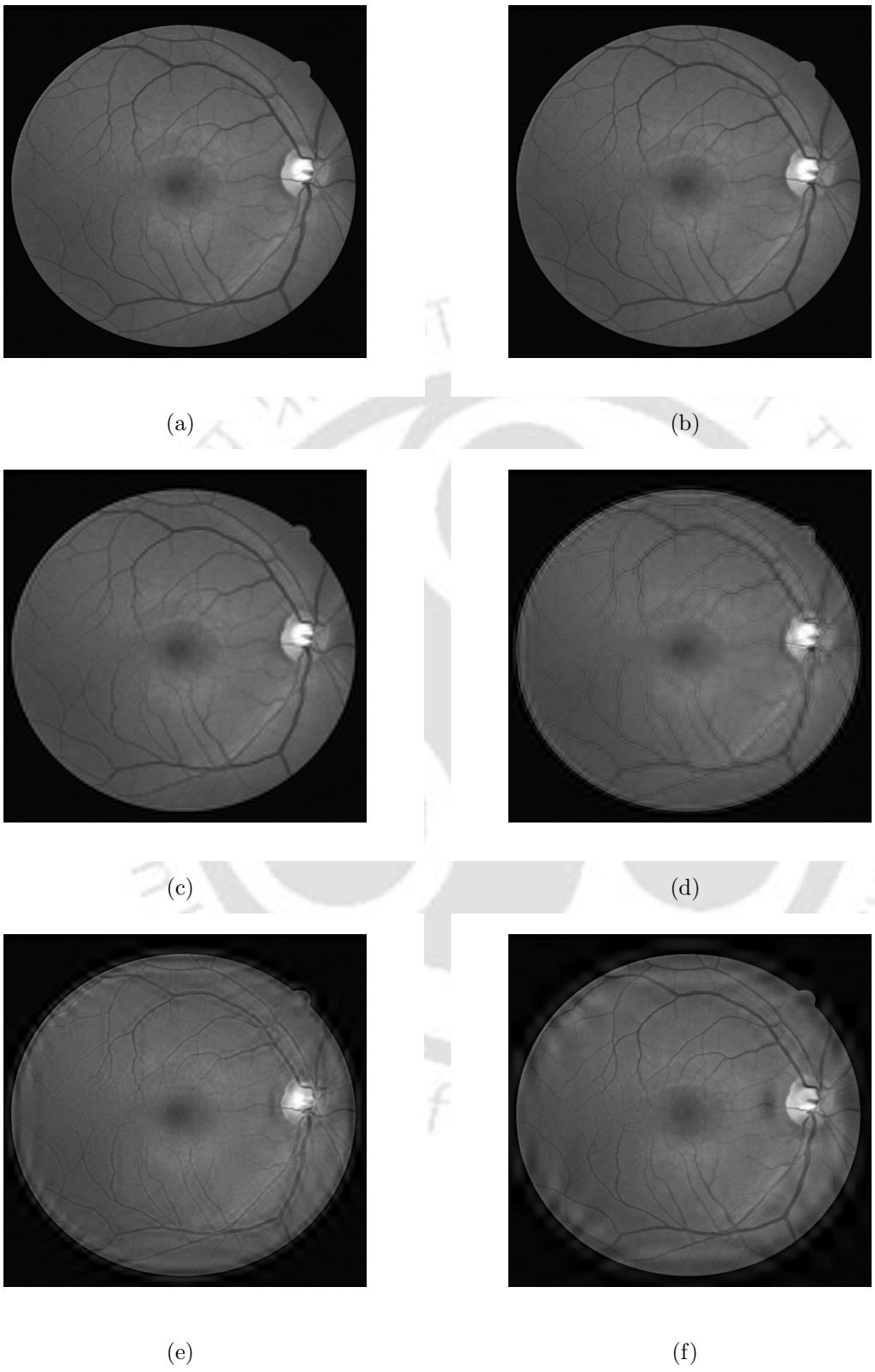

(a) (b)

(c) (d)

(e) (f)

Figure 3.4: (a) Original image and reconstructed images when subband coefficients of (b) L1, (c) L2, (d) L3, (e) L4 and (f) L5 are made zero.

3.3 Blood vessel information in wavelet subbands

In this subsection, we analyze the significance of each subband from the point of view of blood vessel information in a retinal image. The blood vessels are darker compared to the background and their thickness varies as they travel radially out of the optic disc. The vascular network is thicker in the area near the optic disk and the vessel thickness gradually reduces leading to the thin end part. The main thick vessel splits into many small thin branches and they almost get lost when their thickness is only of one pixel. The nonvessel region acts as background and is one with slowly varying pixel values. Based on the above information, the diagnostic importance of each subband is examined by zeroing the coefficients of the subband and keeping all other subbands undisturbed. The diagnostic quality of the retinal image is examined by reconstructing the image with the altered subbands.

In image processing applications, generally the low frequency approximation band A(5) is kept unaltered. The effect of approximation band coefficients is not considered [86] and only the detail subbands are considered in all the computations discussed further in this thesis.

To illustrate the importance of subbands at each decomposition level, consider the images shown in Figure 3.4. The retinal image 36_training from the DRIVE database is shown in Figure 3.4(a) and decomposed to 5 levels using the biorthogonal filter. The blood vessels represent changes in intensity and characterized by high frequency subbands. The image in Figure 3.4(b) is obtained after zeroing the highest frequency coefficients of decomposition level-1 (L1) subbands H(1), V(1) and D(1). It is observed that the vessel structure is well reconstructed and the overall image quality is close to the original image. This implies that subbands H(1), V(1) and D(1) do not carry significant blood vessel information. The image in Figure 3.4(c) is produced after zeroing the coefficients of L2 subbands H(2), V(2) and D(2). In this image the blood vessels look slightly smeared but still the details of main vessels are retained. Most of the thin vessels have lost their sharpness by spreading into the surroundings and faint end part of small branches have disappeared. It is observed that the quality of the image is not as good as that of Figure 3.4(b). Similar results are obtained when tested with other retinal images from

the DRIVE. It shows that any alteration of second level subband coefficients has more effect on the thin vessels, whereas there is a little effect on thick vessels. The thin vessels are considered to be of higher frequency components as compared to the thick vessels. Hence the L2 subbands are expected to have higher significance for thin vessels. The reconstructed image after zeroing the subband H(3), V(3) and D(3) coefficients is shown Figure 3.4(d). The image shows that the main thick vessels are smeared and most of the thin vessels are preserved. It is observed that the image quality is low as compared to that of Figure 3.4(c). This shows that thick vessels are sensitive to changes in the third level subband coefficients. A small amount of thin vessel information is affected by the third level subband coefficients. The thick vessels constitute the low frequency components of the image in relative to the thin vessels. This may be the reason for distortion in thick vessels when the third level subband coefficients are altered. So, the L3 subbands are important for thick vessels as compared to higher frequency L2 subbands. So, the L3 subbands are expected to have higher importance for thick vessels as compared to higher frequency L2 subbands. Figure 3.4(e) shows the image after zeroing the coefficients of subbands H(4), V(4), D(4) of L4. It is observed that the thin vessels are clear and has little distortion in thick vessels. When the coarsest subband H(5), V(5) and D(5) coefficients are made zero, the reconstructed image in Figure 3.4(f) shows that the vessel pattern is well preserved. The image has a thin ring like appearance along the circular periphery of the FOV. This is due to the loss of global information such as luminance and it is more visible in the areas where the gray level distribution has a sharp gradient. The diagnostic quality of the image still be retained since these artifacts do not disturb the diagnostic features. The study shows that the subbands of lower frequency (L3 and L4) hold more of thick vessel information. The higher frequency (L2) subbands carry information about fine structures such as thin vessels.

The relative importance of subbands in each decomposition level can also be investigated. Figure 3.5 shows the results when all the coefficients in one of the subbands (H(2), V(2) and D(2)) of the L2 are individually zeroed. The images in Figure 3.5(b) and (c) show a significant loss of blood vessel information in the horizontal and vertical direction when H2 and V2 subband coefficients are modified. When D2 subband coefficients are zeroed, there is no significant loss

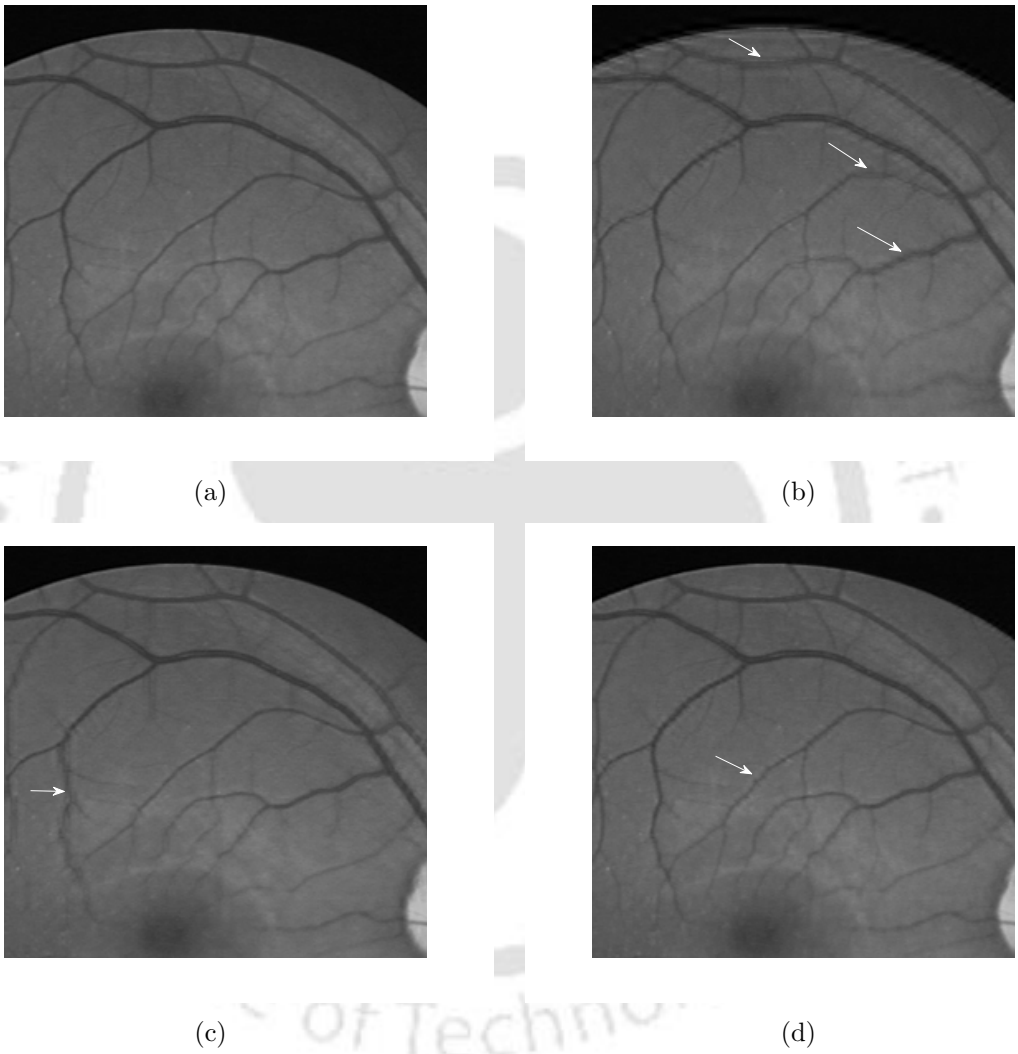

Figure 3.5: (a) Original image and reconstructed images when coefficients of subband (b) H2, (c) V2 and (d) D2 are made zero. Only small section of the image is shown for better visualization.

Table 3.2: SSIM index values for blood vessels in different directions

Zeroed band	Thick vessels in			Thin vessels in		
	Hori	Vert	Diag	Hori	Vert	Diag
V(1)=0	0.9977	0.9936	0.9975	0.9969	0.9914	0.9951
V(2)=0	0.9957	0.9762	0.9954	0.9945	0.9566	0.9827
V(3)=0	0.9974	0.9265	0.9952	0.9937	0.9680	0.9932
V(4)=0	0.9982	0.9204	0.9993	0.9968	0.9968	0.9994
V(5)=0	0.9997	0.9935	0.9993	0.9993	0.9996	0.9995

of vessel information as shown in Figure 3.5(d). The effect of zeroing the coefficients of the third level subbands H(3), V(3) and D(3) is also found to be similar.

To quantify the effect of altering the coefficients of a subband on blood vessels, a simple experiment is performed. Small sections of thick and thin vessels in approximately horizontal (Hori), vertical (Vert) and diagonal (Diag) orientations are picked from the original and the reconstructed images. The SSIM index for blood vessels is then computed and tabulated. When there is strong similarity, the SSIM index takes a value of one and it takes zero for no similarity. Table 3.2 shows SSIM index values for blood vessels when the coefficients of different subbands are made zero. Only the vertical subband coefficients from all decomposition levels are considered and their effect on blood vessels is observed. Thin vertical vessels get disturbed when the coefficients of subband V(2) are made zero. The thin vertical vessels show lower SSIM index value of 0.9566 whereas the thick vertical vessels show SSIM index reading 0.9762. This indicates that the thin vessels are significantly distorted compared to thick vessels. The third row entries show the SSIM index values when coefficients of subband V(3) are zeroed. The SSIM index value in the third column of the third row, 0.9265 indicates that the distortion of the thick vessel in the vertical direction is more significant. The thin vessels in the same direction are comparatively less disturbed as indicated by an SSIM index value of 0.9680 in the same row. These results show that the coefficients of second level subbands have more influence on thin vessel distortion. Similarly the coefficients of third level subbands have higher significance for distortion in thick vessels and little effect on thin vessels. It can be observed

from the results in Table 3.2 that the coefficients of fourth level subbands have little effect on thick vessels and the coefficients in the first and fifth level bands have minimum effect on blood vessels. Another example shown Figure 3.6 also demonstrates the clinical importance of subbands for the image 01_test from the DRIVE database.

Pathological images

The experiment is also performed using pathological images and the clinical importance of subbands is observed. The blood vessel information in different subbands is investigated for two pathological images 08_test and 31_training from the DRIVE database. The results of the experiment are shown in Figure 3.7 and Figure 3.8. From these images it is observed that subbands of L2 are important for preserving the thin vessel information. The quality of thick vessels is influenced by the coefficients of L3 and L4 subbands. The L1 and L5 subbands have less clinical importance as they do not disturb the blood vessel structure.

From the point of view of distortion in blood vessels, the different subbands behave differently. The results of visual quality investigation and SSIM index values are used to rank the clinical importance of subbands of different levels. In image processing applications, the distortion in the image is generally due to the attenuation of the high frequency components. The thin vessels are composed of higher frequency components and the distortions in them are perceived even at low compression rates. Hence the L2 subbands are expected to have higher clinical importance compared to the other subbands. With all these observations, different subbands can be ranked according the vessel information content, in the descending order as $L2, L3, L4, L5$ and $L1$.

3.3.1 Analysis of vessel information through segmentation

This section describes the segmentation of blood vessels using the vessel information provided by different wavelet subbands. The analysis of retinal images using the DWT discussed in Section 3.3, shows that the significant information about blood vessels is captured by only a few subbands while other subbands carry minimum information of the blood vessels. This observation is exploited to propose a new method for the segmentation of blood vessels.

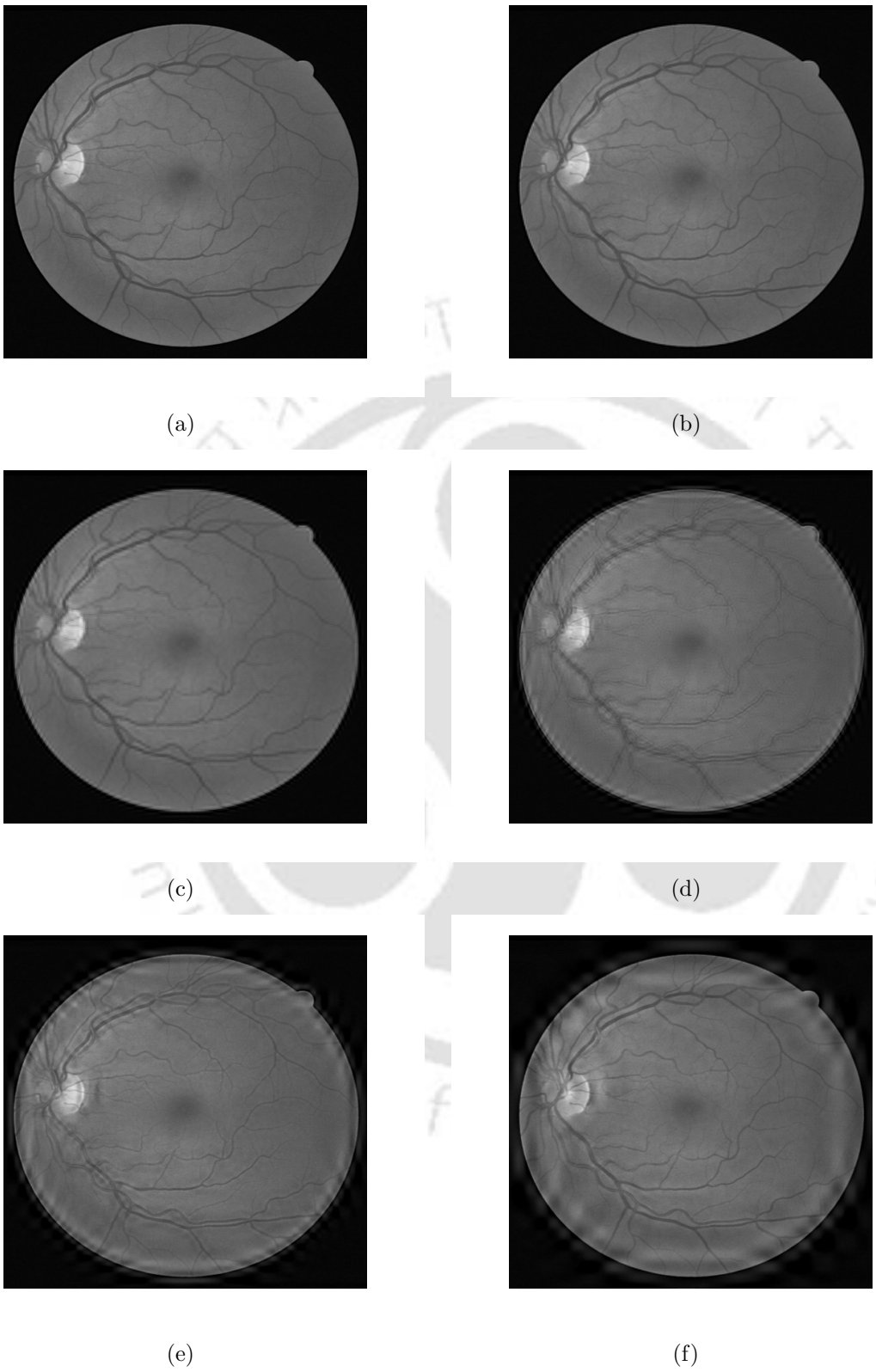

(a) (b)

(c) (d)

(e) (f)

Figure 3.6: (a) Original image and reconstructed images when subband coefficients of (b) L1, (c) L2, (d) L3, (e) L4 and (f) L5 are made zero.

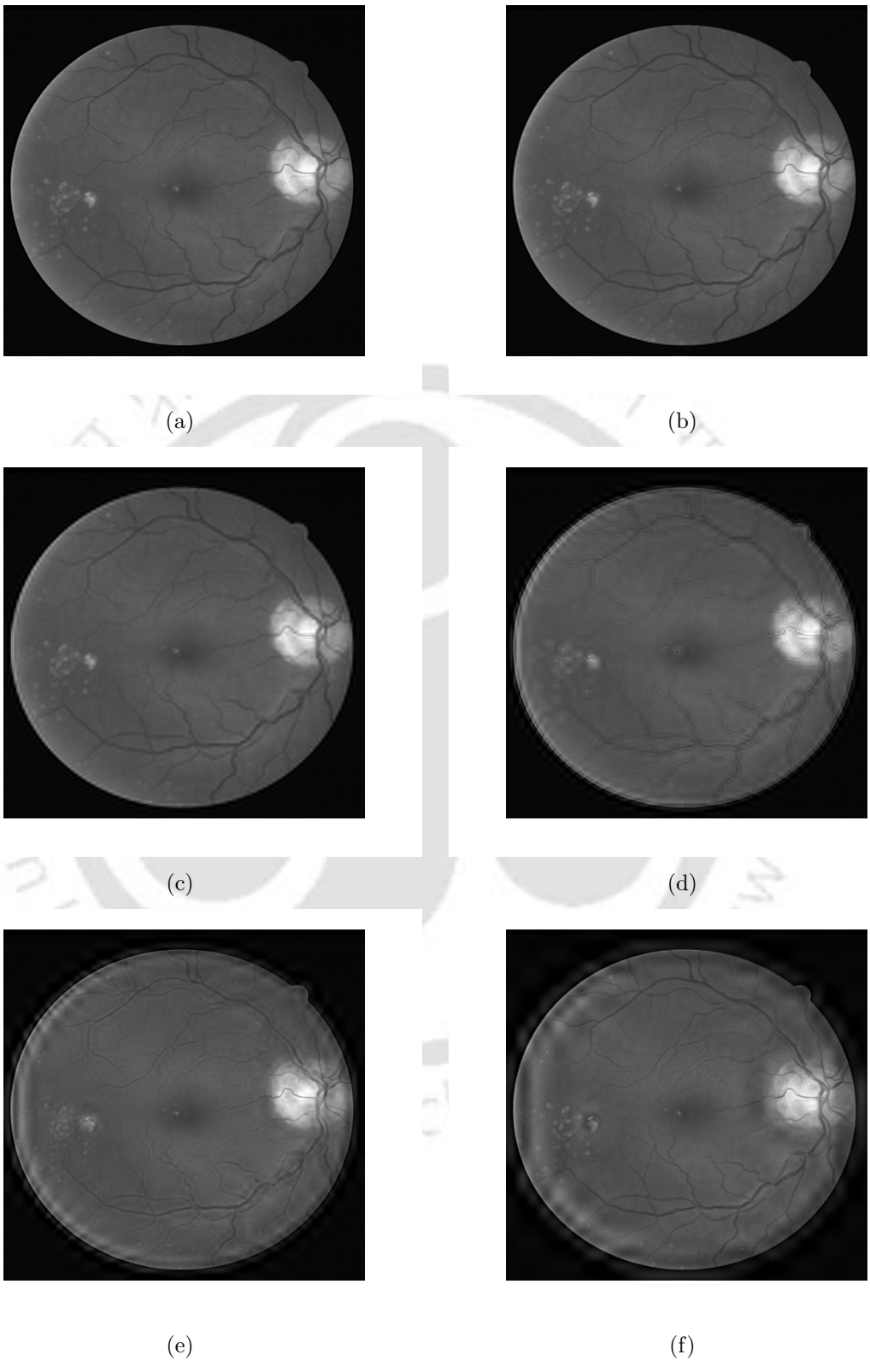

Figure 3.7: (a) Original image and reconstructed images when subband coefficients of (b) L1, (c) L2, (d) L3, (e) L4 and (f) L5 are made zero.

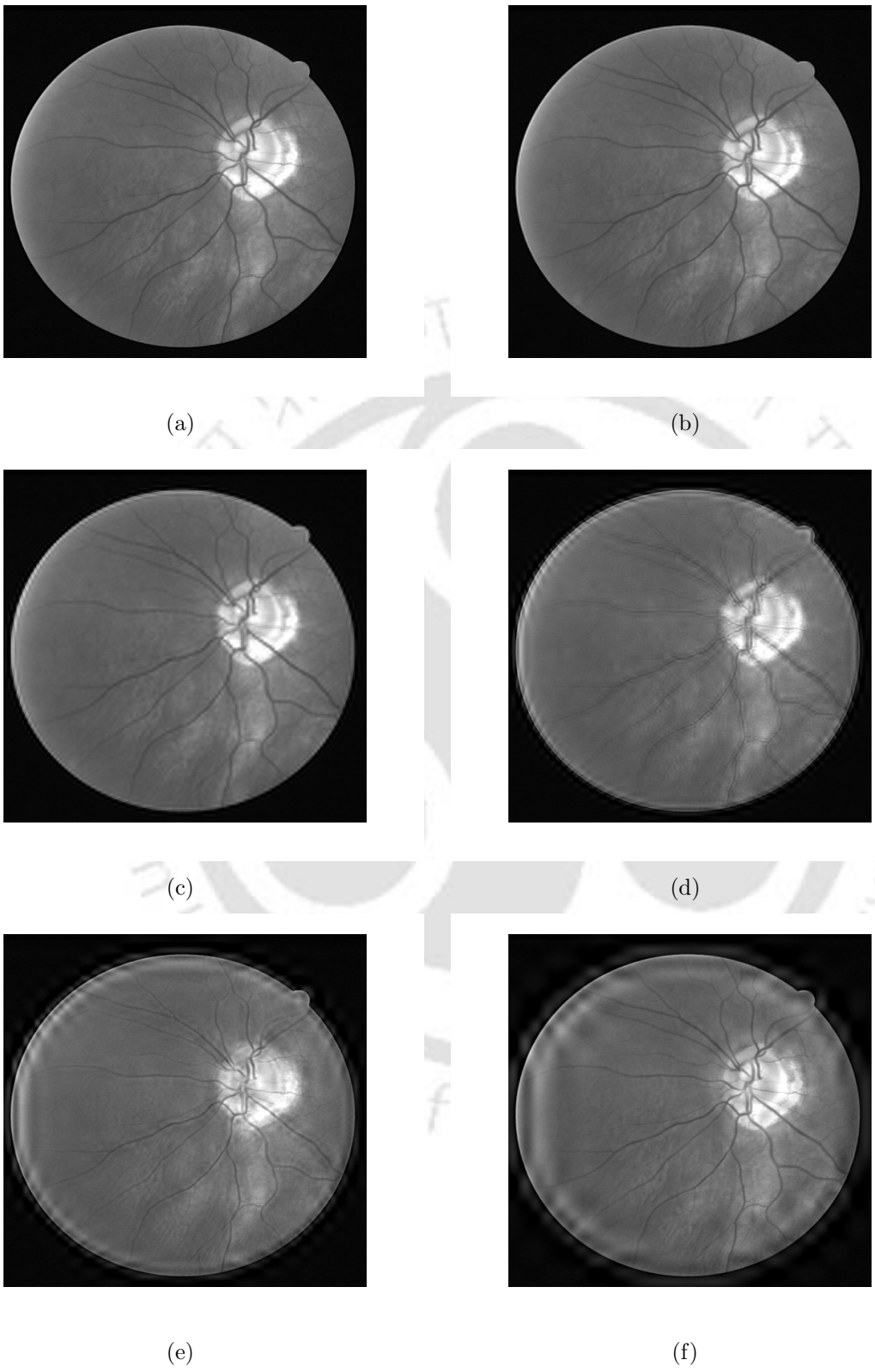

(a) (b)

(c) (d)

(e) (f)

Figure 3.8: (a) Original image and reconstructed images when subband coefficients of (b) L1, (c) L2, (d) L3, (e) L4 and (f) L5 are made zero.

Blood vessel segmentation in retinal images is a fundamental step for interpretation of the image content. In this direction we propose a method for blood vessel segmentation based on wavelet decomposition of the gray retinal images. The gray images are obtained by extracting the green channel from original RGB color images. The green channel is used because it presents the better contrast between regions belonging to the vessel network and the background. The images are then resized to 512×512 and decomposed to five levels using the bior6.8 wavelet filter. The proposed algorithm employs:

(i) preprocessing of retinal images

(ii) wavelet decomposition

(iii) creating the background image using significant wavelet subbands

(iv) subtracting the background image from the original image to get difference image or initial vessel image

(v) thresholding the initial vessel image to generate the vessel map

(vi) postprocessing of the vessel map to get segmented vessels.

The application of the preprocessing algorithm helps in enhancing the image to make it suitable for the subsequent segmentation processes. The post processing includes length filtering and morphological operations. This step helps filling gaps in the detected blood vessels and removing falsely detected isolated vessel pixels. A number of unsupervised [16, 18, 20, 23, 110] and supervised techniques [24–27] are available to deal with this special features (blood vessels) of the retinal image. The method followed in the present work is computationally simple still maintaining a reasonable level of accuracy.

Preprocessing: This process includes green channel extraction and histogram equalization for local contrast enhancement of the retinal image. The output image of this stage emphasizes the local contrast of the image so that the blood vessels are more clearly distinguished from the background.

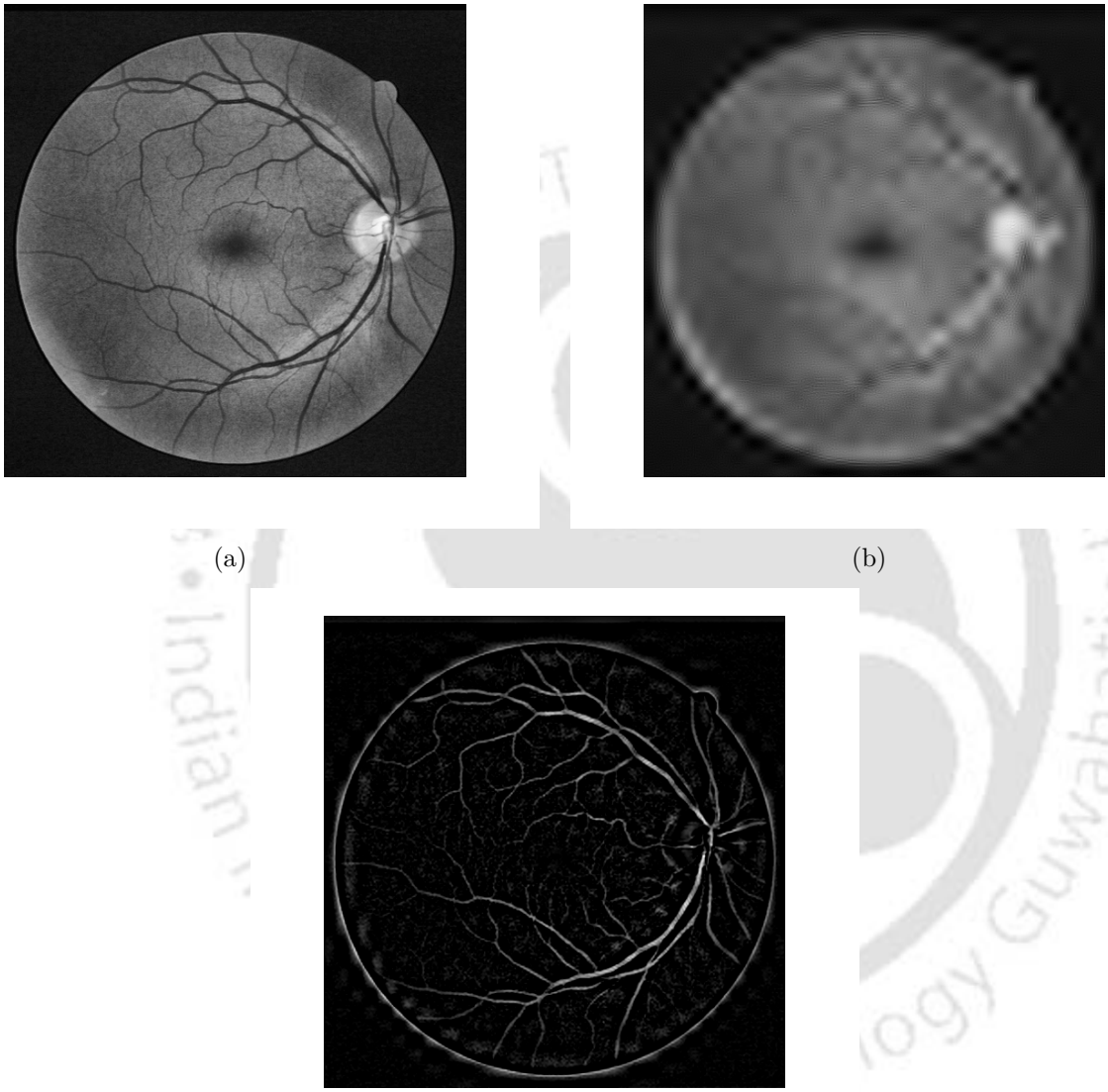

(a) (b)

(c)

Figure 3.9: (a) Original image (b) Background retinal image (c) Initial vessel image (after background subtraction and normalization).

Generating the vessel image: The retinal image can be considered as composed of two components, the blood vessels and the background. The vessel image is obtained by subtracting the background from the original image. The background image contains all the information except blood vessels. This can be estimated by making the subband coefficients of L2, L3, and L4 zero. The coefficients of low frequency approximation subband, L1 and L5 subbands are kept intact. This suppresses the blood vessel components in the retinal image leaving only the approximated background. The reconstructed image using these modified subbands gives the estimated background image as shown in Figure 3.9(b). A difference image is obtained by subtracting the background image from the original image. The difference image consists of many small valued pixels. This image is normalized by the maximum difference value. This process generates a normalized difference image having pixel values in the range [0, 1]. This helps making all the small valued pixels as background pixels. Figure 3.9(c) shows the normalized difference image. Since this difference image emphasizes the blood vessels, it can be called as initial vessel image.

Blood vessel segmentation from the initial vessel image: The next step is to extract the blood vessel map from the initial vessel image. It is observed that number of pixels that hold high confidence to belong to the background is more than the number of pixels that belong to the vessel structure. To segment the vessels from the initial vessel image, a simple threshold is applied to the normalized vessel image. The main task of thresholding is to highlight pixel values which correspond to the blood vessels and suppress small values which correspond to background in the image. The important parameter in this process is the choice of the threshold value. A simple and easy way to get this value is to use the histogram of the initial vessel image. After experimenting with forty images from the DRIVE database, it is found that nearly 80 % of the pixels in the difference image are unimportant background pixels and only 20 % of the pixels belong to the blood vessels. These values are also verified by considering the manually segmented vessel images available in the database. It is observed that the number of pixels belong to the background are more compared to the vessel pixels. After thresholding process as indicated in Figure 3.10 (b), the pixels are grouped into background and vessel pixels. The

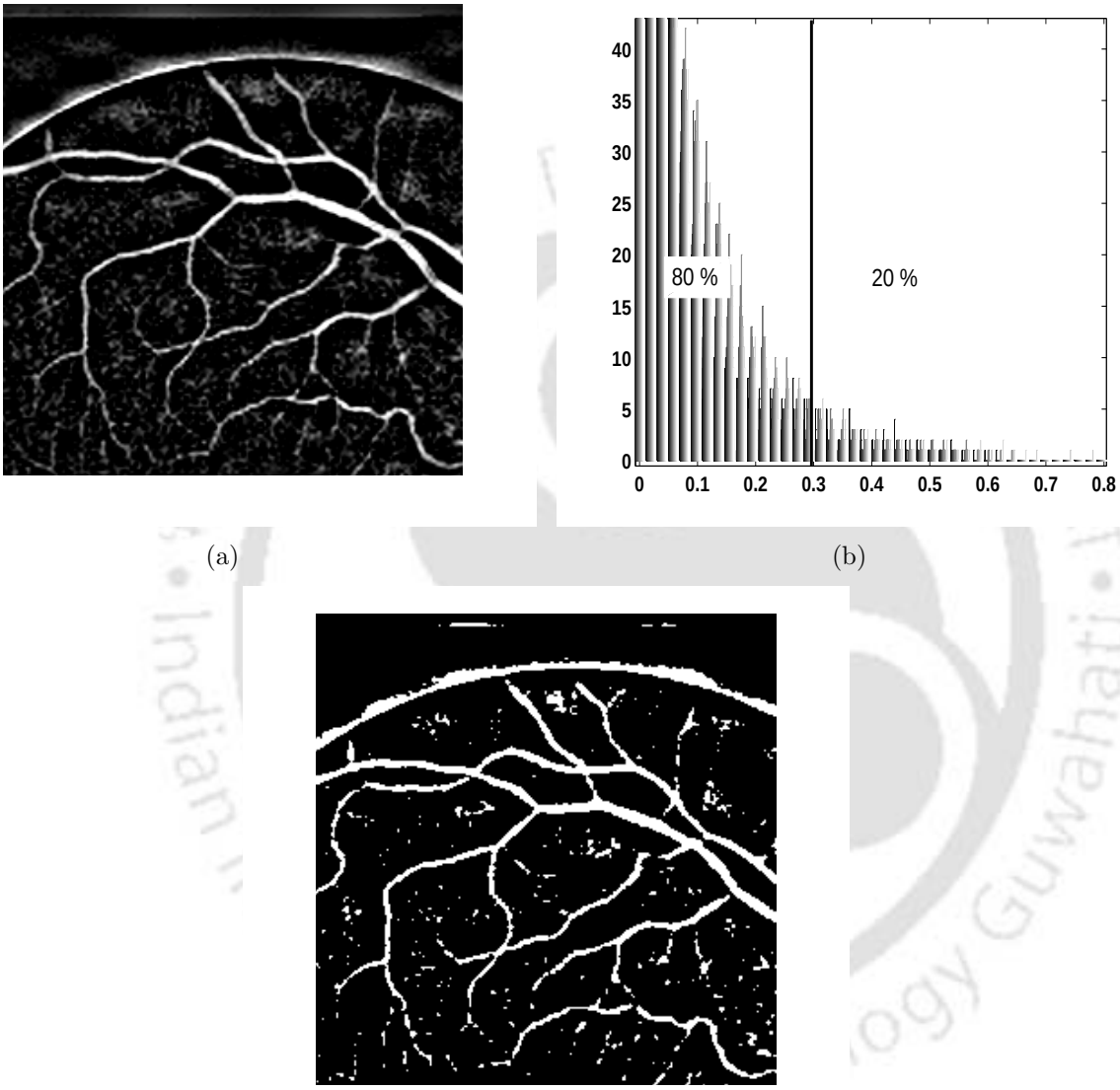

Figure 3.10: (a) Initial vessel image (b) Histogram and threshold selection and (c) Thresholded vessel image.

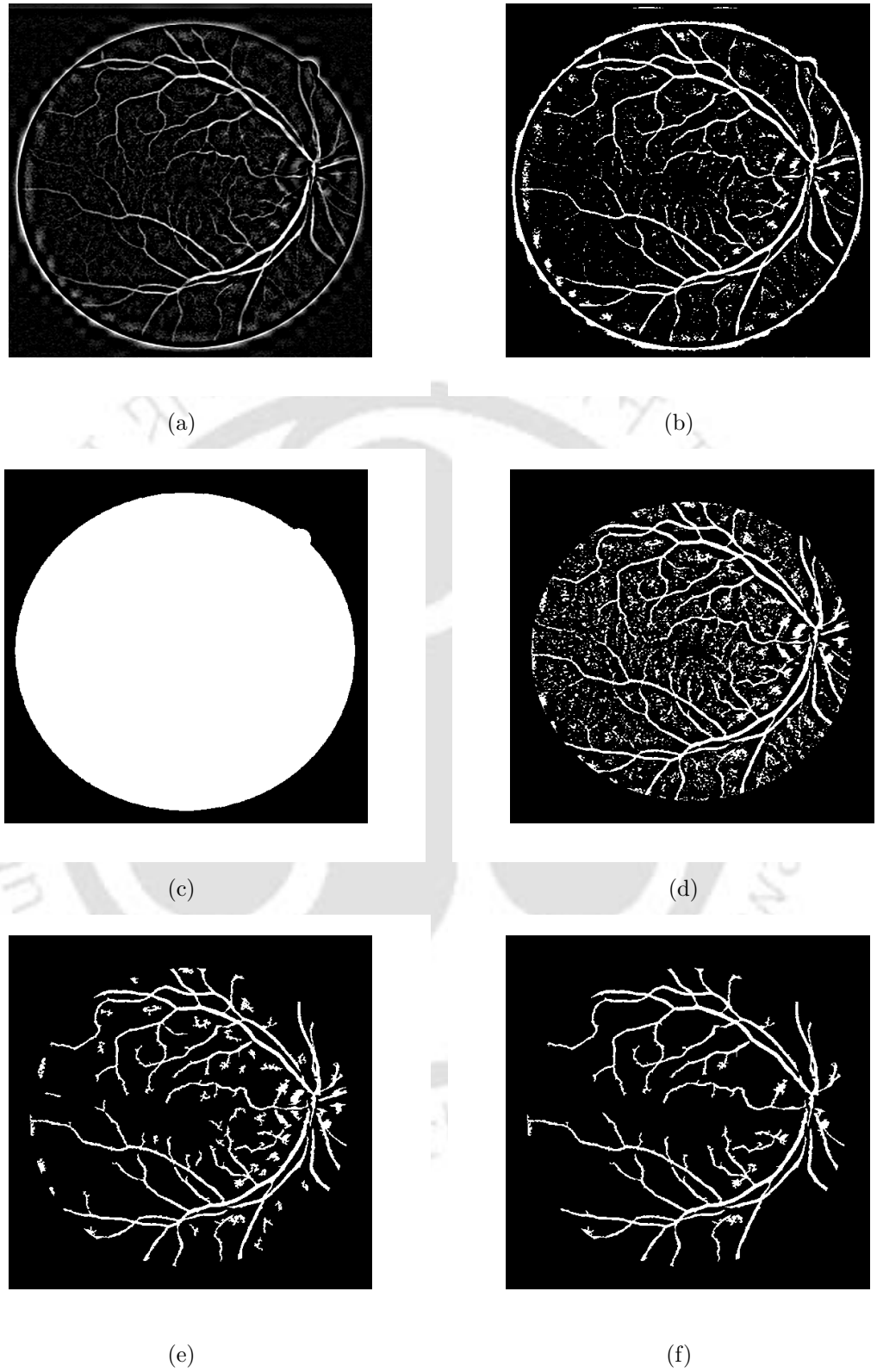

Figure 3.11: (a) Image showing initial vessel map (b) Thresholded vessel image (c) Mask image (d) Mask multiplied vessel image (e) Vessel map after length filtering and (f) Segmented vessel map after morphological processing.

result of thresholding is a binary image, shown in Figure 3.10 (c). It is observed that some noisy patterns still exist in the resultant vessel map. One way to remove the noisy patterns is to employ some postprocessing procedures.

Postprocessing:

The segmentation results can be improved through a postprocessing procedure. The post-processing methods are used to remove falsely detected vessels in the binary vessel image (Figure 3.10(c)) thereby improving the detection accuracy. This stage also includes eliminating the circular FOV edge artifacts, length filtering [111] and mathematical morphology functions [20]. Figure 3.11 shows the results of each step in the postprocessing.

The vessel image after thresholding exhibits circular edge artifacts and some artifacts outside the circular FOV region. They can be observed in Figure 3.10(c) and 3.11 (b). Therefore, a mask which indicates the circular FOV region is used to eliminate these artifacts. The mask images are available in the database for all the images. An example of the mask for the image is shown in Figure 3.11(c). The thresholded vessel image is multiplied by the mask which removes these artifacts and leaves only the segmented vessels inside the FOV. Figure 3.11(d) shows an image without edge artifacts. The segmented vessel image contains some disconnected, small groups of pixels. These isolated parts are removed by length filtering [111]. The length filter is based on the concept of connected pixels labeling. Connected regions correspond to individual objects. The length filtering tries to isolate the individual objects by using the four or eight-connected neighborhood. Every isolated part is labeled as an object. Each object is entered into a look-up-table (LUT) with its label and length information. The LUT is sorted according to the length information in descending order. We applied a threshold length value to LUT. This removes the small groups of isolated pixels from the binary image. Once the algorithm is completed, only the resulting classes exceed a certain number of pixels are labeled as blood vessels. This limit is varied to get better segmentation accuracy. The length filtered vessel image is shown in Figure 3.11(e). Finally the binary vessel image is subjected to morphological open function to remove small disconnected vessel parts present in the length filtered image. Figure 3.11(f) is the result of the postprocessing step showing the segmented blood vessels.

Table 3.3: Vessel classification table

	Vessel present	Vessel absent
Vessel detected	True positive (TP)	False positive (FP)
Vessel not detected	False negative (FN)	True negative (TN)

Following the similar procedure, an image emphasizing only the thick vessels can also be generated. The background image consisting of all the components except the thick vessels is obtained by zeroing all the coefficients of L3 and L4 subbands. Then the difference image, obtained by subtracting the background image from the original image shows more of thick vessels and further processed for thick vessel extraction. The images shown in Figure 3.12 give a visual illustration of the process. Figure 3.13 shows the vessel image emphasizing only the thin vessels, generated in the same way. The background image consisting of all the components except the thin vessels is obtained by zeroing all the coefficients of L2 subbands. Thin vessels are segmented by processing the difference image.

The proposed segmentation method is evaluated using the retinal images of the DRIVE database. The performance of proposed algorithm is quantified by comparing the segmentation result with the gold standard images available in the database. For each of the test and training data set images a corresponding manually segmented image is provided. The pixels that have been determined to be part of a blood vessel are set to one. The nonvessel or background pixels are set to zero. The manual segmentation gives a binary image and generally used as ground truth (GT) for evaluating the performance of segmentation algorithms. An example of the original and the GT of image of 10_test is shown in Figure 3.14.

To ensure that only the portion of the image containing vessels is considered during processing and analysis, a mask image is provided. This consists of a black background with a white image field indicating the location of relevant image data in a retinal photograph (Figure 3.11(c)).

The result of vessel segmentation in retinal images is a pixel classification based process. Each pixel is classified either as foreground (vessel) or backgorund (nonvessel). This leads to four possible events: true positive (TP), true negative (TN), false positive (FP) and false

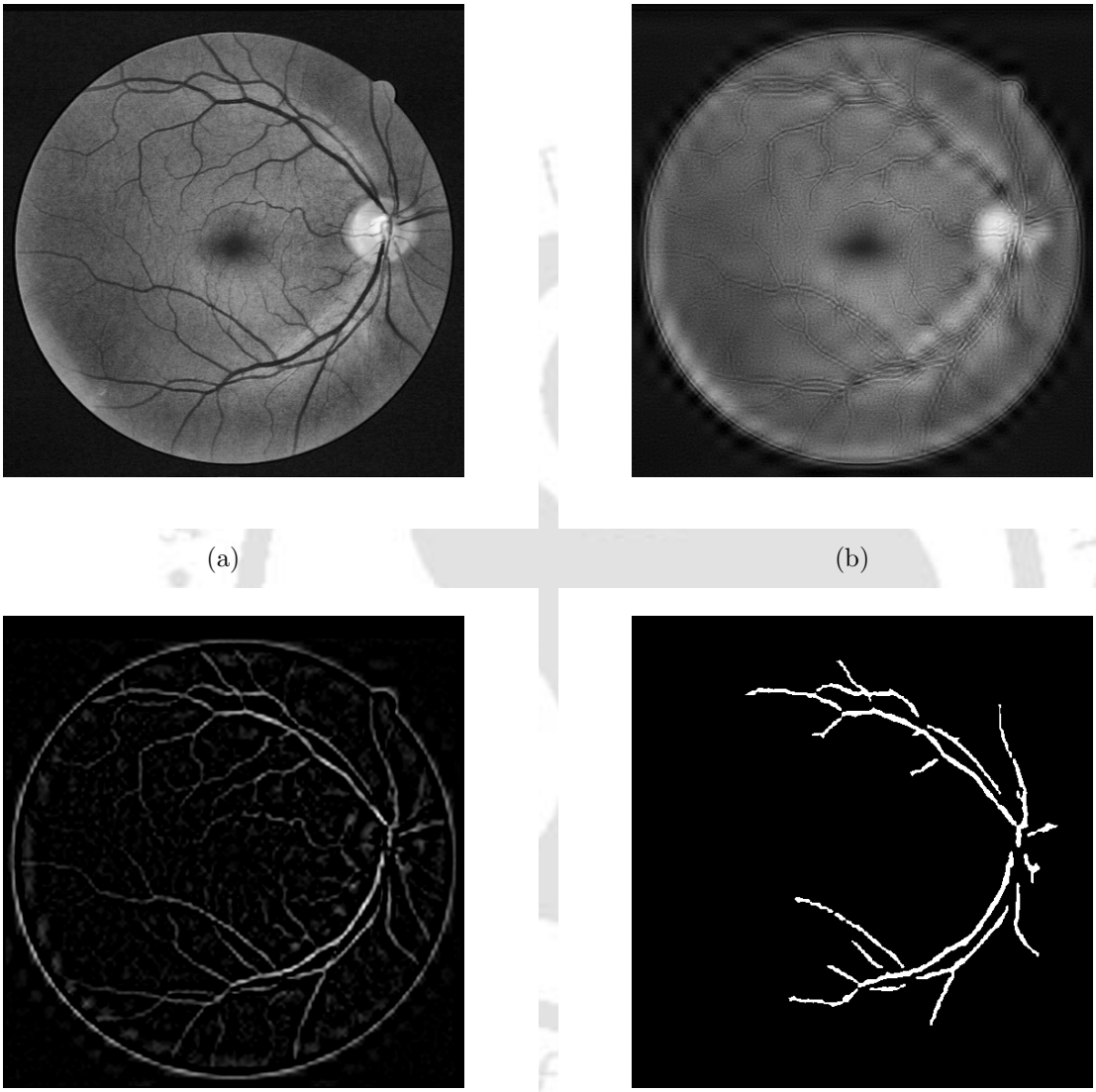

(a) (b)

(c) (d)

Figure 3.12: (a) Original image (b) Background image (c) Difference image and (d) segmented image showing the thick vessels.

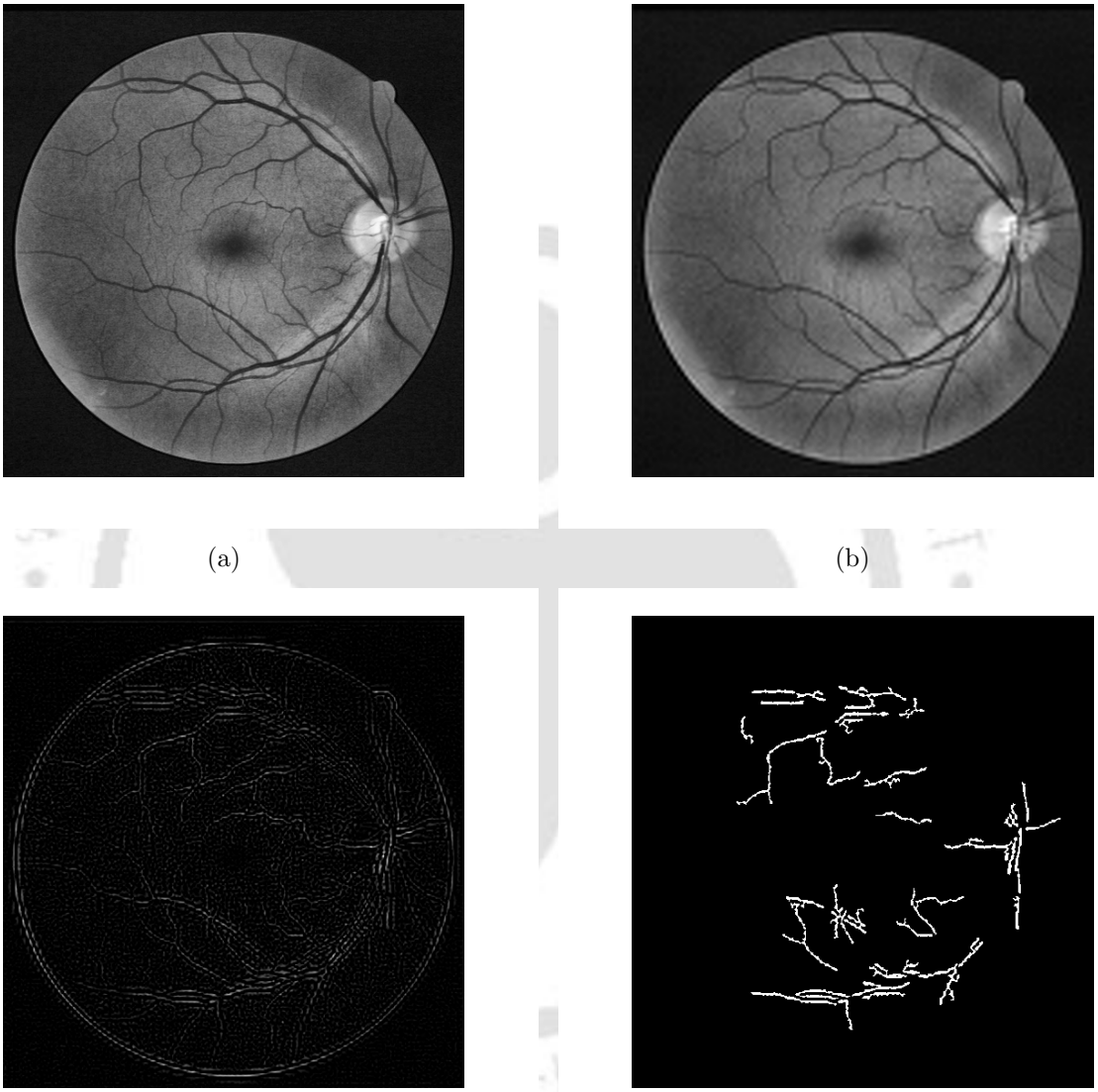

(a) (b)

(c) (d)

Figure 3.13: (a) Original image (b) Background image (c) Difference image and (d) segmented image showing the thin vessels.

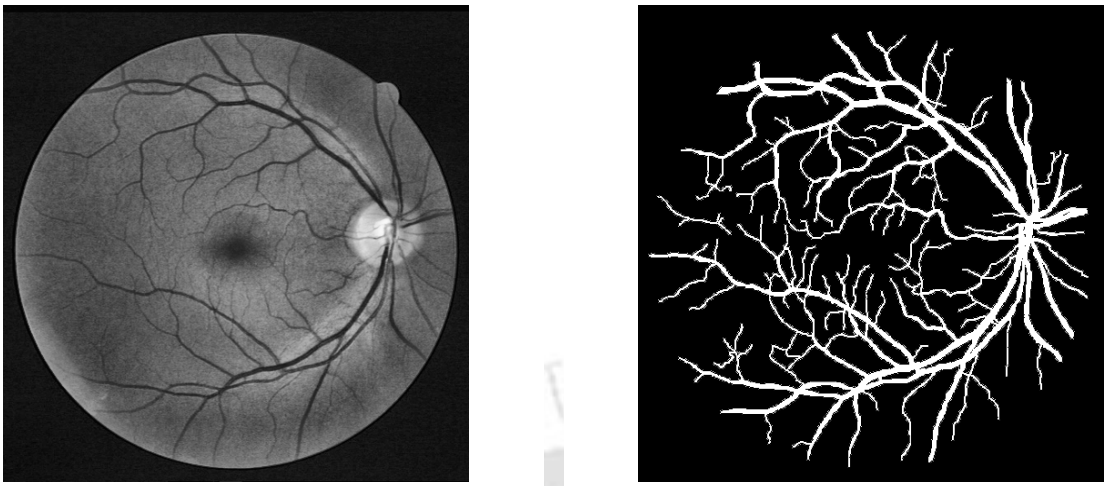

(a) (b)

Figure 3.14: (a) Original image (b) ground truth (GT) image.

negative (FN) as shown in Table 3.3. The correctly classified pixels as a vessel or nonvessel are indicated by TP and TN whereas misclassifications are indicated by FP and FN, respectively.

In the present work, the performance of the proposed vessel segmentation method is assessed in terms of sensitivity (Se), specificity (Sp) and accuracy (Acc) [27]. These metrics are defined as,

$$Se = \frac{TP}{(TP + FN)} \tag{3.1}$$

$$Sp = \frac{TN}{(TN + FP)} \tag{3.2}$$

$$Acc = \frac{TP + TN}{TP + FN + TN + FP} \tag{3.3}$$

The sensitivity is also called as true positive rate (TPR). The Se is estimated by dividing the number of true positives by the total number of vessel pixels in the GT. A related term is the false positive rate (FPR), given by

$$FPR = \frac{FP}{(TN + FP)} \tag{3.4}$$

Table 3.4: Performance results on test images of DRIVE database

Method	Se	Sp	Acc
Chaudhuri et al. [16]	0.2716	0.9795	0.8895
MF-FDOG [18]	0.7120	0.9724	0.9382
Zana and Klein [20]	0.6696	0.9769	0.9377
Martinez-Perez et al. [23]	0.7246	0.9655	0.9344
Jiang and Mojon [110]	0.6478	0.9626	0.9222
Proposed	0.6906	0.9547	0.9159

Then Sp = 1- FPR, is computed by dividing the number of true negatives by the total number of nonvessel pixels in the GT. For a perfect segmentation, values of TPR should be 1, whereas for FPR should be 0. The Acc is a global measure providing the correctly classified pixels. It shows the degree of conformity of the segmented blood vessel map with the GT. Since the dark background outside the FOV is easily detected, all the values are computed for each image considering FOV pixels only.

Comparison with other methods

A comparison of the proposed segmentation method with other segmentation algorithms is presented in Table 3.4. An outline of these algorithms was presented in Section 1.1. The *Se*, *Sp* and *Acc* values are computed for all the 20 test images of the DRIVE database. The average value of each parameter is computed and compared with that obtained by other methods. The performance results were obtained considering the threshold value as the mean threshold varying about one standard deviation (0.3 ± 0.05) for all the images in the test set. The threshold value was set in the defined range to provide maximum accuracy for each image. The experimental investigation shows encouraging results with an average sensitivity of 0.6906, average specificity of 0.9547 and average accuracy of 0.9159 on images from the DRIVE database. The proposed method is simple and achieves promising vessel segmentation results as compared to the state-of-the-art schemes.

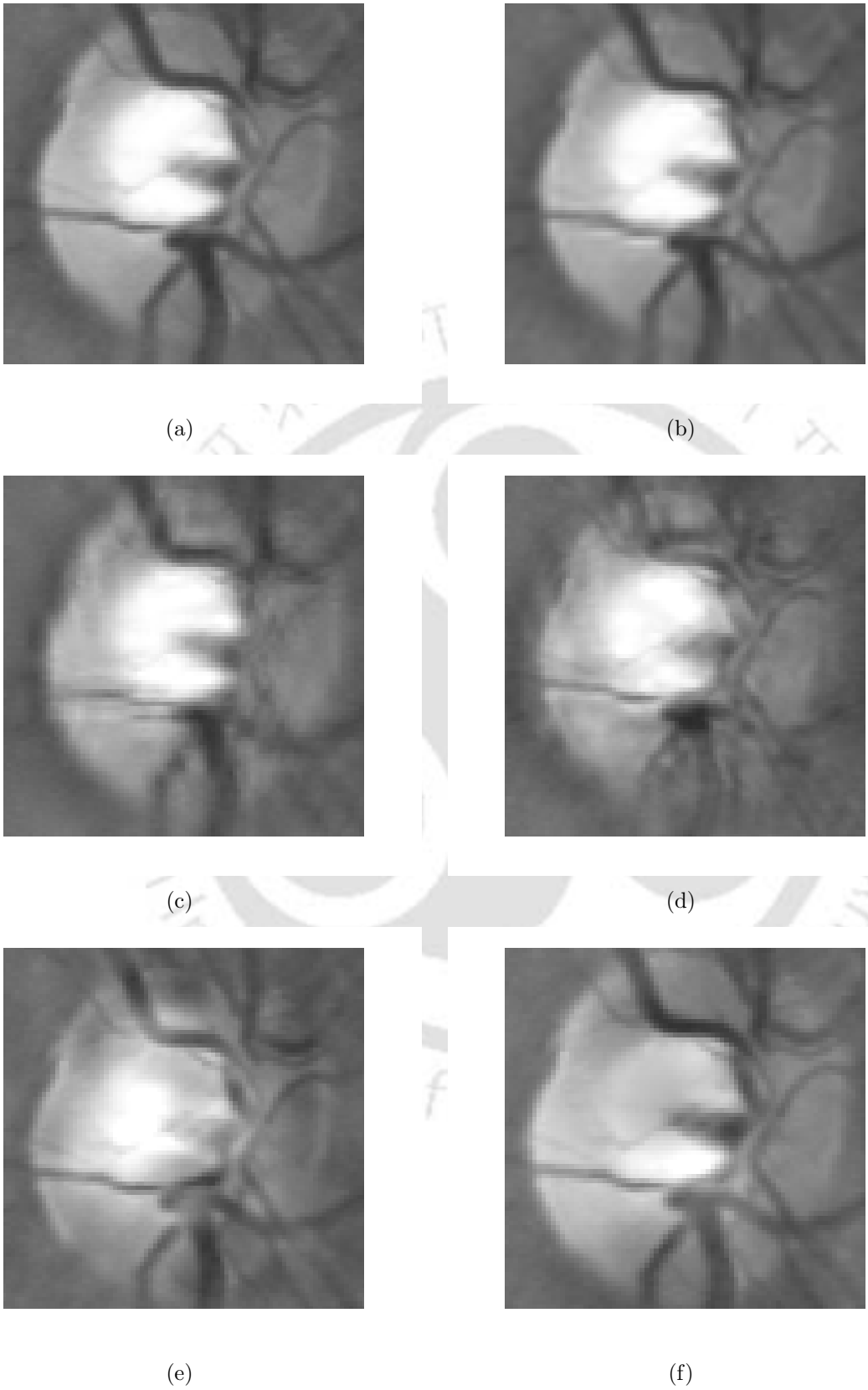

(a) (b) (c) (d) (e) (f)

Figure 3.15: (a) Original and reconstructed OD images when subband coefficients of level (b) L1, (c) L2, (d) L3, (e) L4 and (f) L5 are made zero.

3.4 Optic disc information in different wavelet subbands

In this section, subbands of each level are examined from the point of view of the OD information. The detection and analysis of OD has several potential clinical uses. The OD area is a slowly varying bright homogeneous region interrupted by blood vessels. The intensity variation between the OD and the retinal background is relatively high. Since the OD and macula regions are small compared to the entire retinal image space, their characteristics are effectively studied considering a local region. A region which contains the OD as shown in Figure 3.15(a) is manually selected from the retinal image. The retinal image used in this figure is 36_training from the DRIVE database. Figure 3.15(b) shows OD region of the reconstructed image obtained after zeroing the coefficients of L1 subbands. Compared to the original OD image (Figure 3.15(a)), it is observed that the optic disc structure is well reproduced. This shows that H(1), V(1) and D(1) subband coefficients carry little of OD information. Figure 3.15(c) shows the reconstructed OD image after zeroing only the coefficients of L2 subbands. There is a sharp intensity transition from brighter OD region to the relatively darker background. This may constitute higher frequency components represented by the L2 subbands. When coefficients of these subbands are zeroed, the sharp boundary (edge) of the OD changes to smooth variations and appears to be smeared. This shows that altering the coefficients of L2 subbands has an impact on the OD properties. Figure 3.15(d) shows the OD image after zeroing the coefficients of L3 subbands. It is observed that the OD image is more distorted. In some parts of OD, the boundary is spread into the background. The slow intensity changes inside the OD region are captured by the relatively lower frequency subbands of L3. By zeroing those subbands, more distortion is observed inside the OD region. This results in a lower quality OD image compared to Figure 3.15(c). The observation shows that the coefficients of L3 subbands carry significant information of OD and has comparatively higher importance than L2 subbands. The modified coefficients of L4 subbands have a moderate effect on OD structure as indicated by Figure 3.15(e). Similarly, Figure 3.15(f) indicates that the coefficients of L5 subbands have little influence on OD information. This result shows that L4 and L5 subbands are less significant

Table 3.5: Average SSIM values for the optic disc region

Retinal feature	Decomposition level of zeroed subbands				
	L1	L2	L3	L4	L5
Optic disc	0.9762	0.9065	0.8668	0.9173	0.9563

in carrying the information of the OD. Figure 3.16 shows another example that illustrates the clinical importance of different subbands. The retinal image used in this figure is 38_training from DRIVE database. Similar observations are made when tested with other retinal images.

These effects can also be quantified by estimating the SSIM index values between the original and the reconstructed OD images. The SSIM index values are computed for various retinal images. Table 3.5 shows the average SSIM index values for the case of zeroed subband coefficients of different decomposition level. The lowest SSIM index value of 0.8668 is obtained when L3 subband coefficients are zeroed. Figure 3.15(d) which shows comparatively more distortion, is supported by this lower SSIM index value. The similarity index computed between the original and the image reconstructed by making subband coefficients of L2 zero shows a value of 0.9065. This shows that, the L2 subbands are clinically less relevant compared to L3 subbands. The SSIM index values 0.9173, 0.9563 and 0.9762 are obtained when L4, L5 and L1 subband coefficients are respectively zeroed. The higher SSIM index values indicate that the reconstructed image is close to the original and those subbands are relatively less significant for the OD. Figure 3.16 shows another example that illustrates the clinical importance of different subbands. The retinal image used in this figure is 38_training from DRIVE database.

These experimental results and the SSIM index values show that different subbands can be arranged in the descending order of their clinical information of the OD as $L3, L2, L4, L5$ and $L1$.

3.5 Macula information in different wavelet subbands

The macula is approximately a circular and specialized area of the retina. It is responsible for clear and detailed vision. It is detected as the dark region at the center of retina and within

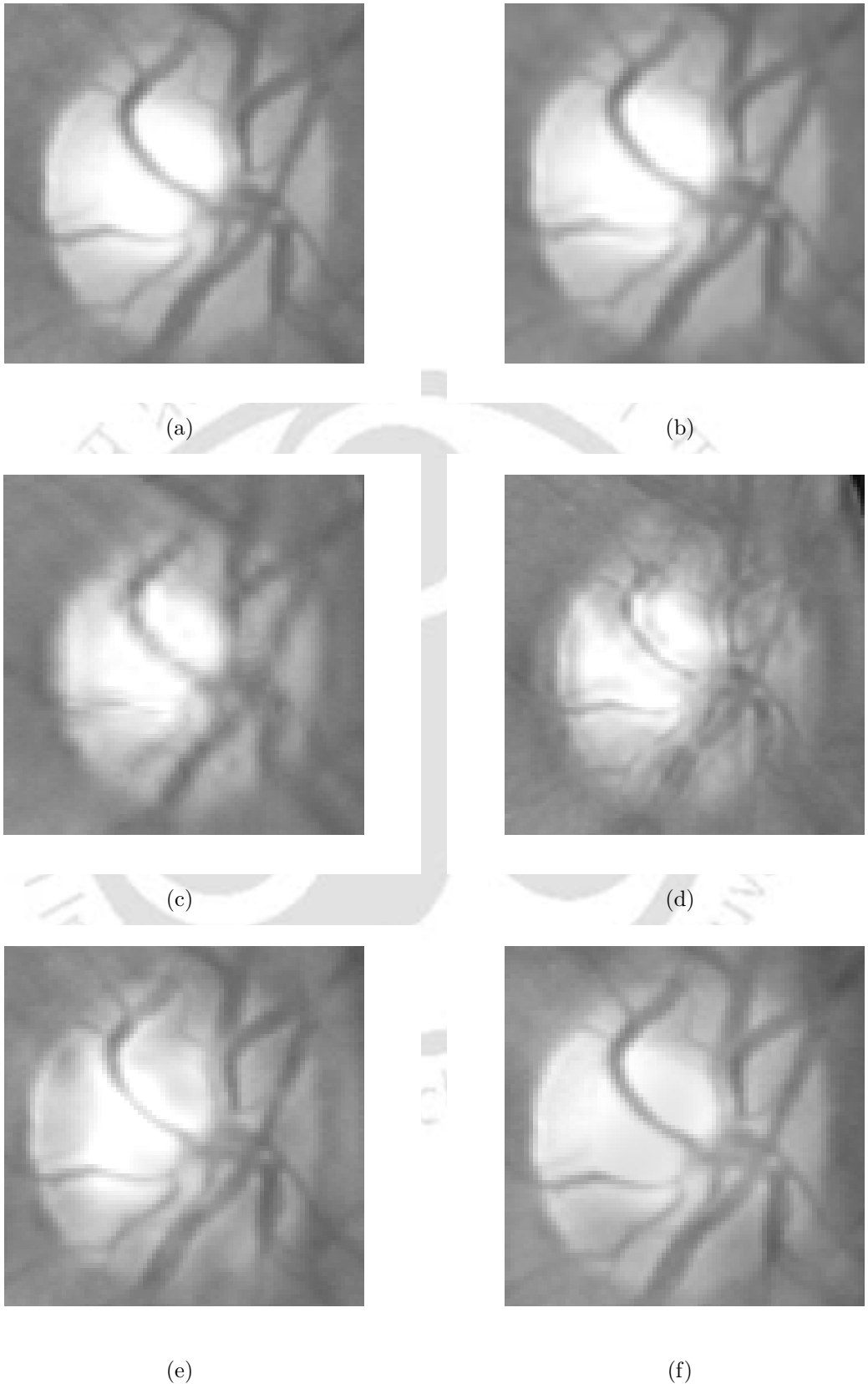

Figure 3.16: (a) Original and reconstructed OD images when subband coefficients of level (b) L1, (c) L2, (d) L3, (e) L4 and (f) L5 are made zero.

Table 3.6: Average SSIM values for the macula region

Retinal feature	Decomposition level of zeroed subbands				
	L1	L2	L3	L4	L5
Macula	0.8768	0.8632	0.9547	0.9879	0.9940

the neighborhood of the optic disc. The macula has the darkest region at its center called the fovea. The relative intensity transition between the macula region and the surrounding retinal region is higher compared to the intensity variation between the fovea to the macular region [12]. A region from the retinal image which contains the macula is manually selected and shown in Figure 3.17(a). The effect of making all the coefficients of L1 subbands zero is shown in Figure 3.17(b). It is observed that the fovea is less distorted but the boundary of macula is spread into the background. This may be due to the information of intensity gradient between the macula and the background, carried by these subbands. Modifying the coefficients of L1 subbands has more effect on the macula region compared to the effect on the fovea. Figure 3.17(c) shows the reconstructed macula image after zeroing the coefficients of L2 subbands. It is observed that the intensity variations of both, the macula and foveal region are smoothed out. It shows that the L2 subband coefficients have significant effect on the entire macula region. Similar experiments on other retinal images shows that the modified coefficients of L2 subbands result in macular distortion but it is comparatively higher than the distortion resulted by zeroing the L1 subbands. This may be due to the intensity variation of the macula region reflected in the high frequency components of L2 subbands. The result of making the relatively lower frequency, L3 subband coefficients zero is shown in Figure 3.17(d). It is observed that, they have a moderate effect on the macula region. The low frequency coefficients of L4 and L5 subbands have minimum influence on the macular information as shown in Figure 3.17(e) and (f). Similar observations are made by evaluating the images shown in Figure 3.18. The retinal image 13_test is used to evaluate the macula information in subbands of different decomposition level.

These effects are quantified by evaluating the SSIM index values between the original and

the reconstructed macula images. Table 3.6 shows the SSIM index values estimated for the case of the macula. The lowest SSIM index value of 0.8632 is obtained when the L2 subband coefficients are zeroed. The distortions observed in Figure 3.17(c) are justified by this low SSIM index value. The lower similarity index points to the significant information loss. This indicates that the L2 subbands carry significant information of the macula region. The SSIM index values of 0.8768 and 0.9547 are obtained when the coefficients of L1 and L3 subbands are zeroed indicating considerable changes in the macula. The high SSIM index values of 0.9879 and 0.9940 are obtained when the L4 and the L5 subband coefficients are made zero respectively. This shows that altering these subbands will have minimal effect on the macula. The visual examinations and the SSIM index values show that different subbands can be arranged in the descending order of their importance with respect to the macula information, as $L2, L1, L3, L4$ and $L5$.

3.6 Summary

The advantage of using the DWT in retinal image analysis is that, image features can be well localized. The retinal image is decomposed into different subbands using the DWT. They contain information at specific frequencies and along specific direction. Each subband can be considered as a version of the original image which contains different amount of image information. Different subbands may have different diagnostic relevance. Hence the diagnostic importance of each subband was investigated. The experimental observations show that out of all the subbands, only certain subbands contain the discriminatory information required for the analysis of different retinal features. From the point of view of blood vessels, the L2 subbands which carry information of the thin vessels are more important compared to other level subbands. The L3 and L4 subbands represent the details of thick vessels than the thin vessels. The L5 subbands are more correlated with the retinal background than the blood vessel structure. The L1 subbands are having minimum information of the blood vessels. Hence the order of diagnostic importance for blood vessel feature is $L2, L3, L4, L5$ and $L1$. To verify the vessel related information in different subbands, segmentation of the blood vessels was

performed. The advantage of the proposed method is that it is easy to implement and does not require any trained classifier to classify the vessel pixels. The experimental investigation shows encouraging results with an average sensitivity of 0.6906, average specificity of 0.9547 and average accuracy of 0.9159.

Similar experiments conducted for the OD resulted in the diagnostic relevance order $L3, L2, L4, L5$ and $L1$. For the macula feature, the relative significance order of the subbands is found to be $L2, L1, L3, L4$ and $L5$.

These observations motivate to develop an objective distortion measure which can treat different subbands differently. Such a distortion measure may be more suitable in evaluating the clinical quality of the processed retinal images.

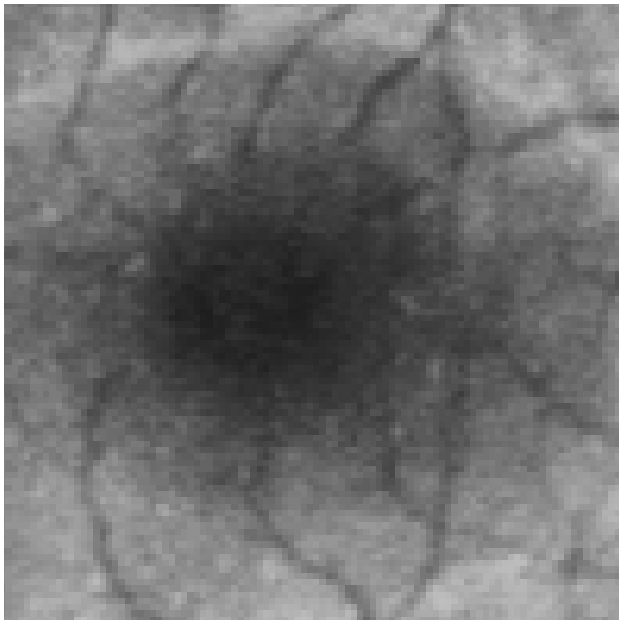

(a)

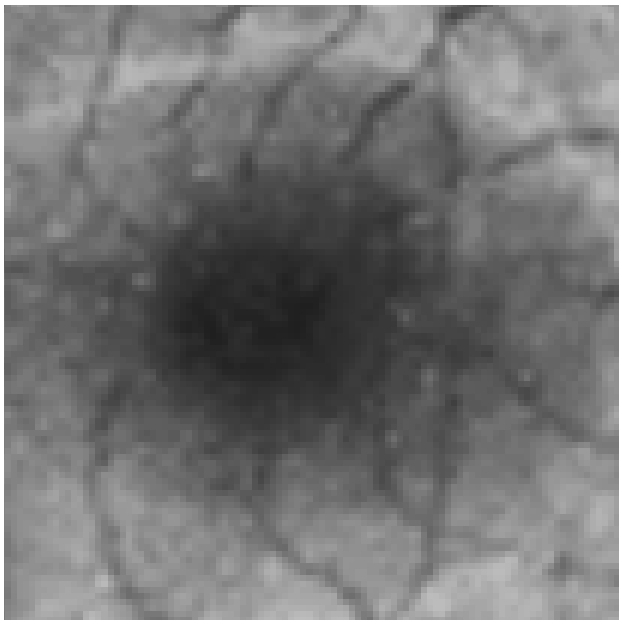

(b)

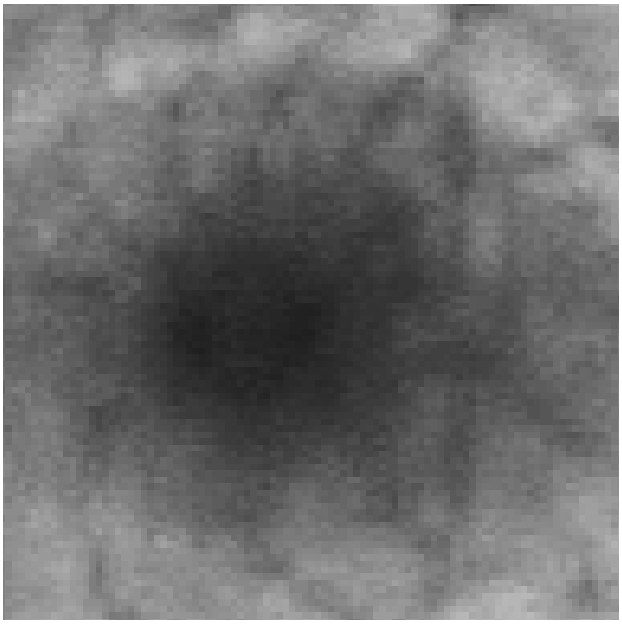

(c)

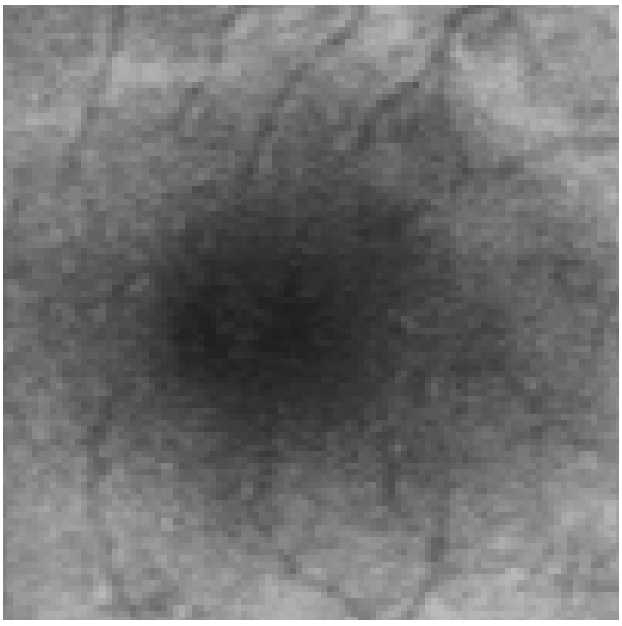

(d)

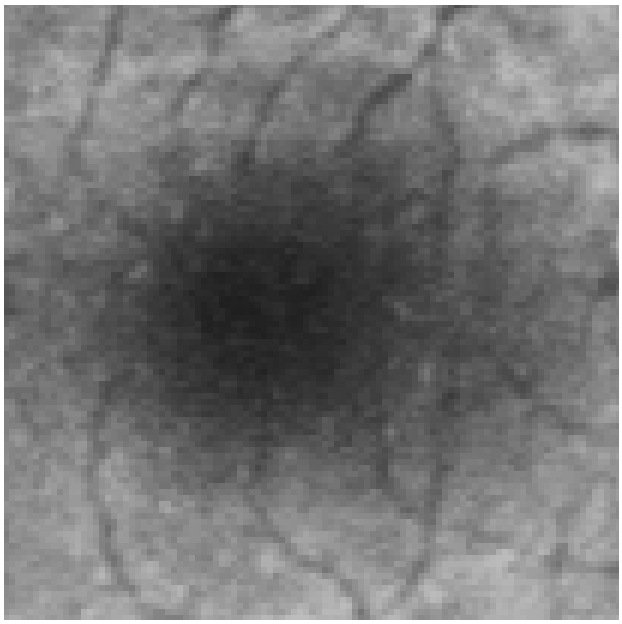

(e)

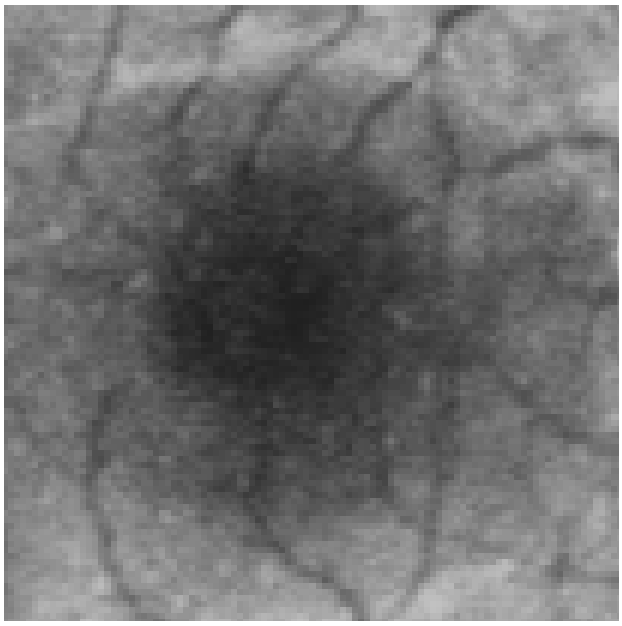

(f)

Figure 3.17: Macula images (a) Original and when subband coefficients of level (b) L1, (c) L2, (d) L3, (e) L4 and (f) L5 are made zero (images are contrast enhanced for better visualization).

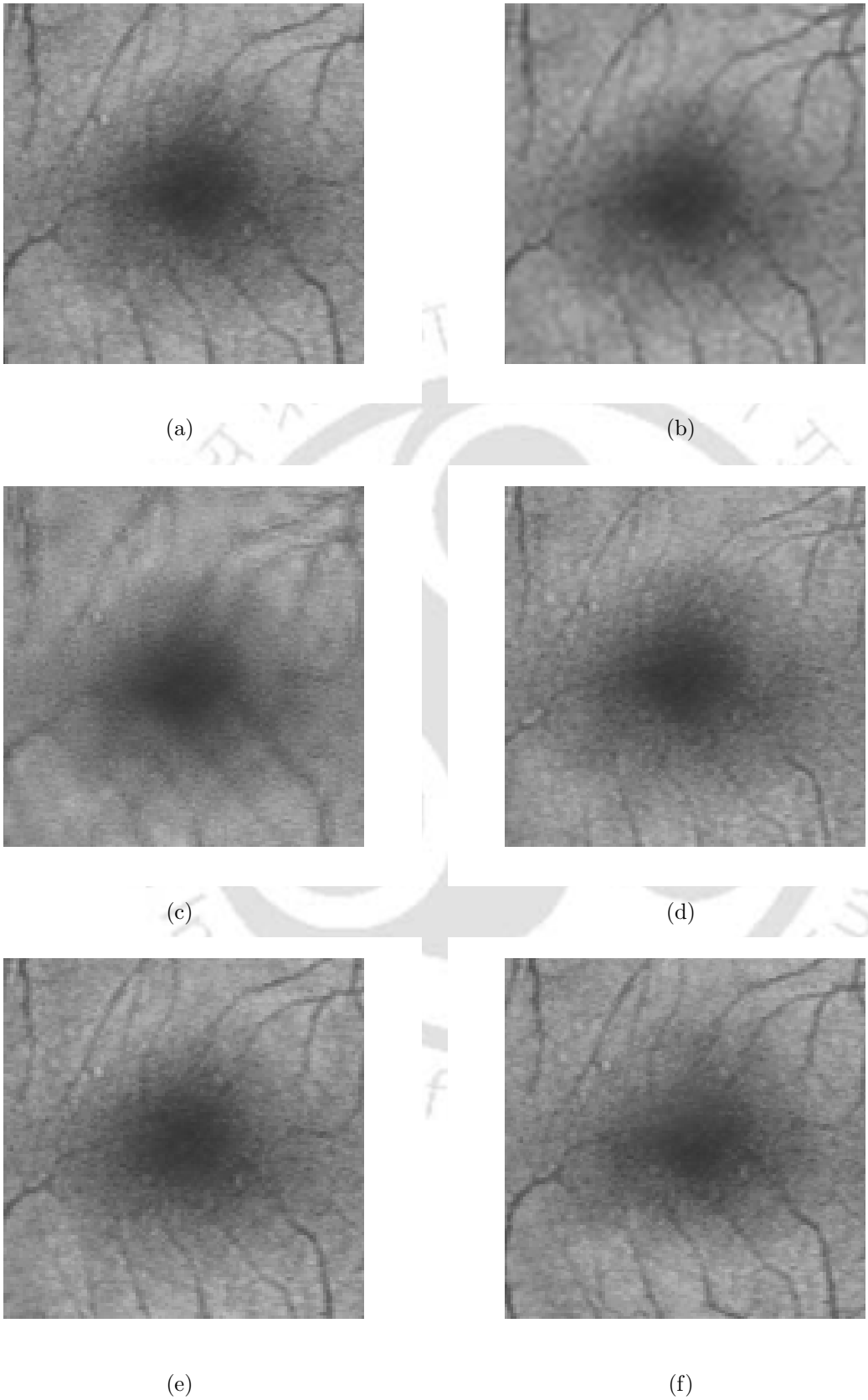

(a) (b) (c) (d) (e) (f)

Figure 3.18: (a) Original and reconstructed macula images when subband coefficients of level (b) L1, (c) L2, (d) L3, (e) L4 and (f) L5 are made zero.

4

Distortion measures in the wavelet domain

Contents

4.1 Proposed distortion measure 90
4.2 Results and discussion 103
4.3 Summary 125

The distribution of clinical feature information in different subbands of the retinal image was investigated in Chapter 3. It was found that different subbands have different diagnostic relevance. The significant information of a retinal feature is captured by only a few subbands. Hence a measure which can treat different subband errors differently will be more suitable in evaluating the clinical quality of the processed retinal images. In this chapter, novel wavelet weighted distortion measures are proposed to quantify the information loss in retinal features. A global distortion measure is defined by combining the individual distortion measures. The distortion measure in wavelet domain is proposed in Section 4.1. The distortion measure for each of the retinal feature is proposed in the subsequent sections 4.1.3, 4.1.4 and 4.1.5. The performance of the proposed measures is evaluated under different conditions and compared with other distortion measures in Section 4.2.

4.1 Proposed distortion measure

After identifying the subbands that contain significant information about a retinal feature, a distortion measure is defined in the wavelet domain. The information loss is quantified as a weighted difference of coefficients in each subband. The error between the significant subbands is given a higher weight. The nonsignificant error is given a lower weight. In this way the distortion measure can emphasize the clinically significant distortion. In this work we propose a wavelet weighted distortion measure WWDM as

$$\text{WWDM} = \sum_{f \in \{v,d,m\}} \text{WWDM}_f \tag{4.1}$$

where $WWDM_f$ is the distortion measure for local clinical feature. $WWDM_f$ is defined as

$$\text{WWDM}_f = \ (\Delta_{\mathbf{e}}^{1/2})^T \cdot \frac{\Gamma_f}{\text{tr}[\ \Gamma_f\ ]} \cdot \ (\Delta_{\mathbf{e}}^{1/2}) \tag{4.2}$$

where Γ_f is the diagonal matrix of subband weights for each of the diagnostic feature and $\Delta_{\mathbf{e}}$ is an error vector with fifteen elements. Each element of $\Delta_{\mathbf{e}}$ is a measure of the error between coefficients of the same subband from the original and the processed image. They can be considered to be one of the DWT based distortion measures discussed in the next subsection.

4.1.1 DWT based image quality measures

The DWT has been used in various biomedical image processing applications such as noise removal, enhancement and detection of diagnostic features [54]. In the DWT domain, significance of different subbands varies with different diagnostic features. A measure which can quantify the subband distortion differentially will be more appropriate in evaluating the diagnostic quality of the reconstructed image. Different wavelet based image quality assessment schemes have been proposed in [86, 87, 112] based on the idea to exploit the characteristics of the HVS. But these works are aimed at evaluating the visual quality of a multimedia image. Various DWT based distortion measures are, wavelet subband MSE (WMSE), relative WMSE (Rel WMSE) and the root of the normalized WMSE (RNWMSE) [86, 87]. The WMSE is expressed as the MSE between the subband coefficients of original image and subband coefficients of the processed image. The WMSE for a subband b with K number of coefficients and at any given decomposition level n ($1 \leq n \leq$ final decomposition level-N) is defined as,

$$\mathrm{WMSE}_{(b,n)} = \frac{\sum_{k=1}^{K}(d_{(b,n)}(k) - \tilde{d}_{(b,n)}(k))^2}{K} \tag{4.3}$$

where d is the wavelet coefficient of original image subband and $\tilde{d}$ is the wavelet coefficient of processed image subband. The Rel WMSE is obtained by normalizing the WMSE with the sum of the WMSE of all subbands. It is given by,

$$\mathrm{Rel\,WMSE}_{(b,n)} = \frac{\mathrm{WMSE}_{(b,n)}}{\sum_{b\in(H,V,D)}\sum_{n=1}^{N}\mathrm{WMSE}_{(b,n)}} \times 100\ \% \tag{4.4}$$

The RNWMSE is given as

$$\mathrm{RNWMSE}_{(b,n)} = \sqrt{\frac{\sum_{k=1}^{K}(d_{(b,n)}(k) - \tilde{d}_{(b,n)}(k))^2}{\sum_{k=1}^{K}(d_{(b,n)}(k))^2}} \times 100\ \% \tag{4.5}$$

These DWT based distortion measures are computed directly from the wavelet coefficients of a subband and they show the average global error. Since all the subbands are equally weighted, the error in the dark background which does not have any clinically relevant information is treated same as the significant distortion. Any distortion in the nondiagnostic region results in

high error values. This may mislead the diagnostic interpretation of the retinal image.

In our proposed method different weights are assigned to different subbands according to their diagnostic importance. The following subsections discuss the computation of weights for different wavelet subbands.

4.1.2 Computation of weights

The diagnostic importance differs for different subbands. The error in each subband contributes to the overall distortion. A measure can better quantify the diagnostic distortion by having different weights for different subband errors. These weighting factors may play an important role in highlighting the diagnostically significant errors from the nonsignificant errors. The weight values are to be calculated using the subband coefficients of the original image. The weight may be computed in various ways.

4.1.2.1 Proposed weight based on the sum of absolute values of wavelet coefficients

The weight factor for a detail subband b at decomposition level n with K number of coefficients may be estimated as the sum of the absolute values of wavelet coefficients $d_{(b,n)}$ within the subband. It is defined as,

$$\omega_{(b,n)} = \sum_{k=1}^{K} |d_{(b,n)}(k)| \tag{4.6}$$

There will be 15 different weights for 15 different wavelet subbands. When these weights are plotted graphically, just for better representation and to make the evaluation simple, we have added the weights of H,V,D bands of a decomposition level and considered as the weight value at that decomposition level. Now the weight matrix with the weight value for each decomposition level as its diagonal elements may be represented as,

$$\Gamma_f = \begin{bmatrix} \omega_{L1} & 0 & 0 & 0 & 0 \\ 0 & \omega_{L2} & 0 & 0 & 0 \\ 0 & 0 & \omega_{L3} & 0 & 0 \\ 0 & 0 & 0 & \omega_{L4} & 0 \\ 0 & 0 & 0 & 0 & \omega_{L5} \end{bmatrix}$$

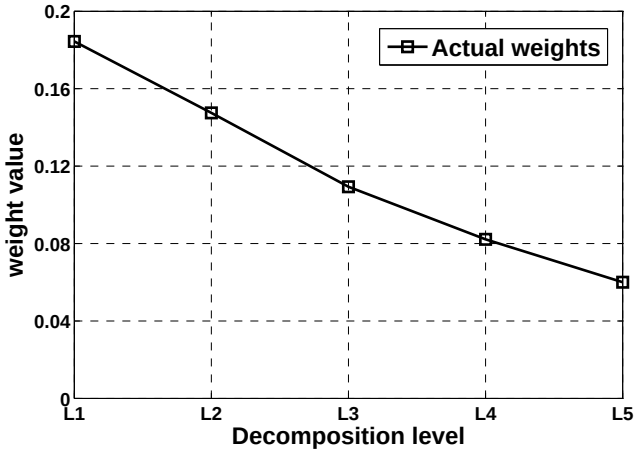

Figure 4.1: Characteristics of weight factor given by Equation (4.6).

Then each of the weight value is normalized by the sum of all the weight values.

For further illustration, the weights are computed for an image (36_training) from the database. Figure 4.1 shows the values of weight factor for all the five decomposition level. The L1 subbands contain a large number of small valued coefficients and summing them all gives a higher weight value. The higher decomposition level subbands have small number of large coefficients and adding them gives a smaller weight values.

The decreasing trend of weight factor from L1 to L5 does not satisfy the order of diagnostic importance for different features. For eg., the decreasing trend of weight factor values from L2 to L5 may be accepted for the case of blood vessels as this satisfies the order of diagnostic influence of subbands. The weight of L1 is expected to have minimum value but shows a higher value. It is also observed that the decreasing weight values from L1 to L5 do not agree with the order of importance of subbands for the OD and the macula.

4.1.2.2 Weight based on the relative subband mean energy (RSME)

The wavelet subband energy is a good measure for signal information content in a subband. The relative subband mean energy (RSME) $\rho_{(b,n)}$ [113] value may be used as the weight factor

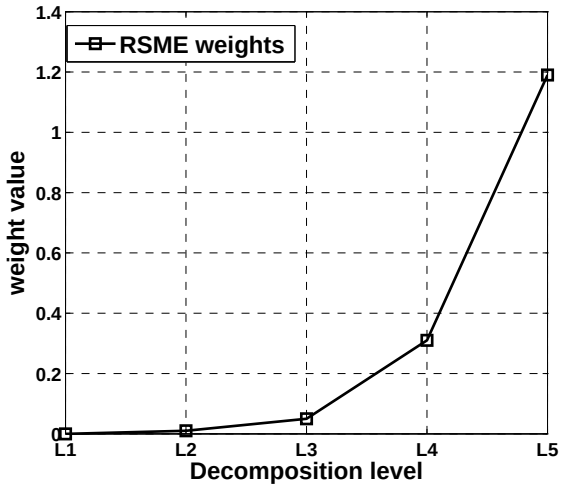

Figure 4.2: Characteristics of RSME weight factor.

for different subband errors.

$$\rho_{(b,n)} = \frac{\bar{E}_{(b,n)}}{\bar{E}_{tot}} \times 100\ \% \tag{4.7}$$

where $\bar{E}_{(b,n)}$ is the mean energy of a subband b, given by

$$\bar{E}_{(b,n)} = \frac{\sum_{k=1}^{K}(d_{(b,n)}(k))^2}{K} \tag{4.8}$$

and $\bar{E}_{tot}$ is the total subband mean energy computed by adding the mean energy of all the detail bands as,

$$\bar{E}_{tot} = \sum_{b\in(H,V,D)} \sum_{n=1}^{N} \bar{E}_{(b,n)}. \tag{4.9}$$

Figure 4.2 shows the weight values computed for the same image (36_training), using $\rho_{(b,n)}$ for different subbands. The L1 subbands have coefficients with small energy and give the small weight. The higher decomposition level subbands have large valued coefficients and give high energy values. The weight factor shows an increasing trend from L1 to L5. The limitation of these weights is that they tend to emphasize the higher order subbands. They do not satisfy the relative diagnostic importance order of different subbands for different features as discussed before.

The approximation band contains the average information about the image. In image pro-

cessing applications, the approximation band coefficients are generally kept unaltered. Hence in this distortion measure, the effect of approximation band coefficients is not considered and the total distortion is computed using only the detail subbands [86]. Then the proposed distortion measure is defined as the weighted difference between wavelet coefficients of the original and the degraded images. The weights for different subbands in the distortion measure are generated from retinal images of size 512×512.

The important details in medical images are the local clinical features. The study and analysis of these features is of great importance when representing the medical image content. Hence the total distortion can be considered as the linear combination of the local distortion measure as given in Equation (4.1). The distortion measure for each of the local clinical features in the retinal image are discussed in the following subsections.

4.1.3 Wavelet weighted blood vessel distortion measure ($\mathrm{WWDM_v}$)

A wavelet weighted blood vessel distortion measure ($\mathrm{WWDM_v}$) is defined using Equation (4.2) to capture the distortion in blood vessels. The $\mathrm{WWDM_v}$ is obtained by considering the feature f as v in Equation (4.2) and $\Delta_{\mathbf{e}}$ is the normalized wavelet subband error vector with fifteen scalar components computed using Equation (4.5). The proposed measure estimates different weights for different subband errors using Equation (4.6) to form the weight matrix Γ_v. The L1 subbands have minimum effect on the blood vessels, they are expected to have small weight factor values. As thin vessels have relatively higher frequency components compared to the thick vessels, the distortions in them are perceived easily even at low compression. Hence the L2 subbands are expected to have higher weight factor values compared to the other subbands. The thick vessels are affected by lower frequency L3 subband coefficients. With the increase in compression values, the low frequency coefficients also start getting affected. Hence the L3 subband error is weighted less than the second level subband error. The L4 and L5 subbands contribute little in carrying the vessel information and hence weighted less than the third level subbands. With all these observations, the weight factor for different subbands are expected to have values in the order $\omega_{L2} > \omega_{L3} > \omega_{L4} > \omega_{L5} > \omega_{L1}$. Figure 4.3 shows the actual values

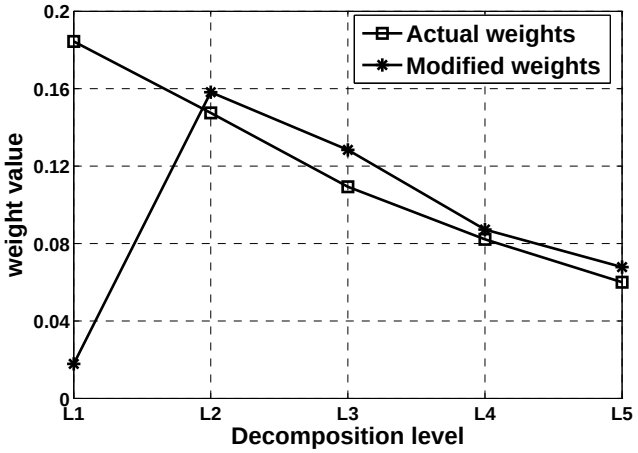

Figure 4.3: Characteristics of weight factor for blood vessels.

of weight factor computed for an image (36_training) from [98]. The weights are computed using Equation (4.6) for different decomposition levels. The decreasing trend of weight factor values from L2 to L5 can be accepted as this satisfies the order of diagnostic influence of subbands. The weight for L1 is expected to have minimum weight factor value, but shows a bigger weight value. This requires the correction of weight value for L1 subbands. The weight factors computed from Equation (4.6) are modified to make them follow the diagnostic order. It is proposed to modify the weight values by using only the coefficients that are comparatively more significant than the other coefficients in a subband. The coefficients which fall within the circular FOV (CFOV) are considered as significant coefficients. The coefficients outside the CFOV represent the dark background and are diagnostically insignificant. They are made zero to reduce their influence on the distortion measure. The wavelet coefficients within the CFOV are extracted using a mask generated for each subband similar to the masks provided in the database (Figure 3.9 (c)). The mask is a binary image of the same resolution of the wavelet subband. This consists of a black background with a white image field (CFOV) indicating the region of significant coefficients as shown in Figure 4.4.

The wavelet coefficients belonging to the CFOV of a subband are arranged in the descending order of their absolute magnitude. A given number of coefficients are selected depending on

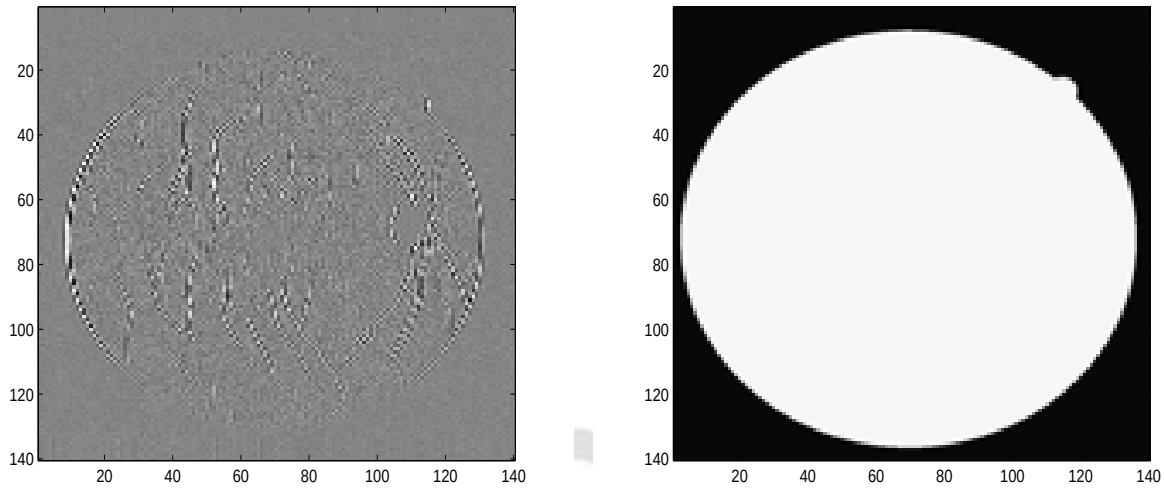

(a) (b)

Figure 4.4: (a) Image of subband V2 (b) mask image.

the importance level of the subband. The higher number of coefficients are selected from those subbands having higher significance. The subbands of L2 are having highest importance and more number of coefficients are selected from them. The absolute sum of the subband coefficients gives a large weight value for the subband. The L3 subbands are having the next higher importance. The number of coefficients selected are slightly less than the case of L1 subbands. This gives a smaller weight to L3 subbands compared to L2 subbands. The L1 is having the lowest importance and only few of the significant coefficients are considered from a large number subband coefficients. Sum of these, gives a smaller weight to the subbands. The number of coefficients considered to compute the weight may slightly vary depending on the image. After working with 35 retinal images from [98], the number of coefficients (in %) used for computing the weights is as follows:

for each subband of L2 - 90 to 100%,

for each subband of L3 - 70 to 90%,

for each subband of L4 - 30 to 50%,

for each subband of L5 - 8 to 10%,

for each subband of L1 - 2 to 4%.

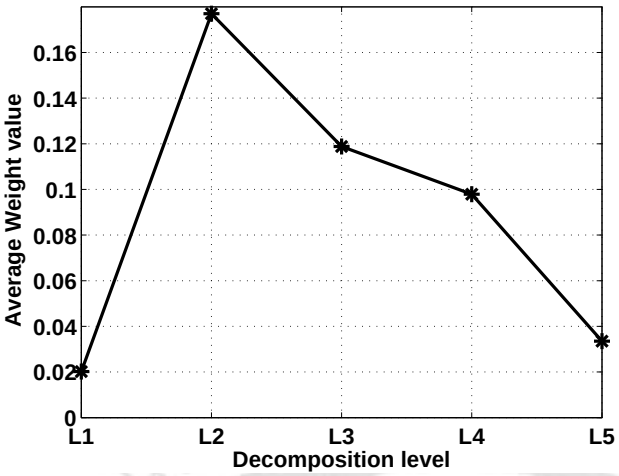

Figure 4.5: Average modified weight factor.

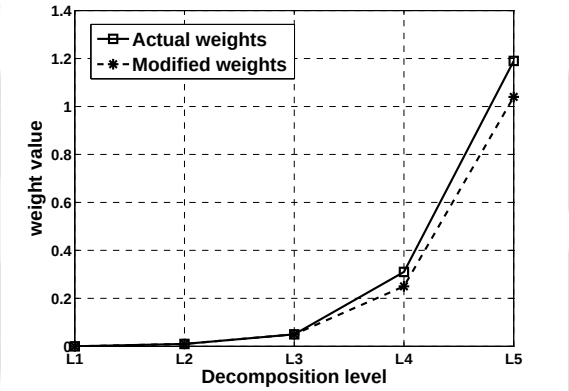

Figure 4.6: Characteristics of RSME weight factor.

Figure 4.3 shows the values of modified weights for different subbands. It is observed that the modified weights satisfy the requirement of relative weight values of subbands. The modified weight values are computed for all the images and the average weight value at each L is shown in Figure 4.5. These modified weight values are expected to capture the error in blood vessel structure effectively.

Following the similar procedure for RSME based weights, Figure 4.6 also shows the modified $\rho_{(b,n)}$ weight values for the same image. It is observed that the weight values still follow the increasing trend and do not satisfy the requirement of relative weight values of subbands. These results show that the weight factor $\omega_{(b,n)}$ can be used to weight the different subband errors.

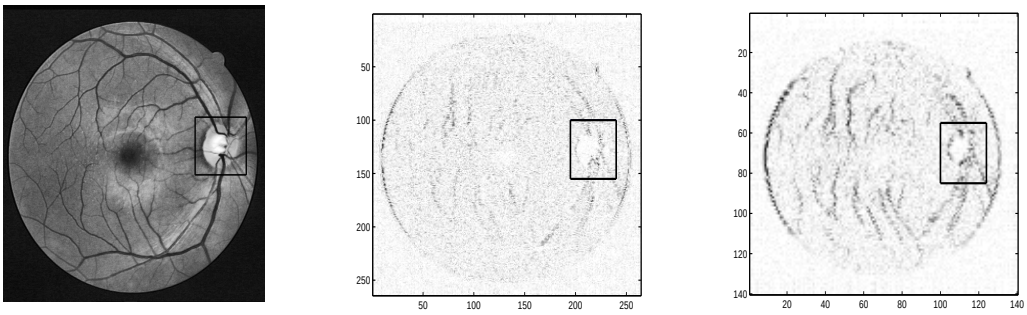

(a) (b) (c)

Figure 4.7: The OD regions (black square) in (a) original image (b) subband V1 (b) subband V2.

4.1.4 Wavelet weighted distortion measure for the optic disc ($\mathrm{WWDM_d}$)

The wavelet weighted distortion measure for the optic disc ($\mathrm{WWDM_d}$) is proposed to quantify the distortion in the OD of processed retinal images. The weights for different subbands are estimated using Equation (4.6). The weights are computed using only those wavelet coefficients that lie within the *OD region in each subband*. In standard retinal images, the OD is approximately a region of 80×80 pixels [29]. A candidate area of 100x100 pixel is considered as the OD region. Such regions are selected manually from each subband as shown in Figures 4.7(b) and 4.7(c).

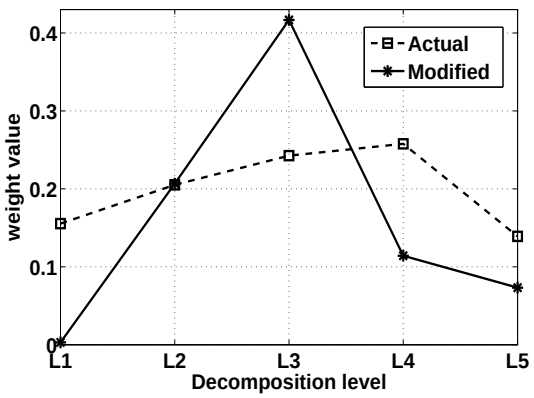

Figure 4.8: Characteristics of the actual and modified weight factors for the optic disc

The diagonal weight matrix Γ_d can be generated by putting the actual weight values as the

diagonal elements. Figure 4.8 shows the weight values for different decomposition levels. It is observed that the actual weight of L4 subbands is high compared to the L2 and L3 subbands. The weight of L1 subbands is expected to be minimum but indicates a value higher than that of the L5 subbands. These weight values do not follow the relative diagnostic importance order of subbands ($L3, L2, L4, L5$ and $L1$) for the OD as discussed earlier. Therefore, the weight factors have to be modified to satisfy the order of diagnostic relevance. As in the case of blood vessels, it is proposed to modify the weight values by using only the coefficients that are comparatively more significant than the other coefficients in a subband. The wavelet coefficients belonging to the OD region in a subband are arranged in the descending order of their absolute magnitude. The number of selected coefficients is decided depending on the significance of the subband.

For an image of 512×512, the L1 subbands are of dimension 256×256 pixels. The region containing the OD in each subband is approximately of size 60×60. If, the first 100 higher magnitude coefficients out of 60×60=3600 coefficients are considered, then it is approximately 3 % of the total coefficients which are used for computing the weight for a subband. The number of coefficients considered may slightly vary between 2 to 4 % depending on the image. The L3 is having highest importance and more number of coefficients are selected from the OD region (16×16) of H3, V3 and D3. The absolute sum of all these coefficients gives a large weight value for each of the subband. Similarly the weight for L2 subbands is computed using 70 - 90 % of the coefficients in the OD region. The size of the region in L2 subbands representing the OD is approximately 30×30. From the total coefficients, 700 to 800 coefficients are considered to compute the weight. The weights of L4 subbands have to be less than the weights of L2 subbands. Hence 20 to 30 coefficients are considered from a total of 8×8=64 coefficients. The L5 is having lower significance than L4. The weight is computed by considering only 8 to 10% of the total 5×5=25 coefficients. The number of coefficients (in %) used for computing the weights is as follows:

for each subband of L3 - 90 to 100%,

for each subband of L2 - 70 to 90%,

for each subband of L4 - 30 to 50%,

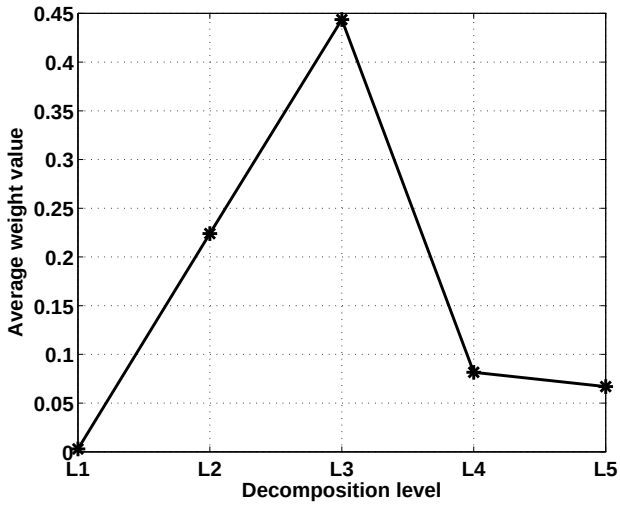

Figure 4.9: Average modified weight factor.

for each subband of L5 - 8 to 10%,

for each subband of L1 - 2 to 4%.

The modified weight value Γ_d at each L for the same image is shown in Figure 4.8.

The average modified weight value for the whole set of images is shown in Figure 4.9. The weight values satisfy the order of relative diagnostic significance of subbands. These modified weight values may be more appropriate to quantify the distortion in the optic disc.

4.1.5 Wavelet weighted distortion measure for the macula ($\mathrm{WWDM_m}$)

A wavelet weighted distortion measure ($\mathrm{WWDM_m}$) is proposed to capture the changes in the macula of processed retinal images. The weights for different subbands are computed using Equation (4.6). For computation of weights, a small region which contains the macula is considered. The macula occupies only a small retinal region (< 1.5 %) [114]. The region containing the macula in each subband of L1 is considered approximately of size 60×60. Similar to the case of OD, the region containing the macula in the subbands of L2, L3, L4 and L5 is considered. The weights are generated using only those wavelet coefficients that lie within this region in each subband. An example of a weight matrix Γ_m with actual weights computed for an image (36_training) having diagonal elements as weight values for each decomposition level

is given by

$$\Gamma_m = \begin{bmatrix} 0.424 & 0 & 0 & 0 & 0 \\ 0 & 0.275 & 0 & 0 & 0 \\ 0 & 0 & 0.175 & 0 & 0 \\ 0 & 0 & 0 & 0.071 & 0 \\ 0 & 0 & 0 & 0 & 0.055 \end{bmatrix}$$

These weight values are required to follow the relative importance order of subbands ($L2, L1, L3, L4$ and $L5$). It is observed that the actual weights for L3 to L5 subbands satisfy the diagnostic order of the subbands. The weight value of L1 subbands is expected to be lower than L2 subbands but the calculated weight shows a higher value. The weight values are modified as discussed in the subsection 4.1.4. To calculate the modified weight for L2 subbands, all the coefficients within the macula region are considered. The weight for L1 subbands is computed using approximately 3000 coefficients from a total of 3600 coefficients. The L3 is having lower importance and 100-120 coefficients are selected from the macula region of approximately 16×16. The L4 subbands are having lower importance than L3 and very few coefficients are used to compute the weights. The L5 subbands are having least importance and only a couple of of the coefficients from a total of 5×5=25 coefficients are used to compute the weights. The modified weights are computed using the following number of coefficients: (in %),

for each subband of L2 - 90 to 100%,

for each subband of L1 - 70 to 90%,

for each subband of L3 - 30 to 50%,

for each subband of L4 - 8 to 10%,

for each subband of L5 - 2 to 4%.

The weight matrix Γ_m with modified weight values and satisfying the relative importance

order of subbands, is given by

$$\Gamma_m = \begin{bmatrix} 0.163 & 0 & 0 & 0 & 0 \\ 0 & 0.278 & 0 & 0 & 0 \\ 0 & 0 & 0.061 & 0 & 0 \\ 0 & 0 & 0 & 0.045 & 0 \\ 0 & 0 & 0 & 0 & 0.034 \end{bmatrix}$$

The average modified weight values at each L is shown in Figure 4.10. These new weights are expected to be more effective in highlighting the error in macula.

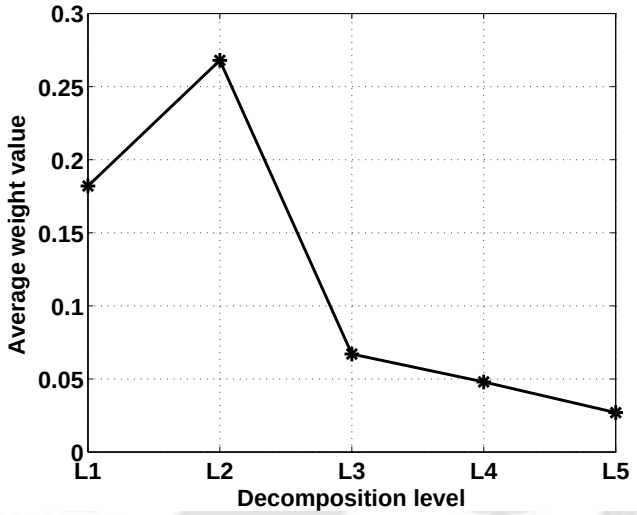

Figure 4.10: Average modified weight factor.

4.2 Results and discussion

The retinal images are taken from test and training set of images in [98]. In the present work, gray level retinal images are used. The images are resized to (512×512) and decomposed to five levels using the biorthogonal wavelet filter. In this section the performance of the DWT based distortion measures is evaluated and compared with that of the proposed distortion measures. The performance of the proposed wavelet weighted distortion measures for the OD, the macula and the blood vessels are also evaluated separately.

4.2.1 Evaluation of the DWT based distortion measures

In this subsection, the performance of different wavelet based distortion measures (Equations (4.3)-(4.5)) are evaluated when they are used to quantify the distortion in different retinal features. These distortion measures can be considered as having uniform weights and treating all the subband errors equally. Each of the measure performs differently for the distortions occurring in different retinal features.

Introducing distortion in retinal features

The distortion considered in this work is smoothing of the retinal features. The smoothing of the image structures may occur during the process of lossy compression [69, 115–117]. The process of compression involves truncation of high frequency details. During quantization, the high frequency wavelet coefficients are made zero. This results in the loss of details and smoothing of the image. Smoothing is also experienced during the process of image denoising. The smoothing distortion is introduced by using a Gaussian smoothing filter available in Matlab [118]. The standard deviation σ of the Gaussian filter is varied to have different amount of smoothness. This gives the reconstructed images. Then the distortion is computed between the original image and the reconstructed image. To simplify the computation, the distortions computed for H, V, D bands of a given decomposition level are summed up and it is considered as the total distortion value at that decomposition level.

4.2.1.1 Distortion in blood vessels

In this subsection, the performance of different wavelet based distortion measures is evaluated when they are used to quantify the distortion in blood vessels. Our earlier experiments showed that, the local error due to the thick vessel distortion mostly appears at the third decomposition level (L3) and small errors appear at second and fourth levels. Similarly, most of the error due to thin vessel distortion is present at L2. A distortion measure is clinically useful if it gives greater importance to the distortions in the diagnostic features and not to the distortions due to background noise. To check whether the distortion measures satisfy all these conditions, a simple test is conducted. A section of the thick blood vessel is considered and the smoothing

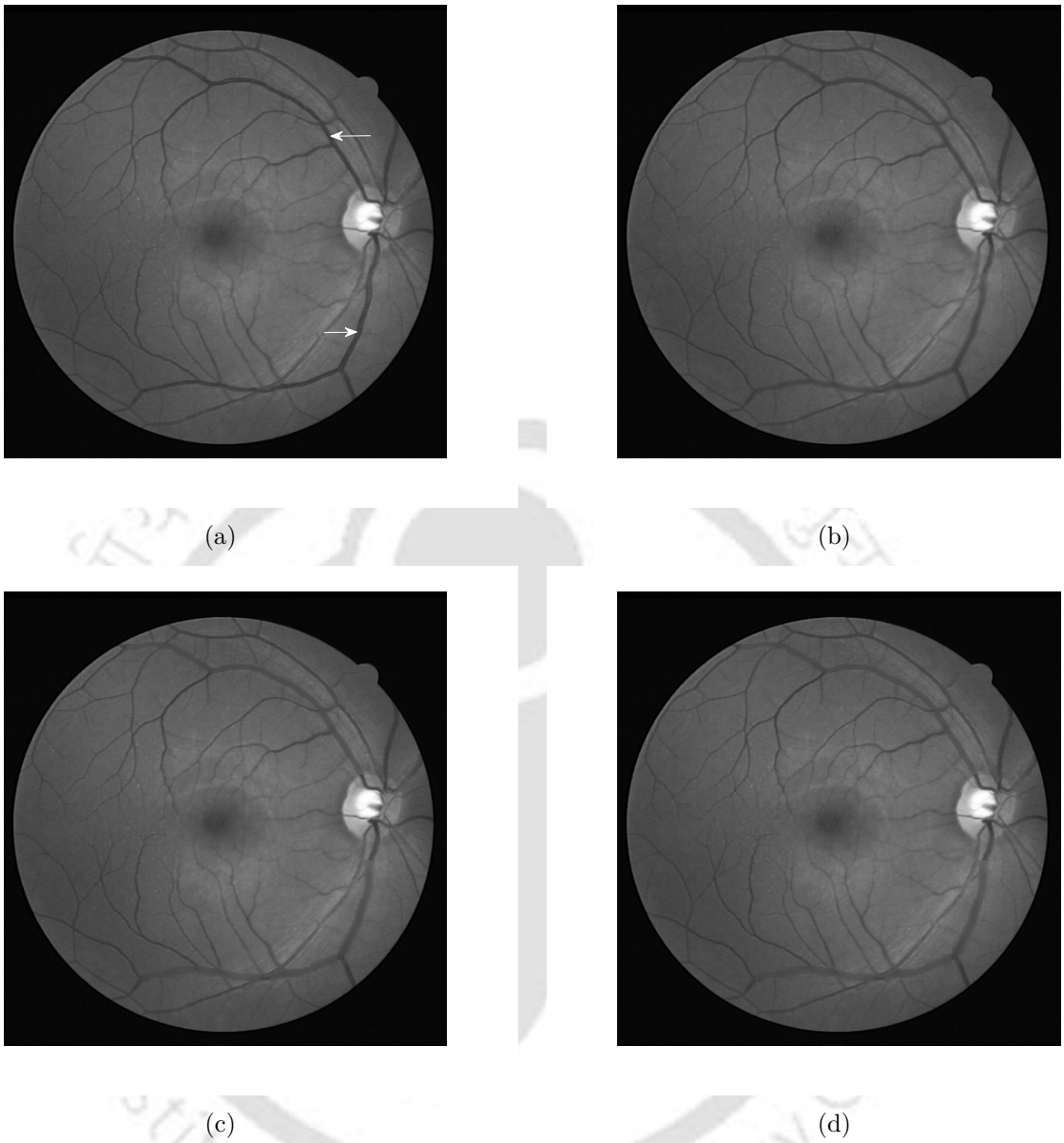

Figure 4.11: (a) Original image showing the two thick vessels (b), (c) and (d) processed images showing increased distortion in the thick vessels.

distortion is introduced artificially. The distortion in the thick vessel is progressively increased by increasing the smoothing parameter σ. The different images of Figure 4.11 shows increasing distortion in the thick vessels.

The distortion values are estimated for all the decomposition levels from L1 to L5 and are shown in Figure 4.12. The variation in WMSE for blood vessel distortion is shown in Figure 4.12(a). It shows increasing WMSE value for L3, L4 and L5. As the distortion increases,

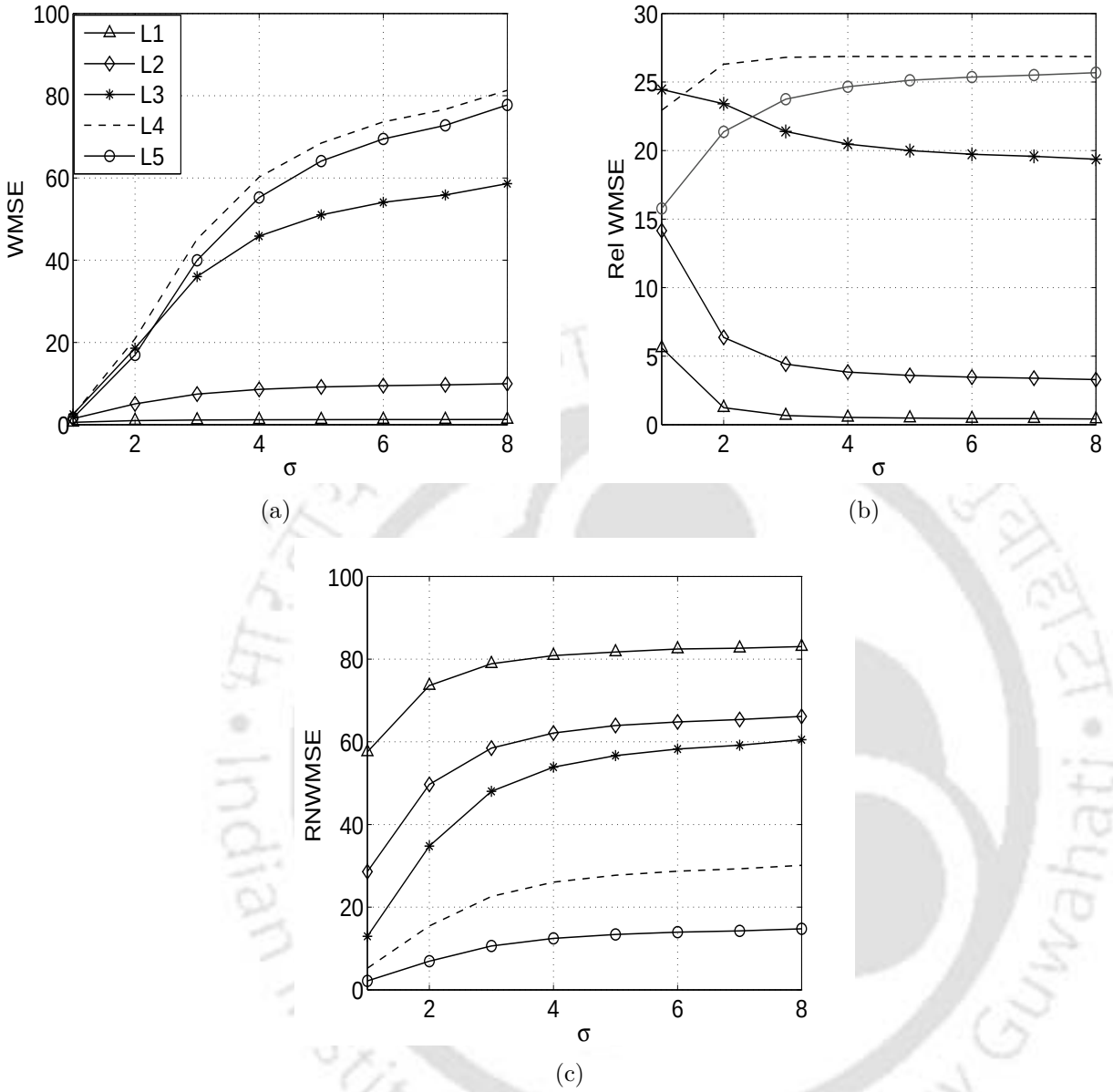

Figure 4.12: Behavior of (a) WMSE, (b) Rel WMSE and (c) RNWMSE at different decomposition level, when the distortion is progressively increased in the thick vessel. x-axis indicates increase in the smoothness (σ)

the increase of WMSE at L3 is less than the increase in L4. The L5 subbands which are less significant from the point of view of the thick vessel information shows higher values of the WMSE. The subbands of L2 which are relatively more significant than L4 shows slow variation with the increase in blood vessel distortion. Figure 4.12(b) shows the Rel WMSE values for thick vessel distortion. The error in L3 slightly high in the beginning but decreases with increase

in the blood vessel distortion. The error in L4 subbands increases slowly whereas the error in L5 subbands shows an increasing trend. It is observed that the L2 subbands, which are more significant than L4 subbands shows decreasing error values compared to L4. The L5, being less significant shows lower error values. The behavior of WMSE and Rel WMSE shows that a considerable amount of error is present at L4 and L5 subbands while the error in them is expected to be minimum. The behavior of RNWMSE in Figure 4.12(c) shows that L1 carries more of the distortion than that of the expected levels L3 and L2. These observations indicate that the aforementioned distortion measures are unable to satisfy the diagnostic importance order. Hence they fail to capture the loss of blood vessel information. Similar tests are extended to evaluate the measures for the case of the distortions in optic disc and macula.

4.2.1.2 Distortion in the optic disc

In this subsection, different wavelet based distortion measures defined earlier are evaluated for their ability to capture distortion in the OD. A distortion measure is expected to emphasize the distortion in a diagnostic feature and ignore the distortion in nondiagnostic regions. To investigate the effectiveness of these distortion measures, a simple experiment is conducted. The optic disc region is altered by a smoothing process. The Gaussian smoothing is performed to different levels as shown in Figure 4.13.

All the distortion measures are computed in each case. The total distortion value for all the decomposition levels is computed. Figure 4.14 shows the behavior WMSE, Rel WMSE and RNWMSE at all decomposition levels. Figure 4.14(a) shows the variation of WMSE for increasing distortion in the OD. The WMSE value shows an increasing trend for subbands of L3 and L4. The error in the L4 subbands is expected to be lower than L2 subbands, instead it shows a higher variation. The L2 subbands carry significant information and are anticipated to follow closely the increased distortion in OD. But the WMSE for the L2 subbands shows a slow variation compared to L3 and L4. The variations of Rel WMSE in Figure 4.14(b) indicate that L3 shows slowly decreasing values. But it is expected to vary sharply with the distortion in OD as L3 subbands are more significant than other subbands. The L2 subbands

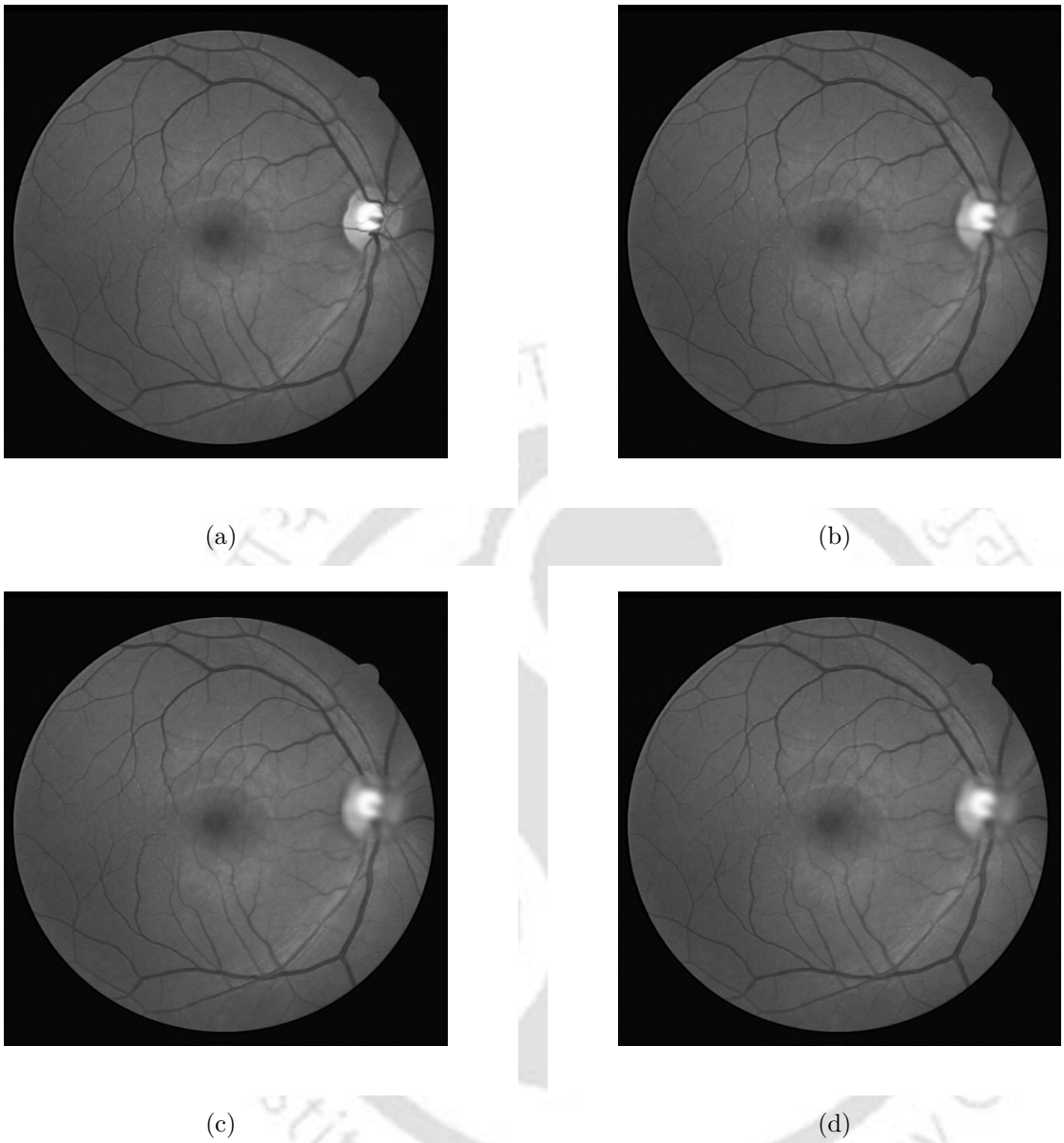

(a) (b)

(c) (d)

Figure 4.13: (a) Original image showing the OD (b), (c) and (d) processed images showing increased distortion in the OD.

which are quite important, show low error values compared to the L4 subbands. Figure 4.14(c) shows the increasing RNWMSE behavior at L2, L3 and L4. L3 subbands are supposed to show comparatively more significant variations than L2, but the measure fails to satisfy this condition. The L1 subbands carry minimum information about OD and are expected to show the minimum variation. But it is not followed by the RNWMSE. All these observations indicate that the above mentioned DWT based distortion measures are unable to satisfy the diagnostic

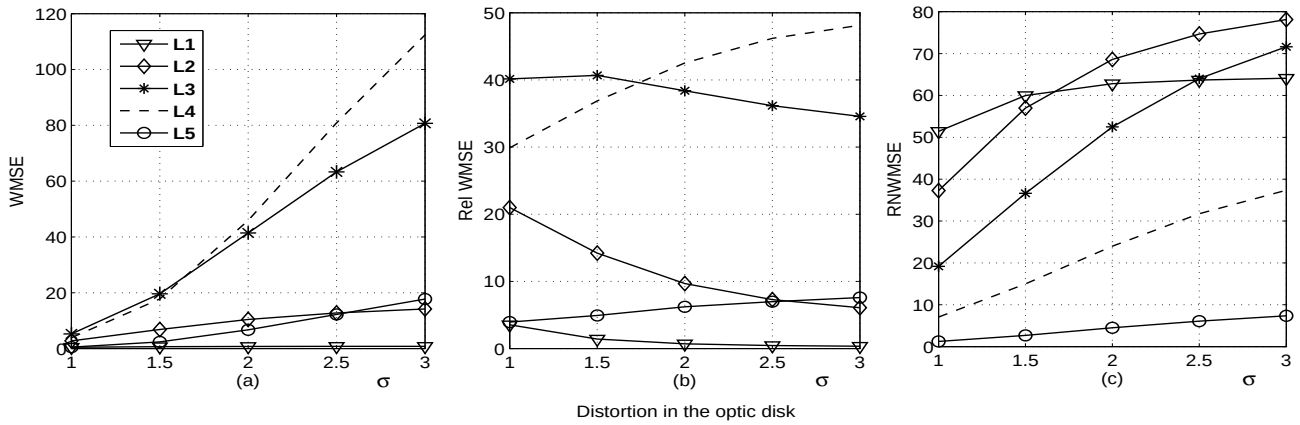

Figure 4.14: Behavior of WMSE, Rel WMSE and RNWMSE at different decomposition levels: x-axis indicates the increase of smoothness (σ).

Table 4.1: Performance of the wavelet based distortion measures when macula of the retinal image is distorted

Distortion measure	Distortion computed at each L					
	L1	L2	L3	L4	L5	Total distortion
WMSE	0.138	0.696	1.949	1.471	0.886	5.139
Rel WMSE	2.414	12.212	34.120	25.825	15.550	90.201
RNWMSE	32.452	19.373	11.875	4.427	1.633	69.760

importance order and to quantify the distortion in OD.

4.2.1.3 Distortion in the macular region

In the light of earlier observations and discussions, the error due to macular distortion mostly appears at the subbands of L2, L1 and a small error appears at the L3 subbands. A test is conducted to verify whether these DWT based distortion measures satisfy this condition or not. A region from the retinal image containing macula is considered manually and the distortion is introduced artificially. The macular region is distorted by the Gaussian smoothing so that it looks blurred. Artificially distorting the macular structure changes its characteristics. The error values are estimated for each of the subbands and for all the decomposition levels. The results of the test are shown in Table B.1. The distortion measures WMSE and Rel WMSE show high values in subbands of L3, L4 and L5 compared to those in L2 subbands. The

measure RNWMSE shows higher value of error in L1 subbands compared to all other levels. This suggests that the DWT based distortion measures are unable to highlight the distortion in the macular region.

The observations made from the above examples show that the wavelet based distortion measures are not able to capture the distortion in the retinal features. This problem may be solved by using different weights for different subband errors. This helps to emphasize the distortion in clinically important subbands. The weighted distortion measures may be more meaningful in quantifying the distortion in retinal features.

The different subband errors need to be weighted differently according to their diagnostic significance. The DWT based distortion measures are weighted with the actual and modified weight values and their performance is evaluated. Figure 4.15 shows weighted DWT based distortion measures. When the L1 subbands are made zero the distortion measure is expected to show minimum distortion value as the reconstructed image is very much similar to the original image. Zeroing L2 subbands distort the thin vessels and leads to a large distortion value. Similarly when L3 subbands are zeroed the distortion measure is again a large value which is slightly less than L2 zero case but higher compared to other cases like zeroing the subbands of L4 and L5. A small amount of thick blood vessel distortion occurs when L4 bands are zeroed and no diagnostic features are distorted when L5 subbands are zeroed thereby giving a low distortion measure value. Figure 4.15(a) shows the behavior of weighted WMSE (wWMSE), weighted Rel WMSE (wRel WMSE) and weighted RNWMSE (wRNWMSE). The wWMSE value is minimum when L1 subbands are zeroed and increases to the maximum value when L5 subbands are zeroed. The wRel WMSE shows approximately same amount of distortion for L1 and L2 subbands zero condition and then slowly decreases. The wRNWMSE also behaves in the same way being maximum initially and then decreasing gradually. This may be due to the ineffective value of weights for different subbands. The performance can be improved by modifying the weight values. Figure 4.15(b) shows the improved performance of the distortion measures using the modified weights. The behavior of wWMSE still remains the same whereas the performance of wRel WMSE and wRNWMSE is improved by showing low error values for

the case of zeroing L1 subbands. In this thesis the RNWMSE is used to compute the error between original and reconstructed image subbands. Under this condition wRNWMSE is one of the proposed $WWDM_f$s.

4.2.2 Performance of the individual distortion measures

In this subsection, the performance of the distortion measure for each of the features is evaluated. The distortion measure $\mathrm{WWDM_f}$ is expected to respond strongly when a particular retinal feature f is distorted and to be less sensitive for any changes in other features. The performance is evaluated by introducing distortion in different regions of the retinal image shown in Figure 4.16.

4.2.2.1 Evaluation of the blood vessel distortion measure ($\mathrm{WWDM_v}$)

The proposed measure is required to highlight the distortion in blood vessels. The performance of the $\mathrm{WWDM_v}$ is investigated under different conditions:

(i) comparing with relative subband mean energy weights

(ii) introducing distortion artificially into the blood vessels keeping all other features undisturbed

(iii) introducing distortion in clinically nonsignificant regions

(iv) introducing distortion in other features such as the optic disc and the macula.

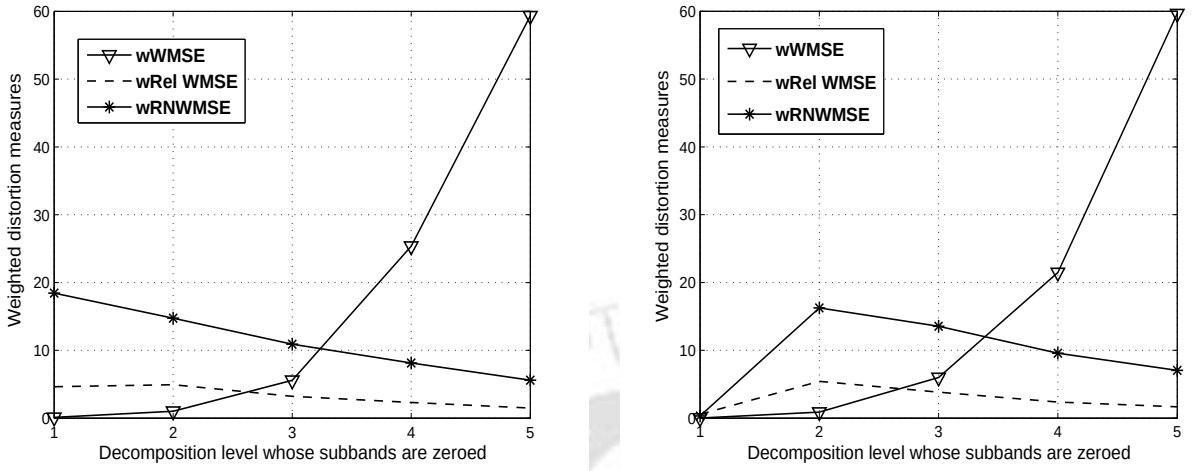

Figure 4.15: Weighted distortion measures under subbands zero condition (a) weighted with actual weight values and (b) weighted with modified weight values.

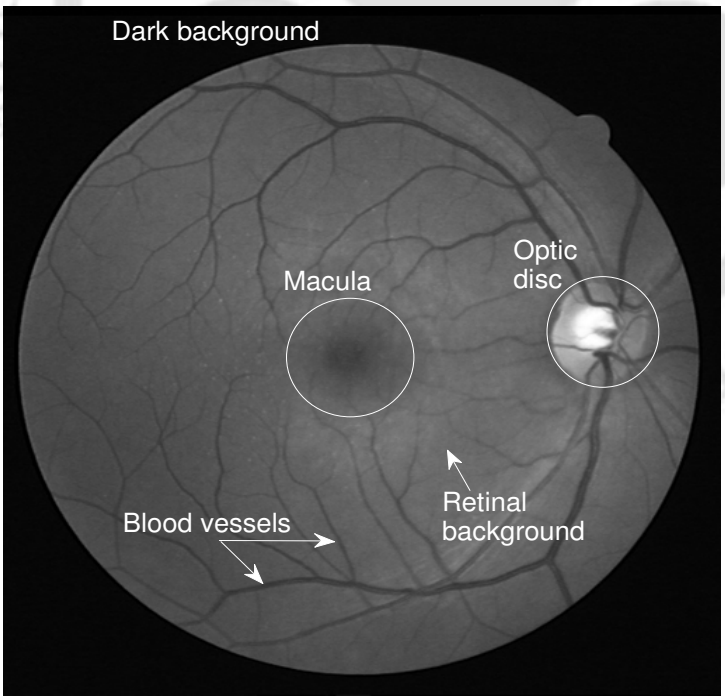

Figure 4.16: Retinal image showing different regions.

Table 4.2: Performance of the proposed measure when a particular decomposition level (L) subbands are zeroed

L of zeroed subbands	Using the proposed weights					$WWDM_v$ (%)	Using the RSME weights					$WWDM_v$ (%)
	L1	L2	L3	L4	L5		L1	L2	L3	L4	L5	
L1=0	0.4422	0.2303	0.1109	0.0843	0.0468	0.9145	0.0028	0.0059	0.0286	0.1848	0.5478	0.7698
L2=0	0.0080	17.9486	0.2999	0.1106	0.0672	18.4342	0.0001	0.4436	0.0786	0.2295	0.7853	1.5370
L3=0	0.0063	0.8984	12.7956	0.4053	0.2083	14.3140	0.0000	0.0251	3.1734	0.8695	2.4458	6.5137
L4=0	0.0068	0.6546	1.7764	9.5863	0.5223	12.5463	0.0000	0.0183	0.4913	19.4464	6.0938	26.0499
L5=0	0.0021	0.2656	0.7981	1.5464	6.4876	9.0998	0.0000	0.0074	0.2209	3.4577	70.9939	74.6799

(i) Using the weights based on relative subband mean energy

Subsection 4.1.2 suggests that the weight can also be computed from the energy of wavelet coefficients. Now all the distortion measures are computed using the RSME weights ($\rho_{(b,n)}$) and their performance is verified under the condition of zeroing different subbands. Table 4.2 shows the comparison of proposed $WWDM_v$ with RSME weighted blood vessel distortion measure. Following the order of diagnostic influence, the proposed $WWDM_v$ indicates a high value of 18.4342 for the case of zeroed L2 subbands and a low value of 0.9145 when L1 subbands are made zero. The values in the seventh column shows that the proposed measure emphasizes the diagnostically significant error and gives less importance to the nonsignificant error. The RSME weighted measure shows a high value of 74.6799 for L5 bands zero condition which are considered as diagnostically less significant. The total distortion values in the last column of RSME weighted measure shows a low distortion value of 1.5370 when L2 subbands are zeroed and 6.5137 when L3 subband coefficients are zeroed. This shows the inability of the RSME weighted measure in highlighting the significant diagnostic distortion. This may be due to, the weights assigned for different subbands are inefficient to bring the diagnostically nonsignificant error to a low value. Thus the proposed $WWDM_v$ may be more suitable in assessing the quality of blood vessel features in a retinal image.

(ii) Introducing artificial distortion into the blood vessel

In this case, we evaluate the $WWDM_v$ by introducing distortion in the blood vessels. Artificially distorting the vessel alters the size and contrast of the blood vessels. In this approach the thick vessels are artificially distorted by Gaussian smoothing so that the vessels look blurred. This is tested for different levels of smoothing. Figure 4.17(a) shows a section of the thick blood vessel from the original image. Figure 4.17(b) shows the same vessel from the reconstructed image, obtained after Gaussian smoothing of the vessel. This process alters the cross sectional intensity profile of the vessel.

Figure 4.18 shows the spread of the intensity profile for different levels of smoothing. It is

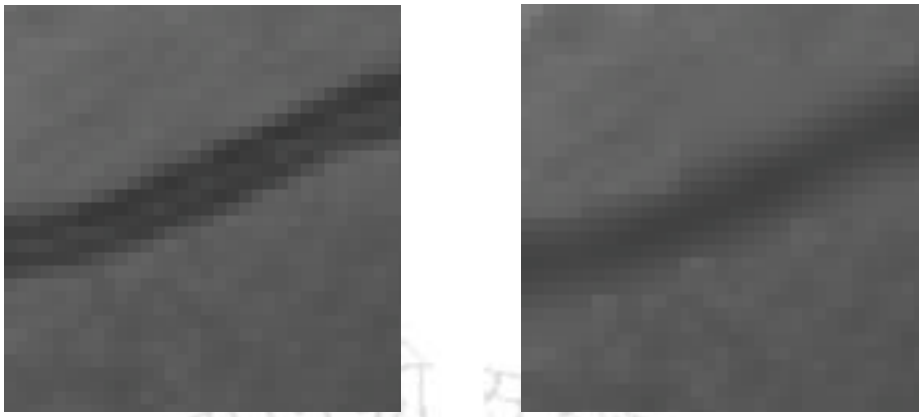

(a) (b)

Figure 4.17: (a) A section of thick vessel (original) (b) Thick vessel after smoothing (reconstructed).

observed that the increased smoothness causes broadening of the profile peak and flattening of the curves. All the distortion measures are computed for each case of smoothing. Then it is investigated which level reflects comparatively more error by showing high distortion value. When this experiment was performed on several retinal images from [98], the obtained result pointed comparatively more error in the L3 subbands, proving that it is due to the distortion in thick vessel. Similar procedure is repeated for some thin vessels also. The thin vessels are altered so that the sharpness gradually reduces and gets blended with the background as shown in the Figure 4.19. Some of the thin vessels in the upper and lower left corner of Figure 4.19(b) shows distortion compared to the original image in Figure 4.19(a). In this case, the error is expected to appear at L2 and L3. Table 4.3 shows the values of proposed $WWDM_v$ and other distortion measures, the wWMSE and wRel WMSE. The last column of table shows that the wRel WMSE and $WWDM_v$ perform in a similar way by having higher distortion values of 2.7776 and 3.4724 respectively. But wWMSE and wRel WMSE show that the total distortion is contributed by all the subbands from L2 to L5. This indicates that the distortion is distributed among these subbands and fails to highlight the distortion in thin blood vessels. The $WWDM_v$ shows a value of 2.2513 in L2 subbands which is significantly higher compared to the distortion

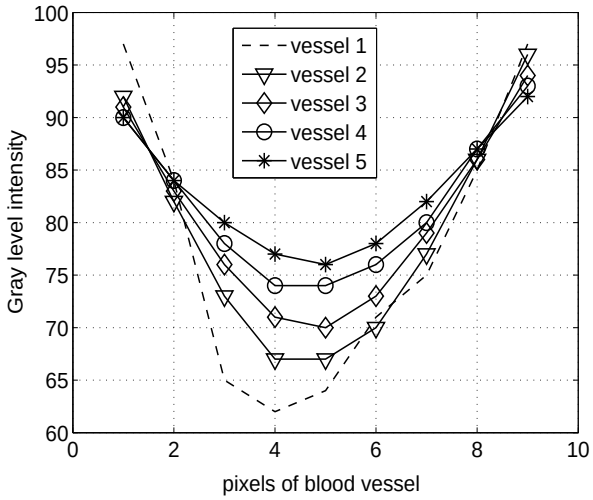

Figure 4.18: The gray level profile(vessel 1) of original vessel. The intensity profile flattens (vessel 2 to vessel 5) for increasing smoothness.

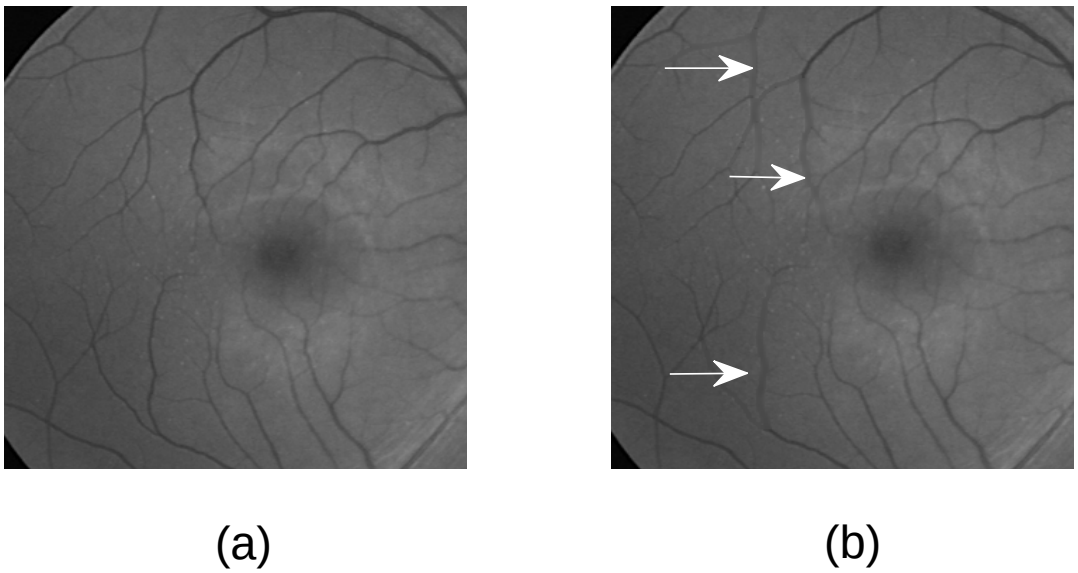

Figure 4.19: (a) Original image (b) image showing distortion in thin vessels.

Table 4.3: Performance of the proposed measure when only thin vessels are distorted

Distortion measure	Distortion computed at each L					Total distortion
	L1	L2	L3	L4	L5	
wWMSE	0.0009	0.1944	0.2500	0.1894	0.1279	0.7627
wRel WMSE (%)	0.0033	0.7079	0.9106	0.6898	0.4659	2.7776
$WWDM_v$ (%)	0.0938	2.2513	0.7880	0.2484	0.0908	3.4724

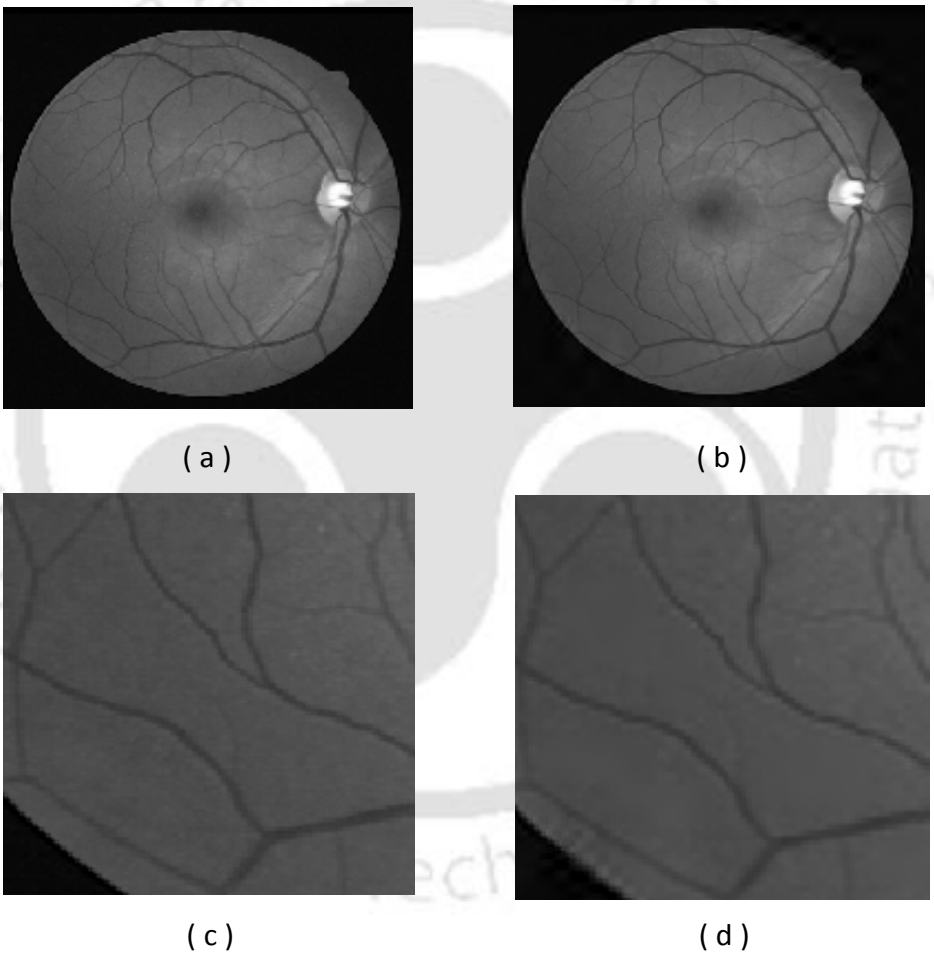

Figure 4.20: (a) Original image, (b) image with distortion in clinically nonsignificant region, (c) clinically nonsignificant region and (d) distortion in clinically nonsignificant region.

value at other levels. This proves that the $WWDM_v$ is a better choice for capturing the distortion in blood vessels.

(iii) Retinal image with distortion in clinically nonsignificant regions

It is observed that the proposed $WWDM_v$ is capable of capturing distortion in blood vessels. The $WWDM_v$ is also required to give less importance to distortion in the regions with no vessels. Such regions are the retinal background regions. To investigate the efficiency of the proposed distortion measure, those regions are distorted by Gaussian smoothing resulting in a reconstructed image. For qualitative verification, the original and the reconstructed images are shown in Figure 4.20(a) and (b). Enlarged sections of nondiagnostic region between the blood vessels are shown in Figure 4.20(c) and Figure 4.20(d). These images show distortion in the nondiagnostic region.

Table 4.4: Distortion in clinically nonsignificant regions

Distortion measure	Distortion measure computed at each L					Total distortion
	L1	L2	L3	L4	L5	
wRel WMSE (%)	0.0334	2.5487	0.8052	0.2326	0.0785	3.6985
$WWDM_v$ (%)	0.0509	0.7927	0.1369	0.0260	0.0064	1.0129
SSIM	-	-	-	-	-	0.9989

Different measures are used to compute the distortion between the original retinal image and the reconstructed image. An efficient distortion measure for blood vessel should effectively evaluate the distortion in blood vessels and ignore the distortion in nondiagnostic regions. Table 4.4 shows the error values obtained using wRel WMSE, $WWDM_v$ and SSIM computed between the original and the reconstructed image. The wRel WMSE shows a high error value of 3.6985 contributed by L2 and L3 subbands. This gives an impression that some blood vessel features are distorted. But the proposed $WWDM_v$ gives low values for all the levels and a small total value of 1.0129. This reflects a small distortion in diagnostically significant features. The same is supported by the image in Figure 4.20(b), which shows that all the blood vessels are well preserved though the image has distortion in clinically nonsignificant regions. From the Table 4.2, it is observed that $WWDM_v$ gives a high value when the second and third level subbands are made

Table 4.5: Performance of the proposed $WWDM_v$ when other features of retinal image are distorted

Distortion in	Distortion computed at each L					Total distortion
	L1	L2	L3	L4	L5	
Thin vessels	0.6306	1.7839	0.5186	0.1487	0.0525	3.1343
Optic disc	0.0344	0.7795	0.3437	0.0998	0.0500	1.3073
Macula region	0.0438	0.9213	0.2521	0.0493	0.0131	1.2797

zero indicating a significant distortion of clinically relevant features. When no diagnostic features are disturbed, the proposed measure shows a low value compared to wRel WMSE as recorded in Table 4.4, suggesting better quality of the retinal image. The better image quality can lead to better diagnosis. The high SSIM index value of 0.9989 points to the good image quality which is true as all the diagnostic features are present as shown in Figure 4.20(b). All these observations suggest that the proposed $WWDM_v$ is efficient enough to catch the significant distortion in blood vessel features and less sensitive to diagnostically nonsignificant distortions.

(iv) Efficacy of the $WWDM_v$ in the presence of distortion in other features

The proposed $WWDM_v$ is evaluated when blood vessel features are not distorted but two other diagnostic features such as the optic disc and macula are distorted. The observations are recorded in the Table 4.5. Selected regions from the optic disc which do not contain any vessel part are distorted with Gaussian smoothing. The $WWDM_v$ reads a small value of 1.3073, whereas for the case of approximately same quantity of distortion in few of the thin vessels results in a $WWDM_v$ of 3.1343. Similarly when the central macula region is distorted to the same level, the $WWDM_v$ shows a low value of 1.2797. All the distorted images are having approximately same MSE. These observations show that $WWDM_v$ is able to capture the distortion in blood vessels more effectively and is less responsive to the distortion in the other features. This is due to the proper weights assigned according to the blood vessel information in the respective subbands.

Table 4.6: Performance of the distortion measure $WWDM_d$ when only OD is distorted

Distortion measure	Distortion computed at each L					Total distortion
	L1	L2	L3	L4	L5	
wWMSE	0.0013	0.7666	5.3470	2.2424	0.1546	8.5120
wRel WMSE (%)	0.0012	0.7102	4.9534	2.0773	0.1432	7.8853
$WWDM_d$ (%)	0.0726	4.6055	6.9015	0.8847	0.1063	12.5707

The proposed $WWDM_v$ shows high error values in appropriate level subbands when the blood vessels are distorted. The $WWDM_v$ indicates low values for the distortion in other retinal features. It was also observed that the measure is less sensitive to the distortion in the nondiagnostic regions. Thus the proposed $WWDM_v$ is more suitable in capturing the distortion in the blood vessels.

4.2.2.2 Evaluation of the distortion measure for the optic disc ($WWDM_d$)

In this subsection, the performance of the $WWDM_d$ is evaluated and compared with that of the other weighted wavelet based distortion measures. The distortion is introduced into the OD region of the image 36_*training* by Gaussian smoothing. All the distortion measures are computed between the original image and the reconstructed image having distortion in the OD. The evaluation and comparison results are shown in Table 4.6. The wWMSE and wRel WMSE show low values of 0.7666 and 0.7102 respectively in the subbands of L2. The proposed measure shows a high value of 4.6055. Similarly, the wWMSE and wRel WMSE show high values of 2.2424 and 2.0773 respectively, at L4 subbands while the proposed $WWDM_d$ shows a low value of 0.8847. The L2 subbands are relatively more significant than L4 subbands for the OD. The wWMSE and wRel WMSE do not reflect the error in the relevant subbands. These comparisons reveal that the proposed distortion measure $WWDM_d$ emphasizes the significant error values at appropriate levels ($L3, L2, L4, L5$ and $L1$) compared to other distortion measures.

The $WWDM_d$ is also evaluated under different cases such as introducing the distortion in (i) other features like thin vessels, thick vessels, (ii) macula region and (iii) clinically nonsignificant

region of the retinal image. All the distorted images considered in the experiment are having approximately the same MSE.

The experimental results obtained are shown in Table 4.7. The first row gives the distortion values when some of the thin vessels are distorted but the OD region is not disturbed. In this situation, the distortion measures are expected to show smaller values. But the wRel WMSE shows a high value of 7.3934. This large error is contributed mainly by the L3 and L2 subbands. These subbands are considered as significant subbands from the OD point of view. This may give a false impression that the OD region is having distortion. The proposed measure $WWDM_d$ shows a comparatively low value of 2.2645. This low value is contributed by L2 subbands which are relatively less significant and thus indicate very little distortion in the OD. The same conclusion holds for the case of distortion in other retinal features such as the thick vessels and the macula. The last row shows the error values when clinically nonsignificant regions are having distortions but the other retinal features are not altered. In retinal images such regions include the smooth retinal background. The distortion measure $WWDM_d$ gives a small value of 1.2932 suggesting very little distortion whereas the wRel WMSE shows a considerably high value of 5.5612.

From the Table 4.6, it is observed that $WWDM_d$ gives a high value when the OD is distorted indicating a significant distortion of clinically relevant feature. When approximately the same amount of distortion is introduced in other diagnostic features, the $WWDM_d$ shows low values compared to wRel WMSE as recorded in Table 4.7. This indicates that the proposed measure emphasizes distortion in the OD. These verifications and comparisons demonstrate that the proposed distortion measure $WWDM_d$ is more suitable to quantify the distortion of the OD in retinal images.

Table 4.7: Performance of the proposed $WWDM_d$ for different cases

Distortion in	wRel WMSE (%)						$WWDM_d$ (%)					
	L1	L2	L3	L4	L5	Total	L1	L2	L3	L4	L5	Total
Thin vessels	0.0064	2.2223	4.2357	0.5548	0.3742	7.3934	0.0276	1.2113	0.9313	0.0689	0.0254	2.2645
Thick vessels	0.0195	2.2060	3.7550	0.8978	0.2152	7.0934	0.0338	0.9398	0.6775	0.0641	0.0136	1.7288
Macula	0.0114	2.6709	5.6649	0.4660	0.2094	9.0226	0.0294	1.0937	0.9456	0.0529	0.0156	2.1373
Clinically nonsig. region	0.0353	2.5069	2.6580	0.2804	0.0806	5.5612	0.0366	0.7520	0.4685	0.0291	0.0071	1.2932

Table 4.8: Performance of the distortion measure $WWDM_m$ when only macula is distorted

Distortion measure	Distortion computed at each L					
	L1	L2	L3	L4	L5	Total
wWMSE	0.0930	1.7450	1.1260	0.3850	0.1210	3.4690
wRel WMSE (%)	0.1437	2.7078	1.7472	0.5978	0.1875	5.3840
$WWDM_m$ (%)	1.7519	3.5441	0.5954	0.1020	0.0222	6.0157

Table 4.9: Performance of the proposed $WWDM_m$ for different cases

Distortion in	Distortion measures (%)	
	wRel WMSE	$WWDM_m$
Thin vessels	6.8572	4.8747
Thick vessels	10.2098	4.2500
Optic disc	8.7909	4.4394
Clinically nonsig. region	10.5892	3.7912

4.2.2.3 Evaluation of the distortion measure for the macula ($WWDM_m$)

The proposed $WWDM_m$ is required to emphasize the distortion in macular region and give less importance to the distortion in other retinal features. In this subsection, the efficacy of the $WWDM_m$ is evaluated. Table 4.8 presents the distortion computed by different measures when the macula is subjected to a distortion of Gaussian smoothing. The wWMSE and wRel WMSE show high values of 1.7450 and 2.7078 respectively in L2 subbands but fail to highlight the next significant error in subbands of L1. They show the next higher values as 1.1260 and 1.7472 respectively, in L3 subbands which are relatively less significant than L1 subbands. The wWMSE and wRel WMSE are unable to follow the diagnostic relevance order of subbands ($L2, L1, L3, L4$ and $L5$) for the macula. The proposed $WWDM_m$ records high values of 3.5441 and 1.7519 in L2 and L1 subbands respectively. The $WWDM_m$ shows a low value in subbands of L3, L4 and L5, satisfying the order of importance. This comparison supports the fact that the proposed distortion measure $WWDM_m$ is more effective in quantifying the macular distortions in a retinal image.

The proposed distortion measure is also examined for its efficiency to consider the distortion

in macula and give less importance to the distortion in other retinal features. The proposed measure is also tested when the distortion is present in the diagnostically nonsignificant regions and other features are not disturbed. The results of this investigation are given in Table 4.9. The entries in the first row give distortion values when a few of the thin vessels are distorted but the macular region is not disturbed. The wRel WMSE shows a high value of 6.8572 supplied by different subbands which are considered as significant from the macula point of view. This may bring a feeling that the macular region is altered which is not the actual situation. The proposed WWDM_{m} results in a considerably low value of 4.8747, indicating a little distortion in the macula. When distortion is introduced in a region which is clinically nonsignificant, the wRel WMSE shows high value of 10.5892 whereas a comparatively low value of 3.7912 is obtained for the WWDM_{m}. All the distorted images used in the test are having approximately the same MSE as that of the macula distorted image. These observations suggest that the proposed distortion measure WWDM_{m} can effectively be used to estimate the distortion of the macular region in retinal images.

4.2.3 Evaluation of the proposed WWDM

The proposed distortion measure WWDM for a retinal image is defined as the linear combination of individual distortion measures as given by Equation (4.1). The distortion measures ($\text{WWDM}_{f}s$) estimate the distortions in the diagnostically important image features. The proposed distortion measure WWDM is required to indicate a high error value when there is distortion in any of the diagnostic features. On the other hand, the distortion measure has to give less importance to the distortion in a clinically nonsignificant regions such as the non-vessel smooth retinal background. The evaluation results are shown in Table 4.10. All the reconstructed images are having the same amount of spatial distortions (MSE≈30%). The WWDM records a high value of 10.974 when the vessel feature is distorted. This total error value is mainly contributed by the WWDM_{v}. The other distortion measures contribute little. The second, third and fourth columns show the performance evaluation of individual distortion measures. The evaluation of WWDM is performed similar to the individual distortion mea-

Table 4.10: Performance of the proposed WWDM

Distortion in	Distortion measures			WWDM
	$WWDM_v$	$WWDM_d$	$WWDM_m$	
Blood vessels	6.046	2.613	2.135	10.794
Optic disc	2.780	6.751	2.064	11.595
Macula	2.558	2.667	6.193	11.418
Clinically nonsig. region	1.727	1.701	1.981	5.409

sures. If the macular region is distorted, then the distortion measure shows a strong response of 11.418. For the same amount of distortion in clinically nonsignificant regions, the WWDM shows a weak response of 5.409. Similarly, for the distortion in OD, the measure is able to capture the error as 11.595. These experimental results prove that the proposed WWDM is a better choice to quantify the clinically significant distortion in processed retinal images.

4.3 Summary

In this chapter, wavelet weighted distortion measures ($WWDM_fs$) are proposed to effectively quantify the loss of diagnostic information. The important information about a retinal feature is captured by some of the wavelet subbands. The proposed $WWDM_fs$ suggest different weights for different subband errors to emphasize the clinically significant errors. The proposed $WWDM_fs$ estimate the distortion in individual diagnostic features and hence performs better in reflecting the diagnostic information loss in retinal images. It is also observed that they all show lower values for the distortion in diagnostically nonsignificant regions. The experimental results demonstrate that the proposed measure is simple and promising for quantifying the distortion in clinically important features in the processed retinal images. In the next chapter, we discuss the performance of the proposed measure in evaluating different types of distortions and comparing it with many of the other existing image quality measures.

5

Performance evaluation of distortion measures

Contents

5.1 Evaluation of image quality measures 128
5.2 Evaluation Results 140
5.3 Summary 147

Wavelet weighted distortion measures for a retinal image were proposed and discussed in the previous chapter. The distortion measures use different weights for different subbands of wavelet decomposition of the retinal images. Such a scheme helps in emphasizing the clinically significant distortions. A global distortion measure (WWDM) was proposed to evaluate the clinical quality of the processed retinal images. The proposed WWDM is expected to correlate closely with the perception of a retinal specialist. This chapter presents the qualitative and quantitative evaluation of the proposed measure in predicting the clinical quality of of the processed retinal images by correlating it with subjective scores. Then the results are compared with many of the other existing image quality measures.

A good objective measure should reflect the distortion introduced in the image due to different types of image processing. Validation is an important step towards successful development of image quality measurement systems. The most standard form of validation is to compare objective quality measures with the ratings by human subjects on a set of distorted images. Section 5.1 deals with the experimental details of the subjective study, objective image quality measures under test and the metrics used for performance evaluation. The results of performance evaluation of distortion measures and their comparison is presented in Section 5.2.

5.1 Evaluation of image quality measures

Since the ultimate users of image processing systems are the humans, a quantitative measure to evaluate the performance of image quality measures is required. The performance of any objective image quality measure is gauged by evaluating its correlation with human visual perception. The subjective studies are carried out to get the subjective scores. After calculating the objective scores for all the distorted images using all the image quality measures, they can be correlated with the MOS using different statistical measures.

There are four widely used metrics to evaluate the performance of image quality measures. The *Pearson linear correlation coefficient* (PLCC) and the *Spearman rank order correlation coefficient* (SROCC) are used to evaluate the correlation between the objective and subjective scores [119]. The other two metrics are the *outlier ratio* (OR) and *root mean square error*

(RMSE) between the actual and predicted subjective scores [120, 121]. The statistical significance test such as *analysis of variance* (ANOVA) is also used to further gauge the performance of image quality measures [122, 123].

5.1.1 Experimental details

This section presents the details of the experiments for subjective study. The details of the reference images used as the original images, the types of distortion used to generate different distorted images, the human subjects involved and the different image quality assessment algorithms used are presented.

Reference images

The reference images (584×565) are derived from the publicly available DRIVE database [98]. Out of forty retinal images, thirty five images are considered as reference images. Five of the images do not show the macula region and are not considered. These images are resized to 512 × 512 using the bicubic interpolation to minimize distortions due to aliasing. All the distorted (test) images are derived from the resized images.

Test images

The test images are created by distorting the reference images using four different types of distortion. In this study, the compression artifacts are generated by two compression algorithms: the discrete cosine transform (DCT) based JPEG [124] and the wavelet based set partitioning in hierarchical trees (SPIHT) [102]. The other types of distortions are the Gaussian blur (Gblur) filters and the addition of white Gaussian noise (WGN) for various values of the standard deviation. The level of distortion is adjusted manually so that the images with minimum to significant distortion are generated.

5.1.1.1 Types of image distortion

Retinal images are degraded by different artifacts such as Gaussian blur, Gaussian noise, JPEG and wavelet based compression methods. Different types of distortion are included to test the ability of objective image quality measures to predict the image quality consistently across distortions. After introducing the distortion, subjective and objective methods are used to

evaluate the image quality. To limit the number of subjective comparisons, only four types of image distortions, commonly encountered in image processing applications are considered in this thesis. The distortion types used to generate different distorted images are as follows.

- JPEG compression: The distorted images are generated by processing the reference images using the JPEG lossy compression. Each of the reference image is compressed with different JPEG Q factors ranging from 10 to 80. The Q factor was varied over a range so that images with a broad range of blocking artifacts, from imperceptible to high levels of impairment are generated.

- Wavelet compression: The distorted images are produced by compression of the reference images using wavelet based image compression method SPIHT [102]. The compression level was varied over a range of quality levels giving images with well preserved clinical information to significant loss of clinical information.

- Gaussian Blur (Gblur): The process of blurring or smoothing the image suppresses noise and small fluctuations. In the frequency domain, this process refers to the suppression of high frequency components of the image signal. The images with this distortion are created by lowpass filtering of the images. A smoothing filter of this kind used in the experiment is, a circular-symmetric 2-D Gaussian kernel of a particular pixel size and standard deviation σ [118]. The smoothing filter is applied to each of the reference images to get the smoothed version of the images. The standard deviation σ of the Gaussian filter is varied such that the images of different quality are generated.

- Addition of white Gaussian Noise (WGN): Noisy images are generated by adding the white Gaussian noise to reference images. The mean and variance of WGN may be varied to generate different levels of noise [118]. The distorted images are obtained by adding noise of different levels to span the range of image quality.

These distortions reflect a wide range of image degradations, from structured to smoothing distortions, image dependent distortions and random noise. The level of distortion was varied

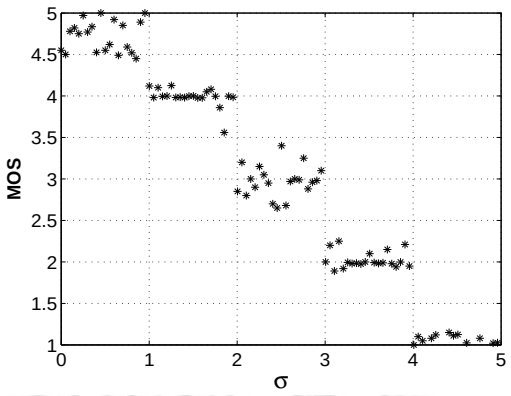

Figure 5.1: Dependance of image quality on distortion parameter σ for Gaussian blur distortion.

to generate images at a broad range of quality, from imperceptible levels to high levels of distortion. Figure 5.1 shows the variation in the subjective quality scores with the distortion strength (σ) for the Gaussian blur distortion. Smaller values of σ indicate, less distortion and higher subjective image quality.

5.1.2 Subjective image quality evaluation

Validation of an image quality measure is important to prove its ability in predicting the images of different quality. It is performed through a subjective evaluation associated with the prediction of perceived image quality by clinical experts. The subjective quality ratings are obtained using a *double stimulus continuous quality scale* (DSCQS) procedure for different distorted images [74, 119]. It is a method to measure the quality of a distorted image relative to a reference image. The continuous scale provides the subject to indicate fine degradations in image quality. This is more convenient for the assessor compared to the five level absolute category rating. The continuous scales are divided into five equal lengths, which correspond to the normal five point quality scale of [74]. The display monitors used to display the images are all 21" monitors set to the same display settings. To maintain constant display conditions across observers, subjects were not allowed to adjust window or level settings or to use the zoom function. The subjective MOS values are obtained from two retinal specialists and thirteen research scholars working in different areas of signal and image processing. All viewers had

normal or corrected to normal visions.

The subjective test is conducted by displaying a pair of images on the screen. The left image is always the original (reference) image without any artifacts and considered to be of excellent quality. The right image is the randomly selected degraded version of the original which possess some difference with respect to original. The assessor is asked to give the score for the second image taking the first image as reference. The absence of defects in the reference part of the presentation pair helps to obtain optimal results. The subject was allowed to take sufficient time to give the score. Once the score was registered, the next pair of images was displayed. The subjects were instructed to score the quality of the distorted image on a scale of 0-100, with 0 being the very bad quality and 100 being the excellent quality. Viewers were aware that the reference image is considered to be of excellent quality and that they should consider it to have a score of 100. A training session was conducted for all the subjects before the experiment. The summary of the training instructions are given in Appendix B. Subjects were shown images in a random order; the randomization was different for each subject. The viewers are allowed to assess without any constraint on viewing distance, time and lighting conditions. After the subject ranked each of the image, the number was converted into a quality score (MOS) by linearly mapping the entire scale to the interval [1, 5]. In this way, the raw quality scores consisted of values in the range 1 to 5.

All the test images (35×4×5=700) were viewed by each subject. The test images are arranged into 35 groups of 20 images. A group of 20 images are viewed by the subjects in a day. To minimize the effects of viewer's fatigue, we conducted the study in two sessions of 30-40 minutes each. The experiment was carried out in a normal hospital and research laboratory environment respectively for the ophthalmic specialists and students. To account for intraobserver differences, each of the image pair (reference and test) was displayed and evaluated twice within the same session. At the end of the day, the difference MOS (DMOS) is computed for each of the distorted image. The DMOS values are generated by taking the difference between the MOS for a reference image and the MOS for the distorted image. The computation of difference scores per session helps to account for any variability in the use of

the quality scale by the viewer between sessions. The evaluation of all the test images was completed in 44 days and some subjects completed in 48 days.

5.1.2.1 Processing of the subjective scores

After obtaining the subjective scores for all the test images from all the viewers, the DMOS scores are computed. The DMOS_{ivt} for the distorted image i is computed by subtracting the quality score q_{ivt} assigned to a distorted image i by the observer v in session t from the quality score of the reference image $q_{i_{ref}}$ in the same session. Thus,

$$\text{DMOS}_{ivt} = q_{i_{ref}} - q_{ivt} \tag{5.1}$$

The true difference score $DMOS_{iv}$ is obtained by taking the average of the scores in the total number of sessions (T).

$$\text{DMOS}_{iv} = \frac{1}{T}\sum_{t=1}^{T} DMOS_{ivt} \tag{5.2}$$

Finally, the DMOS of each of the distorted image i was computed as the mean of the difference score $DMOS_{iv}$ from all the subjects.

$$\text{DMOS}_{i} = \frac{1}{V}\sum_{v=1}^{V} DMOS_{iv} \tag{5.3}$$

where V is the total number of subjects rating the test images.

5.1.3 Objective image quality measures

Over the years, a number of researchers have developed general purpose objective image quality assessment algorithms [120, 125]. The various objective image quality measures investigated in this work are listed in Table 5.1. The implementations of the algorithms were either freely available for download or done by ourselves based on the information available in the papers. The table gives the image quality assessment algorithms belonging to different classes. These measures are described in Chapter 2. For better reference, some of these are outlined here. The traditional pixel difference based global quality measures include the MSE and PSNR. A lower value of MSE or a higher PSNR value indicates lesser error. This should correlate to a

Table 5.1: Image quality assessment (IQA) algorithms under test

IQA Algorithms	Comment
MSE	Pixel difference based
PSNR	Function of MSE
SSIM	[45]
MS-SSIM	[84]
VSNR	[85]
IFC	[47]
VIF	[46]
WIQM	[86]
WWDM	Proposed

higher quality image. But tests have shown that this is not always the case [45, 75, 126]. The performance of the objective measures can be improved by incorporating the properties of HVS. The following structural based and information theoretic based measures use the properties of HVS in the image quality evaluation.

The structural information based measures are the SSIM index and the MS-SSIM index. The SSIM index is based on the assumption that the HVS is highly adapted to extract structural information from natural images [45]. It is based on the degradation of structural information. The SSIM index is based on high-level properties of the HVS, but employ no explicit model of the HVS. The SSIM attempts to measure the changes in luminance, contrast, and structure in an image. It is computed locally and then averaged to obtain a single mean SSIM value [127]. The MS-SSIM is an extension of the SSIM and calculates multiple SSIM values at multiple image scales (resolutions). Since MS-SSIM accommodates for different viewing distance conditions, it has been shown to increase the correlation between the MS-SSIM index and subjective quality tests [84]. However, the trade-off is that MS-SSIM takes a longer time to run than the straight SSIM algorithm. The SSIM and MS-SSIM take 1 for perfect similarity and 0 for no similarity.

The IFC and VIF are information theoretic based measures. They compute the mutual information between the wavelet subbands of the original and the distorted images. The IFC ranges from zero to infinity as VIF values lies between zero and one for complete information loss and no information loss respectively [128].

In recent years several image quality assessment methods in the wavelet domain have appeared in the literature. Wavelet transform provides an alternative representation of image data that closely approximates the space frequency decomposition of the HVS.

The VSNR operates for both near-threshold and supra-threshold distortions via two stages. It incorporates an improved HVS model and hence performs better in predicting the image quality [85, 129]. A higher VSNR indicates little distortion in the image.

The new WIQM based on wavelets uses the Watsons model to treat the distortion in different subbands. The subbands errors are weighted with experimentally determined perceptual weights. We have implemented the algorithm by decomposing the images to three levels and using the weights mentioned in [86].

The proposed WWDM is also used for quantifying the degradation in the processed retinal images.

5.1.4 Evaluation metrics

The objective measures may not correlate linearly with the MOS. Hence before calculating the correlation, the objective measures obtained from image quality metrics are passed through a nonlinear transformation function. A nonlinear logistic function is used to transform the set of objective measure values to a set of predicted DMOS ($\mathrm{DMOS_P}$) values [119]. This removes any nonlinearity due to the subjective rating process and facilitates comparison of all the measures in a common analysis space. The 4-parameter and 5-parameter logistic function was initially suggested by video quality experts group (VQEG) but found to be complex and failed to converge. The following three parameter logistic function was recommended by the VQEG to fit the objective data to the subjective data. Though this function is slightly less accurate, it was found to be converging for all the sets of data [119].

$$\mathrm{DMOS_P} = \frac{\beta_1}{(1 + exp^{-\beta_2(M-\beta_3)})} \tag{5.4}$$

where M is the objective score and β_1, β_2 and β_3 are the model parameters.

The graph of a general logistic curve is shown in Figure 5.2. Changing the values of the

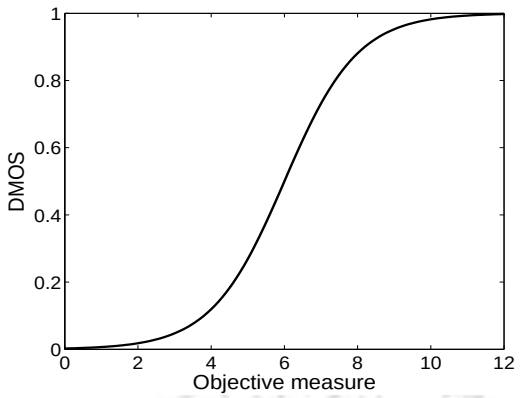

Figure 5.2: A general logistic curve.

parameters stretches or shrinks the axes and changes the rate at which the curve varies from its lower value to its maximum value. The initial values of the parameters can be selected from the data to be fitted. The parameter β_1 may be initialized to the maximum value of the objective data. β_2 controls the curve transitions from the lower value to the upper value and therefore may be initialized with the slope or growth rate of the curve. β_3 may be initialized to the minimum value of the objective data to be fitted. The nonlinear least squares optimization is used to find the optimal parameters. The logistic fitting is done by using the optimal parameters that minimize the square error between the subjective DMOS values and the objective scores M. After applying the nonlinear regression to the objective measures, the prediction performance of the objective image quality measures is evaluated by computing various metrics on the actual DMOS and the DMOS_P.

The performance of the objective measures (models) is evaluated with respect to different aspects of their ability to estimate subjective assessment of image quality [119]. They are,

- Prediction accuracy

  Prediction accuracy is the ability of a model to predict the subjective quality ratings with low error. The evaluation metric related to prediction accuracy of a model is the PLCC.

The PLCC of an objective quality measure M with respect to DMOS is calculated as,

$$\text{PLCC} = \frac{\sum_{i=1}^{S}(M_i - \overline{M})(DMOS_i - \overline{DMOS})}{\sqrt{\sum_{i=1}^{S}(M_i - \overline{M})^2 \sum_{i=1}^{S}(DMOS - \overline{DMOS})^2}} \tag{5.5}$$

where M_i and $DMOS_i$ are the sample values, $\overline{M}$ and $\overline{DMOS}$ are the corresponding sample means of M and DMOS respectively and S is the total number of tested images. The PLCC reflects the degree of linear relationship between two variables and varies from -1 to 1. A value of 0 implies that there is no linear correlation between the variables. A value of $\pm$ 1 implies that there is a highest linear correlation between the variables.

The PLCC after non-linear fitting is computed in a similar way but between the actual DMOS and the DMOS_P. The larger is the PLCC value, the better is the accuracy of the objective measure.

- Prediction monotonicity

  Prediction monotonicity is the degree to which the objective model's predictions agree with the subjective quality ratings. The metric related to prediction monotonicity of a model is the SROCC. The SROCC uses the ranking of the data rather than the actual data. The position of the data point in an ordered list from the minimum to maximum values gives the rank value. The SROCC is computed as [119]

$$\text{SROCC} = 1 - \frac{6\sum_{i=1}^{S}(r_i)^2}{S(S^2-1)} \tag{5.6}$$

  where r_i is the difference between i^{th} rank of the corresponding pair of objective measure and DMOS. This correlation value is computed after nonlinear fitting considering the rank of DMOS and DMOS_P. The larger is the the SROCC, the better the monotonicity of the objective image quality measure.

- Prediction consistency

  Prediction consistency is the degree to which the model is robust with respect to a variety

of image artifacts. The metric related to prediction consistency of a model is the OR. An outlier is defined as a data point for which the prediction error is greater than a certain threshold. In the present work, twice the value of standard deviation of the prediction error was used as the threshold for defining an outlier point [119]. So the outlier points are the points which lie outside the interval $[DMOS - 2\sigma,\ \ DMOS + 2\sigma]$. The OR is defined as the number of outlier-points (s_o) to the total number of data points S,

$$\text{OR} = \frac{s_o}{S} \tag{5.7}$$

- Prediction efficiency

  The prediction efficiency is evaluated using the RMSE. The RMSE gives the root of the mean squared error between the actual DMOS and the DMOS_P. It indicates the statistical distance between the subjective scores and calculated as

$$\text{RMSE} = \sqrt{\frac{\sum_{i=1}^{S} (DMOS(i) - DMOS_p(i))^2}{S}} \tag{5.8}$$

  The lower value of RMSE indicates better performance of the objective image quality measure.

5.1.5 Analysis of variance and F-ratio

The ANOVA is a statistical tool that can be used to compare the differences among image quality measures [119, 122, 130, 131]. It provides a supplementary metric which can be used to evaluate the prediction accuracy of an objective measure. The use of ANOVA is to identify those image quality measures that are more consistent and discriminative of the distortion artifacts due to compression, blur and noise [123]. The ANOVA compares the means of several groups of observations by using estimates of variances of the groups.

In the present context, the purpose of a one-way ANOVA is to find out whether data from several quality groups have a common mean. Each distortion factor, for eg. compression, consists of different objective quality scores obtained from S distorted (compressed) images.

These are grouped into Q_G number of quality groups corresponding to different visual quality of the test images. Each group has S_G number of sample data points. These quality groups are treated as the columns of the ANOVA data matrix A.

The hypotheses for the comparison of the independent groups are as follows:

Suppose μ_g, for g=1,2,..,Q_G are the means of the quality groups, then the null hypothesis H_0 is given by

$H_0 : \mu_g = \mu_h$, for $g \neq h$.

The alternate hypothesis is that at least one of the means is different. Thus

$H_A : \mu_g \neq \mu_h$, for at least one $g \neq h$.

In an ANOVA, the *F-ratio* is the statistic used to test the null hypothesis that the means of several groups of observations are significantly different from one another. The ANOVA computes the F-ratio by dividing the variability of the data into two parts:

- Variability due to the differences among the column means (variability between groups)

  This factor shows how much, the group means vary from the overall mean.

- Variability due to the differences between the data in each column and the column mean (variability within groups)

  This factor shows how much, the groups vary about their own means.

The within group variance is calculated as the sum of squares (SS) of the residuals divided by degrees of freedom DF_{ss}. It is calculated as,

$$\mathrm{SS} = \sum_{g=1}^{Q_G} \sum_{i=1}^{S_G} (s_{g,i} - \mu_g)^2 \tag{5.9}$$

where $s_{g,i}$ is a sample from the g^{th} group, S_G is the total number of samples in that group and μ_g is the mean of the group g. Then $\mathrm{DF_{ss}} = \mathrm{S} - \mathrm{Q_G}$.

The between group variance is calculated as the sum of squares of the means (MS) divided by

degrees of freedom DF_{ms}. It is calculated as,

$$\mathrm{MS} = \sum_{g=1}^{Q_G} (\mu_g - \bar{\bar{\mu}})^2 \tag{5.10}$$

where $\bar{\bar{\mu}}$ is the mean of all the group means (μ_g). Then $\mathrm{DF_{ms}} = \mathrm{Q_G}$ - 1.

Then the F-ratio is calculated as,

$$\text{F-ratio} = \frac{between\ \ group\ \ variance}{within\ \ group\ \ variance}$$

$$\text{F-ratio} = \frac{MS/DF_{ms}}{SS/DF_{ss}} \tag{5.11}$$

A high value of F-ratio indicates the evidence to reject the null hypothesis in favor of the alternative.

Similarly for other distortion cases, blur groups were created by lowpass filtering the images and noise groups were created by adding white Gaussian noise to all the images. The ANOVA is applied separately on blur groups and noise groups.

5.2 Evaluation Results

The effectiveness of objective image quality measures is evaluated by correlating them against subjective quality scores. The performance of the objective image quality measures is tested by using the evaluation metrics. Additionally, the ANOVA is also used to assess the effect of different degradation on the performance of objective quality measures. In this section we present results on validation of the WWDM and comparisons with other quality measures.

5.2.1 Performance evaluation using the metrics

The objective scores given by different quality measures and the subjective scores given by the subjects are used to evaluate the performance of the objective measures. Nine quality measures listed in Table 5.1 were applied to quantify the distortion in retinal images. The logistic function defined in Equation (5.4) is used in the fitting procedure to provide a nonlinear mapping between the objective and subjective scores. The scatter plots for various objective measures along with

the best-fitted logistic regression curve are shown in Figure 5.3. The scatter plots can be used as a visual check on correlation between the two measures. Each data point in the scatter plot represents one distorted image. If the data points are clustered densely around the fitted line, then it implies the better consistency between subjective and objective quality evaluations. The scatter plots shown in Figure 5.3 are only for the SPIHT compression type of distortion.

The scatter plots of MSE, PSNR, SSIM and MS-SSIM show widely spread data points indicating a lower correlation with the subjective score. The scatter plots of IFC, VIF and VSNR measures show less spread data points and improved correlation. By comparing the scatter plots of all the measures, it is observed that the proposed WWDM possess a compact scatter plot with all the data points lying within a small range. This implies that the proposed WWDM provides better quality estimation and is more consistent with the subjective scores as compared to the other measures.

After the nonlinear curve fitting process, different metrics are used to compute the correlation between the objective and the subjective scores. The performance of all objective quality measures in terms of the PLCC, the SROCC, the RMSE and the OR metrics after nonlinear regression are shown in Table 5.2 - Table5.5. All the measures are evaluated for each distortion type and for the entire dataset. Different measures respond with differing sensitivities to artifacts and distortions.

The PLCC values computed for all the measures and for different type of distortions are presented in Table 5.2. It is observed that the WWDM performs well compared to other measures. The WWDM shows higher correlation values for different distortions. The global measures MSE, PSNR and the WIQM are unable to capture the loss of clinical information in distorted retinal images. Hence they show lower correlation values for all distortion conditions. The SSIM index and MS-SSIM index show improved performance as compared to the MSE PSNR and the WIQM. These measures make use of the local structural information to compute the total distortion value. This may improve the prediction of image quality and correlation with the subjective score. The VIF and IFC perform better compared to the SSIM and the MS-SSIM for compression, blur and noise distortions. The VSNR shows better correlation as

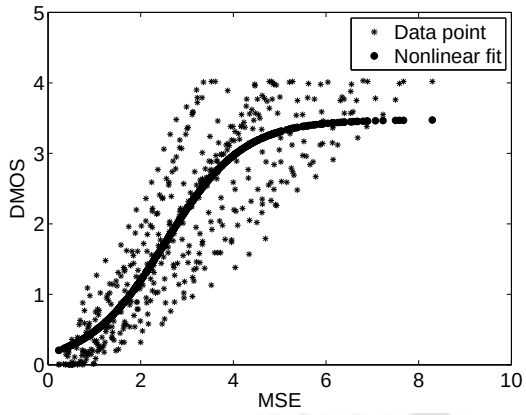

(a)

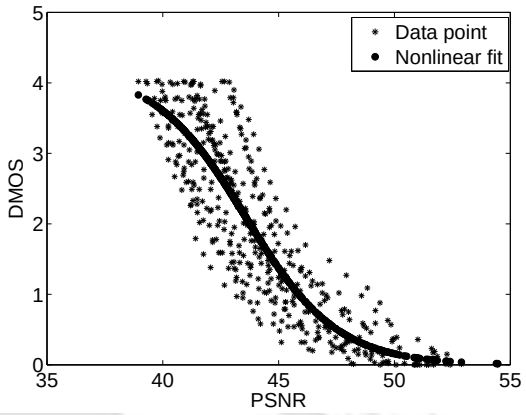

(b)

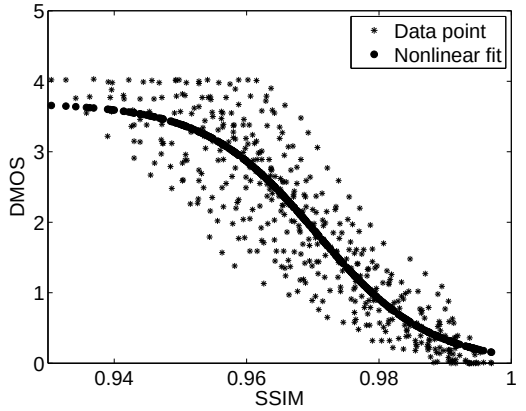

(c)

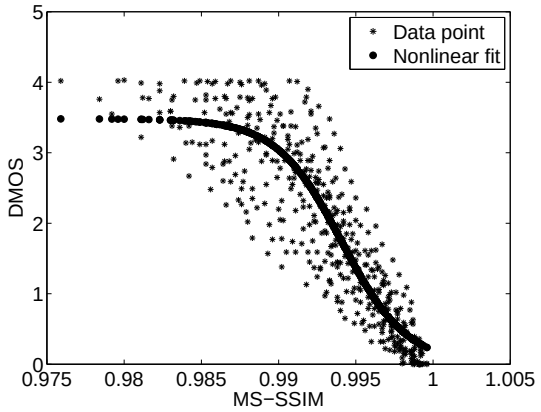

(d)

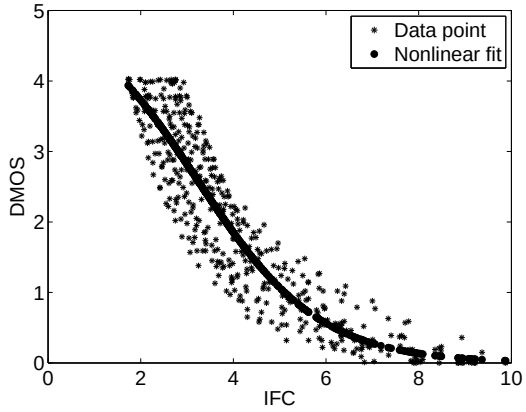

(e)

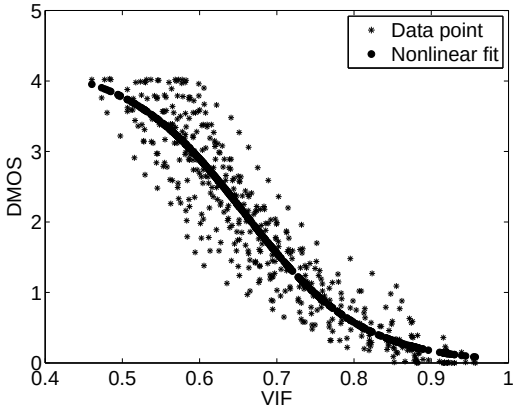

(f)

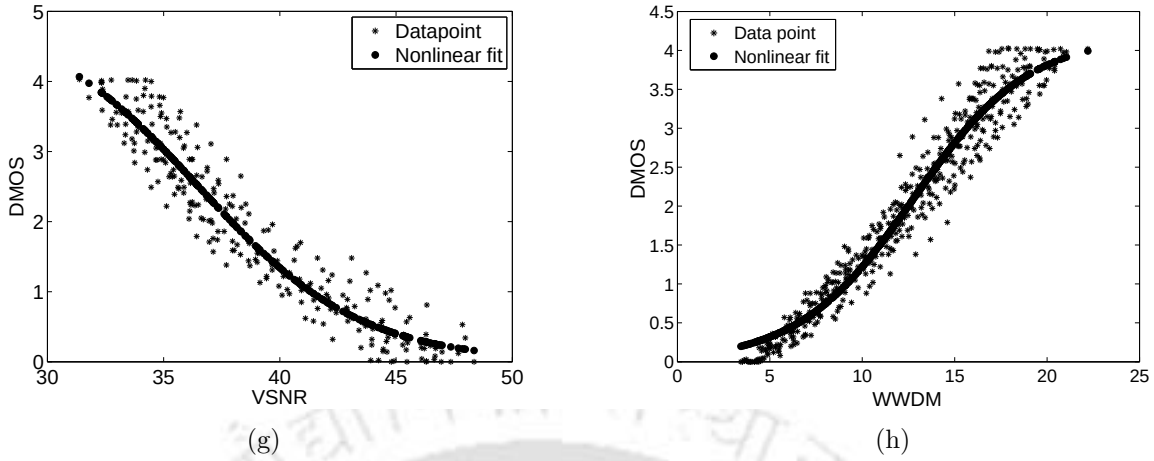

Figure 5.3: Scatter plots showing the nonlinear fit using the logistic function for the a) MSE (b) PSNR (c) SSIM (d) MS-SSIM (e) IFC (f) VIF (g) VSNR and (h) WWDM versus DMOS. Each data point represents one distorted image.

compared to the IFC and VIF. The low level and mid level visual properties of the HVS are used in the implementation of VSNR which makes it to perform better in evaluating the image quality. For the case of Gaussian blur, the performance of IFC and VIF is close to that of the proposed WWDM. The distortion model considered in these measures capture the loss of signal energy due to blur effectively.

Table 5.3 shows the SROCC values between each of the measures and DMOS. The observations are similar to those for the PLCC. The MSE, PSNR and the WIQM show lower correlation values for different distortion conditions. The SSIM and MS-SSIM show slightly improved correlation values. The MS-SSIM index performs better than SSIM index in capturing the blocking and blur artifacts. The VIF and IFC show better correlation compared to the SSIM and the MS-SSIM for all distortions. The proposed WWDM performs much better than the rest of the measures. It is observed that the VSNR is comparable with the proposed WWDM. But for the blur artifacts, the IFC and VIF perform better than VSNR. The different measures are ranked from highest to lowest according to their correlation with the subjective scores for different distortion as follows:

JPEG - WWDM, VSNR, IFC, VIF, MS-SSIM, SSIM, WIQM, MSE and PSNR,

SPIHT - WWDM, VSNR, VIF, IFC, MS-SSIM, SSIM, WIQM, MSE and PSNR,

Gblur - WWDM, IFC, VIF, VSNR, MS-SSIM, SSIM, WIQM, MSE and PSNR and
WGN - WWDM, VSNR, IFC, VIF, MS-SSIM, SSIM, MSE, PSNR and WIQM.

Table 5.4 shows the RMSE values computed after nonlinear fitting, for all the objective measures. The RMSE shows the relative improvement of one image quality measure over the another. For a better objective measure, the RMSE should be smaller. The proposed WWDM shows lower RMSE values in all the distortion cases and hence performs best in the group. The MSE, PSNR and WIQM are less sensitive to different distortions and show higher RMSE values. The SSIM index and MS-SSIM index show improved performance. The IFC and VIF show lower RMSE values and better than the structural based SSIM and MS-SSIM indices. They show better performance in evaluating the blur distortion with lower RMSE value as compared to the VSNR. In this case their performance is close to the best performing WWDM. For compression artifacts (JPEG and SPIHT) and Gaussian noise distortion, the VSNR gives the second best result. The different measures are ranked from highest to lowest according to their sensitivity to different artifacts as follows:
JPEG - WWDM, VSNR, IFC, VIF, MS-SSIM, SSIM, WIQM, PSNR and MSE,
SPIHT - WWDM, VSNR, VIF, IFC, SSIM, MS-SSIM, WIQM, PSNR and MSE,
Gblur - WWDM, IFC, VIF, VSNR, MS-SSIM, SSIM, WIQM, PSNR and MSE and
WGN - WWDM, VSNR, IFC, VIF, SSIM, MS-SSIM, PSNR, MSE and WIQM.

The OR values computed for each of the measure and for different types of distortions are listed in Table 5.5. It is observed that the proposed WWDM shows less number of outlier data points compared to other measures for different types of distortions. From the remaining set of measures, the VSNR shows few outlier data points. Then VIF and IFC measures are better as compared to the VSNR. The WIQM shows fewer outlier points for the case of SPIHT and blur distortion. The similarity measures SSIM index and MS-SSIM index show more outlier data points when compared to the VIF and IFC, whereas the MSE and PSNR are having more number of outliers among all the measures.

The results in the four tables demonstrate that the MSE, PSNR and WIQM have limitations in quantifying the distortion in retinal images. The IFC and VIF show improved performance

Table 5.2: Pearson linear correlation coefficient(PLCC) after nonlinear regression

Measures / Distortion	MSE	PSNR	SSIM	MS-SSIM	VSNR	IFC	VIF	WIQM	WWDM
JPEG	0.8653	0.8746	0.9028	0.9051	0.9567	0.9414	0.9334	0.8890	0.9604
SPIHT	0.8714	0.8744	0.8932	0.8911	0.9441	0.9143	0.9199	0.8818	0.9662
Gblur	0.8456	0.8628	0.9401	0.9415	0.9505	0.9690	0.9663	0.8770	0.9695
WGN	0.8354	0.8490	0.8623	0.8601	0.9475	0.9252	0.9203	0.8296	0.9720

Table 5.3: Spearman rank order correlation coefficient(SROCC) after nonlinear regression

Measures / Distortion	MSE	PSNR	SSIM	MS-SSIM	VSNR	IFC	VIF	WIQM	WWDM
JPEG	0.8754	0.8754	0.9087	0.9211	0.9592	0.9423	0.9360	0.9036	0.9697
SPIHT	0.8737	0.8737	0.8942	0.8943	0.9434	0.9155	0.9210	0.8876	0.9659
Gblur	0.8663	0.8663	0.9481	0.9549	0.9590	0.9721	0.9703	0.9034	0.9756
WGN	0.8511	0.8511	0.8659	0.8684	0.9505	0.9282	0.9217	0.8471	0.9766

compared to the SSIM and the VSNR. The WWDM performs better in terms of PLCC, SROCC, RMSE and OR than all the other quality measures tested in this work. Hence the WWDM can be considered as a better measure to quantify the clinically significant distortion in retinal images.

The overall prediction performance of the evaluated image quality measures based on the SROCC and PLCC is illustrated in Figure 5.4. The WWDM shows higher values of these parameters consistently for all types of distortion. Some of the other measures shown in figure exhibit varying sensitivity to different types of artifacts. It is evident from the plot that the proposed WWDM performs better when compared with other objective measures.

5.2.2 Performance evaluation using the ANOVA

The performance of image quality measures is also evaluated in terms of how discriminating they are to distortion artifacts when tested on a variety of images using the ANOVA method. The F-ratio values are obtained by performing the one-way ANOVA. The results of ANOVA for

Table 5.4: Root mean squared error (RMSE) after nonlinear regression

Measures / Distortion	MSE	PSNR	SSIM	MS-SSIM	VSNR	IFC	VIF	WIQM	WWDM
JPEG	0.6247	0.6051	0.5358	0.5302	0.3646	0.4208	0.4475	0.5705	0.3502
SPIHT	0.6038	0.5976	0.5537	0.5591	0.4048	0.4989	0.4831	0.5822	0.3173
Gblur	0.6305	0.5980	0.4022	0.3980	0.3666	0.2922	0.3037	0.5671	0.2896
WGN	0.6786	0.6526	0.6252	0.6298	0.3952	0.4690	0.4830	0.6894	0.2929

Table 5.5: Outlier ratio (OR) after nonlinear regression

Measures / Distortion	MSE	PSNR	SSIM	MS-SSIM	VSNR	IFC	VIF	WIQM	WWDM
JPEG	0.0597	0.0622	0.0597	0.0522	0.0448	0.0522	0.0522	0.0473	0.0398
SPIHT	0.1454	0.1498	0.1406	0.1410	0.1420	0.1586	0.1476	0.1388	0.1167
Gblur	0.0441	0.0559	0.0618	0.0500	0.0676	0.0471	0.0618	0.0471	0.0265
WGN	0.0446	0.0462	0.0420	0.0394	0.0446	0.0499	0.0391	0.0472	0.0367

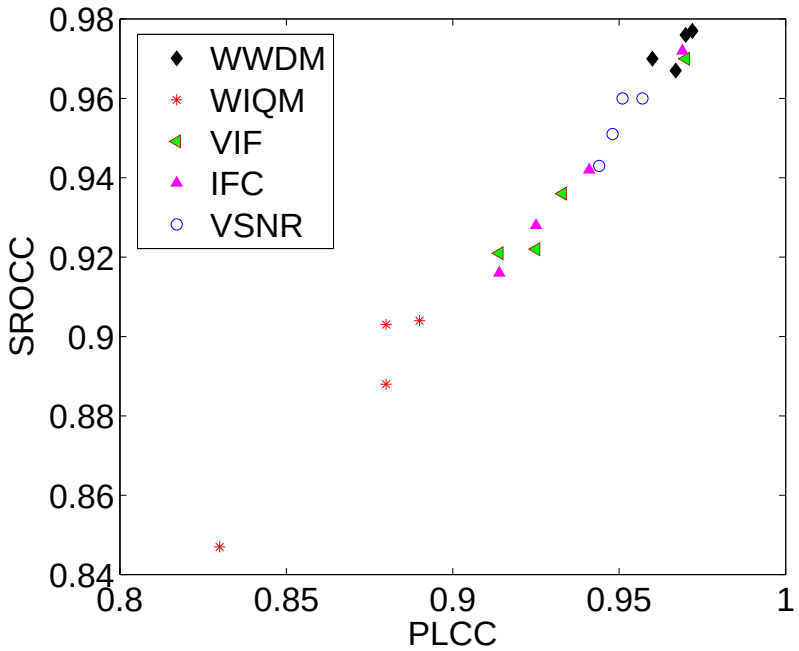

Figure 5.4: Prediction performance of the objective quality measures.

Table 5.6: ANOVA results (F-scores) for all the measures and for different distortions

Measures/ Distortion	MSE	PSNR	SSIM	MS-SSIM	VSNR	IFC	VIF	WIQM	WWDM
SPIHT	78	89	108	93	224	102	136	72	362
JPEG	65	124	102	86	421	210	273	62	860
Gblur	59	97	69	75	412	151	340	57	589
WGN	53	91	84	98	367	193	289	64	624

all the image quality measures and for different distortions are listed in Table 5.6. The larger value of the F-ratio indicates that the means of all the groups of observations are significantly different and there will be minimum overlap between the two or more groups. This indicates that the image quality measure can distinguish the different quality images well and close to the subjective evaluations. From the Table 5.6, it observed that the MSE and WIQM show lower F-ratio value for all the distortion types. This indicates large amount of overlapping between quality groups. They are considered as poor measures and less responsive to different distortions. The PSNR performs better than MSE and WIQM. The SSIM index and the MS-SSIM perform better than PSNR for the SPIHT compression distortion but their performance is poor for other distortions. The IFC and VIF measures respond strongly to all distortions compared to PSNR and SSIM index. The VSNR performs better compared to all these measures and the WWDM performs best among the group. It is observed that the WWDM has the highest F-ratio values among all other image quality measures. This shows that, it is consistent and more close to the subjective evaluations. With all these observations, different measures can be ranked according to their sensitivity to different distortions, in the ascending order as WIQM, MSE, SSIM, MS-SSIM, PSNR, IFC, VIF, VSNR and WWDM. Thus the WWDM performs well in predicting the quality of distorted retinal images.

5.3 Summary

The performance evaluation of a number of image quality measures is presented in this chapter. The study was made considering four types of distortion applied to 35 reference images

to generate different visual quality images to cover the complete range of MOS. Various popular objective image quality measures were evaluated to assess their correlation with human perception. The WWDM can be considered as an effective measure for quality assessment of digital retinal images which agrees well with evaluations made by the human observers. The proposed measure provides better prediction accuracy (higher PLCC), better prediction monotonicity (higher SROCC) and better prediction consistency (lower OR) than the other most widely used quality measures in the image processing literature. The proposed WWDM shows lower RMSE between the actual MOS and the predicted MOS. The analysis by ANOVA shows higher F-ratio values for the WWDM indicating that it can distinguish the different quality images well and hence consistent with the subjective scores. The WWDM is easy to compute and more responsive to clinically significant distortions in retinal images.

6

Conclusions

Contents

6.1 Scope for the Future Work 153

In this thesis, new wavelet weighted distortion measures to quantify the clinical information loss in processed retinal images are investigated. Retinal images have the potential to facilitate the early detection of retinal pathologies. The ophthalmologists examine the clinically important features for signs of various eye related diseases. The retinal image should be of sufficient quality to ensure reliable diagnosis. The retinal images need to be processed for efficient storage and transmission. Any such processing causes distortion and degrades the image quality. It is expected that little distortion occurs to the clinically important features. The image quality measure is expected to emphasize any distortion in clinically important regions and give less importance to the effects in nondiagnostic regions. In this research work, the spatial frequency localization and MRA properties of the DWT are explored for localizing the retinal image features. Different wavelet subbands obtained by wavelet decomposition of a retinal image, are investigated for the presence of information about the clinically important features. The weight values for the subbands are computed according to their clinical importance. Then the distortion measure for each feature is defined in the wavelet domain. The work in this thesis can be summarized as follows:

In **Chapter 1**, retinal image, its components and their clinical importance are discussed. The literature survey on the analysis of clinically important features of a retinal image - the optic disc (OD), the macula and the blood vessels are also presented. The study and analysis of different methods to detect the abnormalities such as microaneurysms, haemorrhages and exudates are also presented.

In **Chapter 2**, the literature review on retinal image quality and related methods in quality analysis are presented. The literature on processing of retinal images and evaluating the image quality for diagnosing particular diseases is also discussed. Though many approaches and algorithms have been reported in the literature, it was found that they focussed on evaluating the quality of an individual retinal photograph. Estimating the image quality from the point of view of diagnostic information loss was not addressed. This gave us the motivation to define a diagnostically meaningful distortion measure for the processed retinal images.

In **Chapter 3**, the analysis of retinal image information in different wavelet subbands is

carried out. The retinal image is decomposed into different subbands using the DWT, each of them containing information at a specific frequency and along a specific direction. The advantage of using the wavelet transform in image processing is that, the image features can be well localized. The experimental observations show that out of many subbands only certain subbands carry discriminating information about different retinal features. From the point of view of blood vessels, the L2 subbands have information about the thin vessels and important compared to other level subbands. The L3 subbands represent the thick vessels. The L1, L4 and L5 carry minimum information about the blood vessel structure. The subbands are ranked according the vessel information content, in the descending order as $L2, L3, L4, L5$ and $L1$. Similar experiments conducted for the optic disc resulted in the diagnostic relevance order of $L3, L2, L4, L5$ and $L1$. For the macula feature, the relative significance order of the subbands is $L2, L1, L3, L4$ and $L5$. All these observations are quantified by computing the SSIM index between the original and the processed retinal images. The observations obtained from this analysis are utilized to develop a new method for the segmentation of blood vessels. The method is fast and easy to implement.

In **Chapter 4**, the results of the above investigations are used to propose distortion measures which can treat different subband error differently. The proposed distortion measures suggest different weights for different subband errors to emphasize the loss of clinically significant information. The wavelet weighted distortion measure $WWDM_f$ is defined for each of the retinal feature f. A global distortion measure WWDM is defined by combining the individual distortion measures. The proposed distortion measures are evaluated under the distortion in clinically nonsignificant regions and in other retinal features. The experimental results demonstrate that the proposed WWDM is more suitable to quantify the distortion in clinically important features. It is simple and promising for evaluating the clinical quality of the processed retinal images.

Chapter 5 presents the qualitative and quantitative evaluation of the proposed WWDM. The performance of the WWDM is compared with various other image quality measures by applying them on distorted retinal images. The investigation was made by considering different

types of distortion applied to reference images to generate different visual quality images. These distorted images are then evaluated qualitatively by human subjects and quantitatively by different image quality measures. The performance is evaluated to assess the correlation of the objective measures with human perception. Various statistical metrics such as the PLCC, the SROCC, the OR and the RMSE are used for evaluating the image quality measures. The ANOVA method is also used to assess the objective measures in discriminating the different artifacts.

The proposed WWDM shows better prediction accuracy (higher PLCC), better prediction monotonicity (higher SROCC), better prediction consistency (lower OR) and lower RMSE compared to other most widely used image quality measures reported in the image processing literature. The WWDM is simple to compute and more effective to quantify the clinically significant distortions in processed retinal images.

The major contributions of the work reported in this thesis include the following:

(1) The analysis of clinical feature information in different wavelet subbands of a retinal image is carried out.

(2) A subband weighted distortion measure for the assessment of clinical quality of the retinal images is proposed by linearly combining the wavelet weighted individual distortion measures for the blood vessels, the OD and the macula features.

(3) The performance of the WWDM is evaluated by correlating with the subjective scores and compared with various other image quality measures by applying them on degraded retinal images.

The other contributions are,

(i) A comparative study of a set of wavelet filters to select the optimum decomposition level and the appropriate wavelet filter for retinal image analysis.

(ii) The blood vessel information in different subbands is used to propose a new method for blood vessel segmentation.

6.1 Scope for the Future Work

The thesis points to some interesting future work.

- The WWDM needs to be evaluated on a larger database and also on pathological images. Then it may be used for diagnostic decision purpose.

- Distortion constrained retinal image compression using WWDM-

  The compression of images results in a trade-off between the compression ratio and the quality. This is an important issue in telemedicine. The WWDM may be used to optimize the trade-off. The WWDM may provide a way for compressing images so that the loss of information complies with user defined distortion requirements.

- Retinal image matching in biometric applications-

  Retinal image matching is used for person identification in biometric security applications. The retinal features are unique to each individual. The WWDM may be used to compute the disparity of the image features and to find the best matched retinal image pair.

- The WWDM may be used as a similarity measure for retinal image registration-

  The registration methods require the evaluation of similarity between images. In this direction, the similarity between different clinical components may be tested using the $WWDM_f$s.

- The longitudinal study of retinal images-

  The proposed WWDM may be used as a measure for quantitative assessment of longitudinal changes in the patients retinal images. This study is useful for automated analysis of therapy effects and pathology progression.

A

Retinal images under pathological conditions

Contents

A.1 Pathological retinal images 156

The retina is a layered tissue lining the interior of the eye that enables the conversion of incoming light into a neural signal that is suitable for further processing in the brain. The important clinical components of the retina and their clinical importance are described in the introduction Chapter. Ophthalmologists use these retinal images to diagnose the retinal diseases.

A.1 Pathological retinal images

Many important diseases manifest themselves in the retina and originate either in the eye or in the cardiovascular system. A brief description of the most prevalent diseases that can be studied via retinal imaging is given below.

Diabetic Retinopathy

Diabetic retinopathy (DR) is a complication of diabetes and the most common cause of visual loss. Diabetic retinopathy affects the small blood vessels in the retina. The blood vessels may be damaged by diabetes reducing the nourishment to the retina. In this condition, new, fragile blood vessels develop on the surface of the retina. These abnormal blood vessels can break and bleed over the surface of the retina leading to microaneurysms (MAs) and hemorrhages as shown in Figure A.1.

Age-Related Macular Degeneration

Age-related macular degeneration (ARMD) is the leading cause of blindness in people over 50 years of age. It is caused by the damage to the macula. One of the symptoms of ARMD is the presence of fatty deposits called drusen, on the retina. The presence of drusen may be identified through inspection of retina images as shown in Figure A.2. Because of ARMD, the property of the macula for seeing fine details and color will be lost.

Glaucoma

Glaucoma is a disease in which fluid pressure within the eye rises. There is a small space in the front side of the eye called the anterior chamber. Clear liquid flows in and out of this chamber. This fluid nourishes the nearby tissues. If a patient has glaucoma, the fluid does not drain properly. This leads to fluid build-up and the pressure inside the eye rises. This increased pressure may damage the optic disc and result in the loss of vision. There is a small brighter

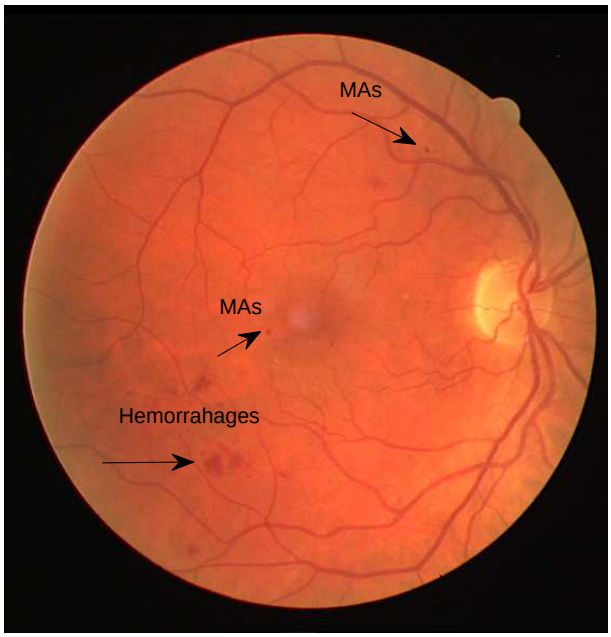

Figure A.1: Retinal image (DRIVE database) with microaneurysms and hemorrhages.

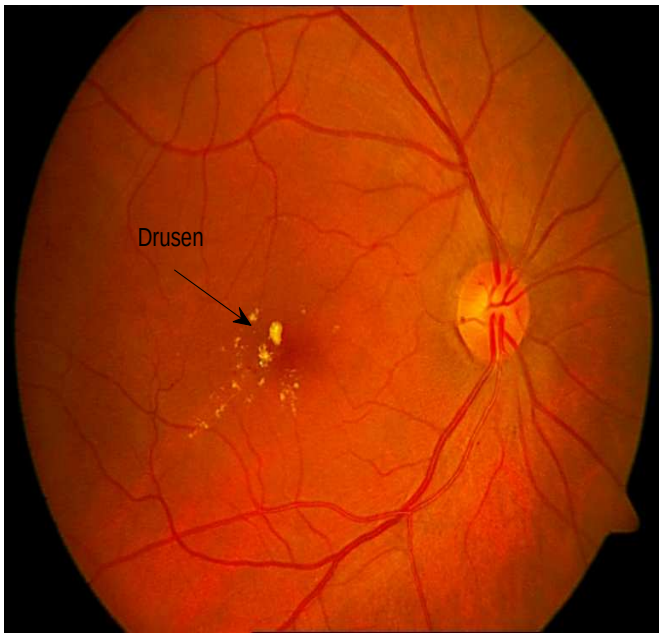

Figure A.2: Retinal image showing drusen. (The image is obtained from a local eye hospital, Sankaradeva Netralaya)

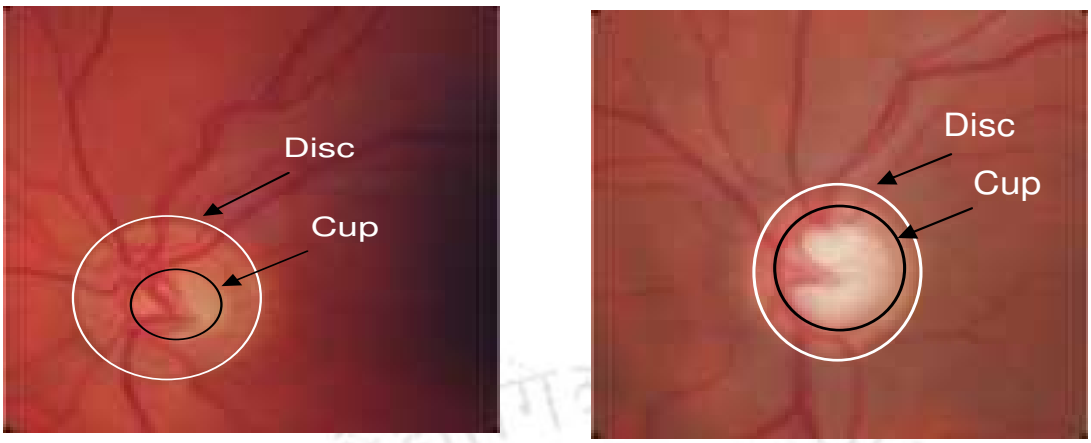

(a) (b)

Figure A.3: (a) Normal OD (b) OD showing increased size of the cup in case of glaucoma (http://optic-disc.org).

region within the OD, known as cup. The disc and cup regions in a normal image is shown in Figure A.3(a). The primary indication of glaucoma is the increased cup size or cupping of the OD. This is a visible manifestation of the optic disc structure as shown in Figure A.3(b). The ratio of the cup and optic disc called cup-to-disc ratio (CDR), is an important structural indicator for assessing the presence and progression of glaucoma.

B

Training and instructions to the subjects

Contents

B.1 Training instructions 161

Before starting the subjective evaluation process, instructions were provided to the subject to explain his/her task. Each subject was individually briefed about the goal of the Experiment. Assessors were carefully introduced to the method of assessment, the types of impairment, the grading scale, the sequence and timing. A training session was conducted showing examples of retinal images of right eye and left eye and their important components. These images are obtained from the different websites and the databases given below

http://www.diabeticeyes.com/

http://www.isi.uu.nl.Research/Databases/DRIVE/

http://www.parl.clemson.edu/stare/

Once the subjects are familiarized with the images, a set of training images were presented to the viewers. These training images are small set of (10) images taken from the set of large number of test images. We selected the training images to span the same range of quality as the test images. This gives the subject an idea of the quality of images they would be viewing in the actual study and to enable suitable use of the quality scale by the subject. We selected the training images to span the same range of quality as the test images. This gives the subject an idea of the quality of images they would be viewing in the actual study and to enable suitable use of the quality scale by the subject. All the training images were shown one by one along with the reference (as a pair). Then the subject is exercised to provide quality scores for the training images to familiarize themselves with the testing procedure. The subjects were asked to consider the quality of each of the clinical components and also the overall image. The format given in the training session for assigning the scores is shown in Table B.1. Training was evaluated by repeating the session sufficient number of times till the subjects are familiarized with the scoring procedure. After training and the subjects said that they are ready for the test, they are instructed to give only one final score as their MOS. Then the test images were shown in a random order to each subject in a separate session.

Table B.1: Format for giving the MOS

Test image	OD	Blood vessels	Macula	Overall MOS
Test image 1				
Test image 2				
Test image 3				
Test image 4				

B.1 Training instructions

The instructions given to the subjects before the subjective test are,

- In this experiment you will see a pair of images on the computer screen in front of you.
- For each of the image pair, you should judge the quality of second image comparing it with the first image.
- Consider the image to be of excellent quality (80-100), if all the clinical features are clearly visible.
- If the thin vessels are blurred but other features are clear, then the image is considered to be in the range of good quality (60-80).
- The test image should be rated as fair (40-60) if thin vessels are not visible and other retinal features look slightly blurred.
- If all the features are heavily blurred and not clearly visible, then it should be in the range of poor (20-40) image quality.
- When the entire image looks blurry and the features are not visible, then the image should be classified as bad quality (0-20) image.

References

[1] J. C. Duncan and N. Ayache, "Medical image analysis: Progress over two decades and the challenges ahead," *IEEE Trans. Pattern Anal. Mach. Intell.*, vol. 22, no. 1, pp. 85–106, 2000.

[2] R. Klein, B. Klein, M. Neider, L. Hubbard, S. Meuer, and B. Brothers, "Diabetic retinopathy as detected using opthalmoscopy, a nonmydriatic camera and a standard fundus camera," *Opthamology*, vol. 92, no. 4, pp. 485–491, 1985.

[3] D. Usher, M. Dumskyj, M. Himaga, T. H. Williamson, S. Nussey, and J. Boyce, "Automated detection of diabetic retinopathy in digital retinal images: a tool for diabetic retinopathy screening," *Diabetic Medicine*, vol. 21, no. 1, pp. 84–90, 2004.

[4] L. Pedersen, M. Grunkin, B. Ersbll, K. Madsen, M. Larsen, N. Christoffersen, and U. Skands, "Quantitative measurement of changes in retinal vessel diameter in ocular fundus images," *Pattern Recognition Letters*, vol. 21, no. 13-14, pp. 1215–1223, 2000.

[5] G. Dougherty, M. J. Johnson, and M. D. Wiers, "Measurement of retinal vascular tortuosity and its application to retinal pathologies," *Med Biol Eng Comput, Springer*, vol. 48, pp. 87–95, 2010.

[6] H. N. Iyer, A. Can, B. Roysam, V. Stewart, H. L. Tanenbaum, A. Majerovics, and H. Singh, "Robust detection and classification of longitudinal changes in color retinal fundus images for monitoring diabetic retinopathy," *IEEE Transactions on Biomedical Engineering*, vol. 53, no. 6, pp. 1084 – 1098, 2006.

[7] E. Grisan, M. Foracchia, and A. Ruggeri, "A novel method for the automatic grading of retinal vessel tortuosity," *IEEE Trans. Med. Imaging*, vol. 27, no. 3, pp. 310–319, 2008.

[8] M. Niemeijer, van Ginneken B, M. J. Cree, A. Mizutani, G. Quellec, C. I. Sanchez, B. Zhang, R. Hornero, M. Lamard, C. Muramatsu, X. Wu, G. Cazuguel, J. .You, A. .Mayo, Q. Li, Y. Hatanaka, B. Cochener, C. Roux, F. Karray, M. Garcia, H. Fujita, and M. D. Abramoff, "Retinopathy online challenge: automatic detection of microaneurysms in digital color fundus photographs," *IEEE Trans Med Imaging*, vol. 29, no. 1, pp. 185–195, 2010.

[9] A. Houben, M. Canoy, H. Paling, P. Derhaag, and P. de Leeuw, "Quantitative analysis of retinal vascular changes in essential and renovascular hypertension," *Journal of Hypertension*, vol. 13, p. 17291733, 1995.

[10] T. Chanwimaluang, Guoliang Fan, and S. R. Fransen, "Hybrid retinal image registration," *IEEE Trans. Inform. Tech. Biomed.*, vol. 10, no. 1, pp. 129–142, 2006.

[11] J. Xu, O. Chutatape, E. Sung, C. Zheng, and P. C. T. Kuan, "Optic disk feature extraction via modified deformable model technique for glaucoma analysis," *Pattern recognition*, vol. 40, p. 2063 2076, 2007.

[12] S. Sekhar, W. Al-Nuaimy, and A. K. Nandi, "Automated localisation of optic disk and fovea in retinal fundus images," in *16th European Sinal Processing COnference(EUSIPCO 2008)*, Lausanne, Switzerland,, 2008.

[13] K. Rapantzikos, M. Zervakis, and K. Balas, "Detection and segmentation of drusen deposits on human retina: Potential in the diagnosis of age-related macular degeneration," *Med. Image Anal*, vol. 7, p. 95108, 2003.

[14] C. C. Köse, U. U. Şevik, and O. O. Gençalioğlu, "Automatic segmentation of age-related macular degeneration in retinal fundus images," *Computers in Biology and Medicine*, vol. 38, no. 5, pp. 611–619, 2008.

[15] K. W. Tobin, E. Chaum, V. P. Govindasamy, and T. P. Karnowski, "Detection of anatomic structures in human retinal imagery," *IEEE Trans. Med. Imag.*, vol. 26, no. 12, pp. 1729–1739, 2007.

[16] S. Chaudhuri, S. Chatterjee, N. Katz, M. Nelson, and M. Goldbaum, "Detection of blood vessels in retinal images using two-dimensional matched filters," *IEEE Transactions on Medical Imaging*, vol. 8, no. 2, pp. 263–269, 1989.

[17] A. Hoover, V. Kouznetsova, and M. Goldbaum, "Locating blood vessels in retinal images by piecewise threshold probing of a matched filter response," *IEEE Trans. Med. Imag*, vol. 19, no. 3, pp. 203–210, 2000.

[18] Bob Zhang , Lin Zhang, Lei Zhang, Fakhri Karray, "Retinal vessel extraction by matched filter with first-order derivative of gaussian," *Computers in Biology and Medicine*, vol. 40, no. 4, pp. 438–445, 2010.

[19] A. M. Mendonca and A. Campilho, "Segmentation of retinal blood vessels by combining the detection of centerlines and morphological reconstruction," *IEEE Trans Med Imaging*, vol. 25, no. 9, pp. 1200–1213, 2006.

[20] F. Zana and J. C. Klein, "Segmentation of vessel-like patterns using mathematical morphology and curvature evaluation," *IEEE Trans Image Process.*, vol. 10, no. 7, pp. 1010–1019, 2001.

[21] X. Gao, A. Bharath, A. Stanton, A. Hughes, N. Chapman, and S. Thom, "A method of vessel tracking for vessel diameter measurement on retinal images," in *Proc. ICIP'01*, vol. 2, 2001, pp. 881–884.

[22] M. E. Martinez-Perez, A. D. Hughes, A. V. Stanton, S. A. Thom, A. A. Bharath, and K. H. Parka, "Retinal blood vessel segmentation by means of scale-space analysis and region growing," *In Proceedings of the International Conference on Image Processing*, vol. 2, pp. 173–176, 1999.

[23] M. Elena Martinez-Perez and A. D. Hughes and Simon A. Thom and Anil A. Bharath and Kim H. Parker, "Segmentation of blood vessels from red-free and fluorescein retinal images," *Medical Image Analysis*, vol. 11, no. 1, pp. 47–61, 2007.

[24] M. Niemeijer, J. J. Staal, B. van Ginneken, M. Loog, and M. Abramoff, "Comparative study of retinal vessel segmentation methods on a new publicly available database," in *PRoc. SPIE Medical Imaging,*, vol. 5370, 2004, pp. 648–656.

[25] J. J. Staal, M. D. Abrmoff, M. Niemeijer, M. A. Viergever, and B. van Ginneken, "Ridge based vessel segmentation in color images of the retina," *IEEE Trans. Med. Imag.*, vol. 23, no. 4, pp. 501–509, 2004.

[26] J. V. B. Soares, J. J. G. Leandro, R. M. Cesar-Jr., H. F. Jelinek, and M. J. Cree, "Retinal Vessel segmentation using the 2-D gabor wavelet and supervised classification," *IEEE Trans. on Medical Imaging*, vol. 25, no. 9, pp. 1214–1222, 2006.

[27] D. Marin, A. Aquino, M. E. Gegndez-Arias, and J. M. Bravo, "A new supervised method for blood vessel segmentation in retinal images by using gray-level and moment invariants-based features," *IEEE Trans. Medi. Imag.*, vol. 30, no. 1, pp. 146–158, 2011.

[28] M. Niemeijer, B. V. Ginneken, and M. D. Abràmoff, "Automatic determination of the artery vein ratio in retinal images," in *in Medical Imaging: Image Analysis. Proc. SPIE Medical Imaging*, vol. 5376, Bellingham, WA, 2010.

[29] C. Sinthanayothin, J. F. Boyce, H. L. Cook, and T. H. Williamson, "Automated localisation of the optic disk, fovea, and retinal blood vessels from digital colour fundus images," *Br. J. Ophthalmol.*, vol. 83, no. 8, pp. 902–910, 1999.

[30] T. Walter and J. C. Klein, "Segmentation of color fundus images of the human retina: Detection of the optic disc and the vascular tree using morphological techniques," in *Proc. 2nd Int. Symp. Med. Data Anal.*, 2001, pp. 282–287.

[31] H. Li and O. Chutatape, "Automated feature extraction in color retinal images by a model based approach," *IEEE Trans. Biomed. Eng.*, vol. 51, no. 2, pp. 246–254, 2004.

[32] A. Mahfouz and A. Fahmy, "Fast Localization of the Optic Disc Using Projection of Image Features," *IEEE Trans. Img. Proc.*, vol. 19, no. 12, pp. 3285–3289, 2010.

[33] M. Niemeijer, M. D. Abrmoff, and B. van Ginneken, "Segmentation of the optic disc, macula and vascular arch in fundus photographs," *IEEE Trans. Med. Imag.*, vol. 26, no. 1, pp. 116–127, 2007.

[34] A. D. Fleming, K. A. Goatman, S. Philip, J. A. Olshen, and P. F. Sharp, "Automatic detection of retinal anatomy to assist diabetic retinopathy screening," *Phys. Med Biol.*, vol. 52, no. 2, pp. 331–345, 2007.

[35] M. Niemeijer, M. D. Abrmoff, and B. van Ginneken, "Fast detection of the optic disc and fovea in color fundus photographs," *Medical Image Analysis*, vol. 13, pp. 859–870, 2009.

[36] J. H. Hipwell, F. Strachan, J. A. Olson, K. C. McHardy, P. F. Sharp, and J. V. Forrester, "Automated detection of microaneurysms in digital red-free photographs: A diabetic retinopathy screening tool," *Diabet. Med.*, vol. 17, no. 8, pp. 588–594, 2000.

[37] S. Lee, E. Lee, R. Kingsley, Y. Wang, D. Russell, R. Klein, and A. Warn, "Comparison of diagnosis of early retinal lesions of diabetic retinopathy between a computer and human experts," *Arch. Ophthalmol.*, vol. 119, pp. 509–515, 2001.

[38] C. Sinthanayothin, J. Boyce, T. Williamson, H. Cook, E. Mensah, S. Lal, and D. Usher, "Automated detection of diabetic retinopathy on digital fundus images," *Diabet. Med.*, vol. 19, pp. 105–112, 2002.

[39] M. Niemeijer, B. van Ginneken, J. Staal, M. S. A. Suttorp-Schulten, and M. D. Abramoff, "Automatic detection of red lesions in digital color fundus photographs," *IEEE Trans. Med. Imaging*, vol. 24, no. 4, pp. 584–592, 2005.

[40] H. F. Jelinek, M. J. Cree, D. Worsley, A. Luckie, and P. Nixon, "An automated microaneurysm detector as a tool for identification of diabetic retinopathy in rural optometric practice," *Clin. Exp. Optom.*, vol. 89, no. 5, pp. 299–305, 2006.

[41] G. Quellec, M. Lamard, P. M. Josselin, G. Cazuguel, B. Cochener, and C. Roux, "Optimal wavelet transform for the detection of microaneurysms in retina photographs," *IEEE Trans. Med. Imaging*, vol. 27, no. 9, pp. 1230–1241, 2008.

[42] K. Ram, G. D. Joshi, , and J. Sivaswamy, "A successive clutter-rejection-based approach for early detection of diabetic retinopathy," *IEEE Trans. Biomed. Eng.*, vol. 58, no. 3, pp. 664–674, 2011.

[43] A. M. Eskicioglu and P. S. . Fisher, "Image quality measures and their performance," *IEEE Trans. on communications*, vol. 43, no. 12, pp. 2959–2965, 1995.

[44] S. Wong, L. Zaremba, D. Gooden, and H. K. Huang, "Radiological image compression: A review," *Proc. IEEE*, vol. 83, no. 2, pp. 194–219, 1995.

[45] Z. Wang, A. C. Bovik, H. Sheikh, and E. P. Simoncelli, "Image quality assessment: From error visibility to structural similarity," *IEEE Trans. Image Process.*, vol. 13, no. 4, pp. 600–612, 2004.

[46] H. R. Sheikh and A. C. Bovik, "Image information and visual quality," *IEEE Trans. Image Process*, vol. 15, no. 2, pp. 430–444, 2006.

[47] H. R. Sheikh, A. C. Bovik, and G. de Veciana, "An information fidelity criterion for image quality assessment using natural scene statistics," *IEEE Trans. Image Process*, vol. 14, no. 12, pp. 2117–2128, 2005.

[48] S. Mallat, "A theory for multiresolution signal decomposition : the wavelet representation," *EEE Trans. Pattern Analysis and Machine Intelligence*, vol. 11, no. 7, pp. 674–693, July 1989.

[49] S. Mallat and W. L. Hwang, "Singularity detection and processing with wavelets," *IEEE Transactions on Information Theory*, vol. 38, no. 2, pp. 617–643, Mar 1992 Volume: 38 Issue:2 On page(s): 617 - 643.

[50] J. B. Weaver, X. Yansun, D. M. Healy, and L. D. Cromwell, "Filtering noise from images with wavelet transforms," *Magnetic Resonance in Medicine*, vol. 21, no. 2, pp. 288–295, 1991.

[51] A. Thakur and R. S. Anand, "Image quality based comparative evaluation of wavelet filters in ultrasound speckle reduction," *Digital Signal Processing*, vol. 15, pp. 455–465, 2005.

[52] A. Munteanu, J. Cornelis, G. V. der Auwera, and P. Cristea, "Wavelet image compression-the quadtree coding approach," *IEEE Trans. on Information Technology in Biomedicine*, vol. 3, no. 3, pp. 176–185, 1999.

[53] M. Antonini, M. Barlaud, P. Mathieu, and I. Daubechies, "Image coding using wavelet transform," *IEEE Transactions on Image Processing*, vol. 1, pp. 205–220, 1992.

[54] M. Unser and A. Aldroubi, "A review of wavelets in biomedical applications," *Proc. IEEE*, vol. 84, pp. 626–638, 1996.

[55] A. F. Laine, "Wavelets in temporal and spatial processing of biomedical images,," *Annual Review of Biomedical Engineering*, vol. 2, pp. 511–550, 2000.

[56] M. Unser, A. Aldroubi, and A. Laine, "Guest editorial: Wavelets in medical imaging," *IEEE Transactions on Medical Imaging*, vol. 22, no. 3, pp. 285–288, 2003.

[57] S. Lee and Y. Wang, "Automatic retinal image quality assessment and enhancement," in *Proc. of SPIE Image Processing,*, S. C. on Image Processing, Ed., 1999, pp. 1581–1590.

[58] M. Lalonde, L. Gagnon, and M. C. Boucher, "Automatic visual quality assessment in optical fundus images," in *Proc. of Vision Interface*, Ottava, June 2001, pp. 259–264.

[59] D. B. Usher, M. Himaga, and M. J. Dumskyj, "Automated assessment of digital fundus image quality using detected vessel area," *Proceedings of Medical Image Understanding and Analysis*, pp. 81–84, 2003.

[60] A. D. Fleming, S. Philip, K. A. Goatman, J. A. Olson, and P. F. Sharp, "Automated assessment of diabetic retinal image quality based on clarity and field definition," *Invest Ophthalmol Vis Sci.*, vol. 47, no. 3, pp. 1120–1125, 2006.

[61] M. Niemeijer, M. D. Abramoff, and . Bram van Ginneken 10(6), pp. 888898, "Image structure clustering for image quality verification of color retina images in diabetic retinopathy screening," *Med Image Anal*, vol. 10, no. 6, pp. 888–898, 2006.

[62] L. Giancardo, M. D. Abràmoff, E. Chaum, T. P. Karnowski, F. Meriaudeau, and T. K. Jr, "Elliptical local vessel density: a fast and robust quality metric for retinal images," in *30th annual international conference of the IEEE*, Engineering in Medicine and Biology Society (EMBS), 2008, pp. 3534–3537.

[63] J. Paulus, J. Meier, R. Bock, J. Hornegger, and G. Michelson, "Automated quality assessment of retinal fundus photos," *International journal of computer assisted radiology and surgery*, 2010.

[64] P. Hänsgen, P. E. Undrill, and M. J. Cree, "The application of wavelets to retinal image compression and its effect on automatic microaneurysm analysis," *Computer Methods and Programs in Biomedicine*, vol. 56, no. 1, pp. 1–10, 1998.

[65] R. H. Eikelboom, K. Yogesan, C. J. Barry, I. J. Constable, M. T. Kearney, L. Jitskaia, and P. H. House, "Methods and limits of digital image compression of retinal images for telemedicine," *Investigative Ophthalmology and Visual Science*, vol. 41, no. 7, pp. 1916–1924, 2000.

[66] D. Beauregard, J. Lewis, M. Piccolo, and H. Bedell, "Diagnosis of glaucoma using telemedicine - the effect of compression on the evaluation of optic nerve head cup-disc ratio," *Journal of Telemedicine and Telecare*, vol. 6, pp. 123–125, 2000.

[67] J. Conrath, A. Erginay, R. Giorgi, A. Lecleire-Collet, E. Vicaut, J.-C. Klein, A. Gaudric, and P. Massin, "Evaluation of the effect of jpeg and jpeg2000 image compression on the detection of diabetic retinopathy," *Eye, Official journal of The Royal College of Ophthalmologists*, vol. 21, p. 487493, 2006.

[68] A. Basu, A. D. Kamal, W. Illahi, M. Khan, P. Stavrou, and R. E. J. Ryder, "Is digital image compression acceptable within diabetic retinopathy screening?" *Diabetic Medicine*, vol. 20, no. 9, pp. 766 – 771, 2003.

[69] M. J. Cree and H. F. Jelinek, "The effect of jpeg compression on automated detection of microaneurysms in retinal images," *Proc. of SPIE-IS&T Electronic Imaging*, vol. 6813, pp. 68 130M–68 130M 10, 2008.

[70] S. Mallat and S. Zhong, "characterization of signals from multi-scale edges," *IEEE Trans. Pattern Analysis and machine Intelligence*, vol. 14, no. 7, pp. 710–732, 1992.

[71] B. Erickson, A. Manduca, P. Palisson, K. Persons, V. S. F. Earnest, IV and, and N.Hangiandreou, "Wavelet compression of medical images," *Radiology*, vol. 206, pp. 599–607, 1998.

[72] H. Ringl, R. E. Schernthaner, A. A. Bankier, M. Weber, M. Prokop, C. J. Herold, and C. S. Prokop, "Jpeg2000 compression of thin-section ct images of the lung: Effect of compression ratio on image quality," *Radiology*, vol. 240, pp. 869–877, 2006.

[73] N. Patton, T. M. Aslam, T. MacGillivray, I. J. Deary, B. Dhillon, R. H. Eikelboom, K. Yogesan, and I. J. C. 25(1), "Retinal image analysis: Concepts, applications and potential," *Progress in retinal and eye research*, vol. 25, no. 1, pp. 99–127, 2006.

[74] *ITU - R Recommendation B T 500 - 11, Methodology for the subjective assessment of the quality of the television pictures, International Telecommunication Union, Geneva, Switzerland, Tech. Rep. 2002.*

[75] Z. Wang and A. C. Bovik, "Mean squared error: Love it or leave it? a new look at signal fidelity measures," *IEEE Signal Processing Magazine*, vol. 26(1), no. 1, pp. 98–117, 2009.

[76] A. P. Bradley, "A wavelet visible difference predictor," *IEEE Trans. Image process.*, vol. 8, no. 5, pp. 717–730, 1999.

[77] Z. Wang and A. C. Bovik, "A universal image quality index," *IEEE Signal Processing Letters*, vol. 9, pp. 81–84, 2002.

[78] P. Cosman, R. M. Gray, and R. A. Olshen, "Evaluating the quality of compressed medical images: Snr, subjective rating and diagnostic accuracy," *Proc. IEEE*, vol. 82, no. 6, pp. 919–932, 1994.

[79] R. H. Eikelboom, K. Yogesan, I. J. Constable, and C. J. Barry, "Jpeg and wavelet compression of ophthalmic images," *Proceedings of SPIE, Medical Imaging 1999: Image processing*, vol. 3658, pp. 448–455, 1999.

[80] I. Daubechies, *Ten Lectures on Wavelets.* Philadelphia: SIAM, 1992.

[81] S. Mallat, *A Wavelet Tour of Signal Processing 1999.*, second ed. ed. San Diego: Academic Press, 1999.

[82] R. C. Gonzalez and R. E. Woods, *Digital Image Processing*, 3rd ed. Upper Saddle River, NJ: Pearson Prentice Hall, 2008, vol. Chap. 7.

[83] A. Jain, *Fundamentals of Digital Image Processing.* Englewood Cliffs, NJ: Prentice-Hall, 1989.

[84] Z. Wang, E. P. Simoncelli, and A. C. Bovik, "Multi-scale structural similarity for image quality assessment," in *IEEE Asilomar Conf. Signals, Systems, and Computers,*, Nov 2003.

[85] D. M. Chandler and S. S. Hemami, "Vsnr: a wavelet-based visual signal-to-noise ratio for natural images," *IEEE Trans. Image Process.*, vol. 16, no. 9, p. 22842298, 2007.

[86] E. Dumic, S. Grgic, and M. Grgic, "New image-quality measure based on wavelets," *J. of Electronic Imaging*, vol. 19(1), no. 1, pp. 011–018, 2010.

[87] Z. Gao and Y. F. Zheng, "Quality constrained compression using dwt-based image quality metric," *IEEE Trans. Circuits and Systems for video technology*, vol. 18, no. 7, pp. 910–922, 2008.

[88] Y. Zigel, A. Cohen, and A. Katz, "The weighted diagnostic distortion (WDD) measure for ECG signal compression," *IEEE Trans. Biomed. Eng.*, vol. 47, no. 11, pp. 1422–1430, 2000.

[89] S. Amjed and Al-Fahoum, "Quality assessment of ECG compression techniques using a wavelet-based diagnostic measure," *IEEE Transactions on Information Technology in Biomedicine*, vol. 10, no. 1, pp. 182–191, 2006.

[90] A. D. Fleming, S. Philip, K. A. Goatman, P. Sharp, and J. A. Olson, "Automated clarity assessment of retinal images using regionally based structural and statistical measures," *Med Eng and Physics*, vol. doi:10.1016/j.medengphy.2011.09.027, 2011.

[91] R. H. Eikelboom, K. Yogesan, I. J. Constable, I. L. McAllister, M. L. Tay-Kearney, and C. J. Barry, "Digital image compression of retinal images for telemedicine applications," *Ophthalmic Research*, vol. 30, p. 122, 1998.

[92] W. Hwang, C. Chine, and K. Li, "Scalable medical data compression and transmission using wavelet transform for telemedicine applications," *IEEE Transactions on Information Technology in Biomedicine*, vol. 7, no. 1, pp. 54–63, 2003.

[93] A. Pizurica and W. Philips, "A versatile wavelet domain noise filtration technique for medical imaging," *IEEE Trans. Med. Imag.*, vol. 22, no. 3, pp. 323–331, 2003.

[94] A. Przelaskowski and A. Kukula, "Estimation of diagnostic ability by diagnostic features assessment tests," *Proc. XVII IMEKO World Congress, Croatia*, pp. 1447–1451, 2003.

[95] A. Przelaskowski, "Vector quality measure of lossy compressed medical images," *Computers in Biology and Medicine*, vol. 34(3), pp. 193–207, 2004.

[96] ——, "Compression of mammograms for medical practice," in *ACM Symposium on Applied Computing*, 2004, pp. 249–253.

[97] C. Doukas and I. Maglogiannis, "Region of interest coding techniques for medical image compression," *IEEE Engg. Medicine and Biology Magazine*, vol. 26, no. 5, pp. 29–35, 2007.

[98] http://www.isi.uu.nl/Research/Databases/DRIVE.

[99] T. Walter, P. Massin, A. Erginay, R. Ordonez, C. Jeulin, and J. C. Klein, "Automatic detection of microaneurysms in color fundus images," *Med. Image Analysis*, vol. 11, no. 6, pp. 555–556, 2007.

[100] M. Penedo, W. A. Pearlman, P. G. Tahoces, M. Souto, and J. J. Vidal, "Region based wavelet coding methods for digital mammography," *IEEE Trans. on Medical Imaging*, vol. 22, no. 10, pp. 1288–1296, 2003.

[101] S. Grgic, M. Grgic, and B. Zovko-Cihlar, "Performance analysis of image compression using wavelets," *IEEE Transaction on Industrial Electronics*, vol. 48, no. 3, pp. 682–695, 2001.

[102] A. Said and W. A. Pearlman, "A new fast and efficient image codec based on set partitioning in hierarchical trees," *IEEE Trans. Circuits Syst. Video Technol*, vol. 6, no. 3, pp. 243–250, 1996.

[103] M. Beladgham, A. Bessaid, and A. Taleb-Ahmed, "Improving quality of medical image compression using biorthogonal CDF wavelet based on lifting scheme and spiht coding," *Serbian Journal of Electrical Engineering*, vol. 8, no. 2, pp. 163–179, 2011.

[104] B. E. Usevitch, "A Tutorial on Modern Lossy Wavelet Image Compression: Foundations of JPEG 2000," *IEEE Sig. Proc. Mag.*, vol. 18, no. 5, pp. 22–35, 2001.

[105] R. S. Khandpur, *Handbook of biomedical instrumentation*, 2nd ed. Tata Mcgraw Hill Education Pvt Ltd, 2003.

[106] A. F. Laine and S. Song, "Multiscale wavelet representations for mammographic feature analysis," in *Mathemetical Methods in Medical Imaging, Proceedings of SPIE*, vol. 1768, San Diego, CA, 1992, pp. 306–316.

[107] P. Feng, Y. Pan, B. Wei, and D. Mi, "Enhancing retinal image by the Contourlet transform," *Pattern Recognition Letters*, vol. 28, pp. 516–522, 2007.

[108] M. J. Cree, J. . A. Olson, K. C. McHardy, P. Sharp, and J. V. Forrester, "The preprocessing of retinal images for the detection of fluorescein leakage," *Physics in Medicine and Biology*, vol. 44, pp. 293–308, 1999.

[109] C. W. Chen, Y. Q. Zhang, and K. J. Parker, "Subband analysis and synthesis of volumetric medical images using wavelet," in *Visual Communications and Image processing*, vol. 2308, no. 3. Chicago, IL, USA: SPIE, Bellingham, WA, 1994, pp. 1544–1555.

[110] X. Jiang and D. Mojon, "Adaptive local thresholding by verificationbased multithreshold probing with application to vessel detection in retinal images," *IEEE Trans. Pattern Anal. Mach. Intell.*, vol. 25, no. 1, pp. 131–137, 2003.

[111] T. Chanwimaluang and G. Fan, "An efficient blood vessel detection algorithm for retinal images using local entropy thresholding," in *Proc. of the 2003 IEEE International Symposium on Circuits and Systems*, vol. 5, 2003, pp. V–21–V–24.

[112] Y. K. Lai and C. C. J. Kuo, "A harr wavelet approach to compressed image quality measurements," *J. of Visual Commun. and Image Representation*, vol. 11, pp. 17–40, 2000.

[113] O. Rosso, S. Blanco, J. Yordanova, V. Kolev, A. Figliola, M. Sahurmann, and E. Basar, "Wavelet entropy: A new tool for analysis of short brain electrical signal," *Neuroscience Methods*, vol. 105, pp. 65–75, 2001.

[114] D. Bandah, T.Swissa, G. B. Shlomo, E. Banin, R. Ofri, and D. Sharon, "A Complex Expression Pattern of Pax6 in the pigeon retina," *Invest Ophthalmol Vis Sci.*, vol. 48, no. 6, pp. 2503–2509, 2007.

[115] T. J. Chen, K. S. Chuang, J. Wu, S. C. Chen, I. M. Hwang, and M. L. Jan, "Quality degradation in lossy wavelet image compression," *J. Digit Imaging*, vol. 16, no. 2, pp. 210–215, 2003.

[116] H. F. Jelinek and M. J. Cree, Eds., *Automated Image Detection of Retinal Pathology.* CRC Press, Taylor & Francis Group, 2010.

[117] A. Manduca and A. Said, "Wavelet compression of medical images with set partitioning hierarchical trees," in *in Proc. Int. Conf. IEEE Engineering in Medicine and Biology Soc. (EMBS)*, vol. 3, 1997, pp. 1224–1225.

[118] R. C. Gonzalez, R. E. Woods, and S. L. Eddins, *Digital Image Processing using MATLAB*. Pearson Education, 2004.

[119] VQEG, "Final report from the video quality experts group on the validation of objective models of video quality assessment, phase II 2003 vqeg, [online]. available: http://www.vqeg.org," 2003.

[120] H. R. Sheikh, M. F. Sabir, and A. C. Bovik, "A statistical evaluation of recent full reference image quality assessment algorithms," *IEEE Tans. Image Process.*, vol. 15, no. 11, pp. 3441–3452, 2006.

[121] A. K. Moorthy, K. Seshadrinathan, R. Soundararajan, and A. C. Bovik, "Wireless video quality assessment: A study of subjective scores and objective algorithms," *IEEETrans. Circuits and Systems for Video Technology*, vol. 20, no. 4, pp. 587–599, 2010.

[122] P. Nguyen, M. Luong, and A. Baghdadi, *Statistical Analysis of Image Quality Metrics for Watermark Transparency Assessment*, ser. LNCS. Springer Berlin Heidelberg, 2010, vol. 6297, pp. 685–696.

[123] I. Avcibas, B. Sankur, and K. Sayood, "Statistical evalaution of image quality measures," *Journal of Electronic Imaging*, vol. 11, no. 2, pp. 206–223, 2002.

[124] G. K. Wallace, "The jpeg still picture compression standard," *IEEE Trans. Consum. Electron*, vol. 38, no. 1, pp. 18–34, 1992.

[125] A. M. Eskicioglu, "Quality measurement for monochrome compressed images in the past 25 years," in *Proc. IEEE Int. Conf. Acoustics,Speech,Signal Processing*, no. 4. Istanbul, Turkey, June 2000, pp. 1907–1910.

[126] B. Girod, *Whats wrong with mean-squared error*, E. A. B. Watson, Ed. Cambridge, MA: MIT Press, 1993.

[127] *Structural Similarity Index (SSIM) and Multi-Scale SSIM (MS-SSIM), Available: http://live.ece.utexas.edu/research/Quality/.*

[128] *Inforamtion Fidelity Criterion and Visual Information Fidelity, Available: http://live.ece.utexas.edu/research/quality/.*

[129] *Visual Signal to Noise Ratio [Online]. Available: http://foulard. ece.cornell.edu/dmc27/vsnr/vsnr matlab source.zip.*

[130] A. C. Rencher, *Methods of Multivariate Analysis*. New York: John Wiley, 1995.

[131] T. D. Dixon, E. F. Canga, S. G. Nikolov, T. Troscianko, J. M. Noyes, C. N. Canagarajah, and D. R. Bull, "Selection of image fusion quality measures: objective, subjective and metric assessment," *J. Opt. Soc. Am. A*, vol. 24, no. 12, pp. B125–B135, 2007.

LIST OF PUBLICATIONS

Refereed Journals:

(1) S. R. Nirmala, S. Dandapat and P. K. Bora, "Image Quality Measures: A Review from Diagnostic Perspective of Medical Images," *Computer Society of India, Kolkata Chapter (CSIKC)* Sept 2006.

(2) S. R. Nirmala, S. Dandapat and P. K. Bora, "Wavelet weighted blood vessel distortion measure for retinal images," *Biomed. Signal Process. Control, Elsevier,* vol. 5, no. 4, pp. 282-291, 2010.

(3) S. R. Nirmala, S. Dandapat and P. K. Bora, "Performance Evaluation of Distortion Measures for Retinal Images," *International Journal of Computer Applications, Foundation of Computer Science, USA,* vol. 17, no.6, pp. 17-23, March 2011.

(4) S. R. Nirmala, S. Dandapat and P. K. Bora, "Phase congruency-based Measure for Quality assessment of the Compressed Retinal images," *International Journal of Imaging and Robotics (IJIR), CESER publications,*, vol. 6, no. A11, pp. 20-31, Autumn 2011.

(5) S. R. Nirmala, S. Dandapat, P. K. Bora , "DTCWT based blood vessel extraction in retinal image analysis", *International journal of Biomedical Engineering and Consumer Health Informatics(IJBECHI), Serials publications,*, vol. 3, no. 1, pp. 1-5, 2011.

(6) S.R. Nirmala, Malaya Kumar Nath, Samarendra Dandapat, "Retinal Image Analysis: A Review", *International journal of Computer and Communication Technology (IJCCT), Interscience Open Access Journals,*, vol. 2, no. 6, pp. 11-14, 2011.

(7) S. R. Nirmala, S. Dandapat and P. K. Bora, "Wavelet weighted distortion measure for retinal images," *Signal, image and video processing, Springer*, 2012.
(Accepted for publication, DOI:10.1007/s11760-012-0290-8)

Article in Book:

(1) S. R. Nirmala, S. Dandapat and P. K. Bora, "Discrete Wavelet Transform (DWT) based blood vessel segmentation in automatic analysis of retinal images", *Biomedical Engineering*, Narosa Publishing House Pvt. Ltd., Delhi, India, pp. 202-209, 2011.

Refereed Conferences:

(1) S. R. Nirmala, S. Dandapat and P. K. Bora, "Image Quality Assessment in Retinal Image Compression systems," *in Proc. IET-UK Int. Conf. Information and Communication Technology in Electrical Sciences (ICTES 2007)*, Chennai, India, Dec. 2007.

(2) S. R. Nirmala, S. Dandapat and P. K. Bora, "Vessel Segmentation by Template Matching in Retinal Blood Vessel Structure Analysis," *in Proc. IEEE India Annual Conference (INDICON)*, Bangalore, India, Sept. 2007.

(3) L. N. Sarma, S. R. Nirmala, M. S. Manikandan and S. Dandapat, "Compression of multi-lead ECG signals and retinal images using 2-D wavelet transform and SPIHT coding scheme for mobile telemedicine", *in Proc. workshop on Image and Signal Processing (WISP 2007)*, pp. 18-27, Dec. 2007.

(4) S. R. Nirmala, S. Dandapat and P. K. Bora, "Performance Evaluation of Wavelet Filters for Compression of Retinal Images," *in Proc. National conference on communication (NCC)*, IIT Guwahati, India, Jan. 2009.

(5) S. R. Nirmala, S. Dandapat and P. K. Bora, "Wavelet weighted diagnostic distortion measure for the Optic disc," *in Proc. 8th international conference on signal processing and communications (SPCOM)*, IISc Bangalore, India, July 2010.

(6) S. R. Nirmala, S. Dandapat and P. K. Bora, "Discrete Wavelet Transform (DWT) based blood vessel segmentation in automatic analysis of retinal images", *in Proc. International Conference on Biomedical Engineering (ICBME 2011),* Manipal Institute of Technology, Manipal, India, Dec 2011.